

A Frequency Domain Approach to Synchronization of Filterbank Multicarrier Systems in Practice

Von der Fakultät für Elektrotechnik und Informatik
der Gottfried Wilhelm Leibniz Universität Hannover
zur Erlangung des akademischen Grades
Doktor-Ingenieur (Dr.-Ing.) genehmigte

Dissertation

von

Dipl.-Ing. Christoph Oliver Thein

geboren am 4. Mai 1984
in Georgsmarienhütte

2015

1. Referent : Prof. Jürgen Peissig
2. Referent : Prof. Didier le Ruyet (CNAM, Paris)
Tag der Promotion : 30. Januar 2015

ABSTRACT

The need for ubiquitous connectivity and the expectation of ever increasing mobile data traffic drive the research in the field of wireless communications. To satisfy these demands, the fifth generation of cellular networks needs to operate in fragmented spectrum and has to offer an increased spectral efficiency compared to previous generations. In this context, the filterbank multicarrier approach is considered as an enabling technology for efficient fragmented spectrum access due to its flexible system structure. Furthermore, the well-contained subband filtering in frequency domain enables flexible resource allocation and configuration for different types of services which improve co-existence and spectrum utilization. It paves the way for more flexible system designs in shared spectrum scenarios, which poses a challenge on common synchronization schemes that fail when a significant amount of interfering signal power is present in the transmission band.

This thesis discusses a new approach to synchronization in which the processing for synchronization is shifted from time to frequency domain to facilitate flexible resource allocation. The challenges of this approach are presented and a preamble design is developed that enables frequency domain processing with a minimum amount of resources needed. Based on this design a frame detection scheme is analyzed and the lower bounds on the estimation accuracy of the symbol timing and carrier frequency offsets are derived analytically. The lower bounds reveal that frequency domain estimators can in theory achieve the same performance as the time domain approaches. However, the offset-induced mismatch between the synthesis and analysis filterbank degrades the estimation in case of large offsets. For the estimation of the symbol timing offset the optimal as well as practical estimators are derived and analyzed by simulations in addition to the discussion of the frequency offset and channel estimation. It follows from the results that the performance of the frequency domain approach strongly depends on the frequency offset. Hence, two synchronization concepts are proposed and their bit error rate performance is analyzed. It follows that the performance loss due to the error floor of the carrier frequency offset estimation can be counteracted by a compensation stage. While the time and frequency domain approach can deliver the same performance, the analysis of their complexity reveals that the frequency domain approach is more complex in contiguous spectrum scenarios

due to the demodulation process involved. However, this work shows that the overall complexity of synchronization is reduced by the frequency domain approach if it is deployed in shared spectrum scenarios due to the simple separation of subbands in the frequency domain. The developed frequency domain approach is finally tested in a measurement campaign where its performance is verified based on the frame error rate. Even though the analysis of the frame loss rate of the frequency domain method shows a small performance floor due to the block-wise processing, this floor can be removed by a small modification which achieves the same performance as that of time domain solutions.

In conclusion, the outcome of this thesis shows that the frequency domain synchronization approach outperforms alternative time domain schemes in shared spectrum scenarios. Even though the time domain solution offers the same performance at lower computational costs in exclusive spectrum access, the frequency domain processing outperforms time domain schemes in terms of computational costs in shared spectrum access transmission while the same synchronization performance is maintained. Additionally, the frequency domain approach provides a flexibility for resource allocation in fragmented spectrum and multi-user scenarios that cannot be reached by time domain solutions. Hence, by reducing the complexity of synchronization of multiple users, increasing the flexibility of resource allocation, and improving coexistence between different services, the proposed frequency domain synchronization approach provides a further step towards efficient system designs for the next generation of cellular networks.

Keywords: Frequency Domain Synchronization, Filterbank Multicarrier, Shared Spectrum Usage.

ZUSAMMENFASSUNG

Eine Herausforderung für die Mobilfunknetze der Zukunft ist es, sowohl die Kommunikation einer immer größeren Anzahl an Teilnehmern zu bewältigen, als auch die Steigerung des mobilen Datenaufkommens jedes Einzelnen zu bedienen. Um beiden Anforderungen gerecht zu werden, sollte der Mobilfunk der fünften Generation eine höhere spektrale Effizienz, aber auch einen flexibleren Umgang mit der Ressource Bandbreite im Vergleich zu den vorherigen Generationen ermöglichen. In diesem Spannungsfeld bieten filterbankbasierte Mehrträgerverfahren die erforderlichen Eigenschaften zur Umsetzung adaptiver Funkssysteme in fragmentierten Spektren. Sie erlauben ein spektral effizientes Design und den Einsatz von frequenzlokalisierten Subkanalfiltern. Im Gegensatz zu heutigen Mobilfunktechnologien, die einen exklusiven Zugriff auf einen zusammenhängenden Frequenzbereich voraussetzen, stellt der Einsatz von frequenzadaptiven Funksystemen die Tauglichkeit von gängigen Synchronisationsalgorithmen in Frage. Die Realisierung solcher Funkssysteme erfordert neue Ansätze für eine effizientere und robustere Synchronisierung.

Die vorliegende Arbeit beschäftigt sich dabei mit dem Ansatz der Frequenzbereichssynchronisation, wobei dessen Schwierigkeiten und Herausforderungen diskutiert werden. Darauf aufbauend wird eine geeignete Präambelstruktur mit minimalem Ressourcenbedarf entwickelt. Des Weiteren werden sowohl Algorithmen zur Rahmendetektion als auch die unteren theoretischen Grenzen der Schätzgenauigkeit für Zeit- und Frequenzversätze hergeleitet. Dabei zeigt sich, dass die Parameterschätzung im Frequenzbereich keinen Nachteil hinsichtlich der analytisch bestimmbaren Genauigkeit gegenüber vergleichbaren Ansätzen im Zeitbereich bietet. Bedingt durch Zeit- und Frequenzversätze des empfangenen Signals ergeben sich jedoch in der Praxis Beeinträchtigungen, die das Ergebnis der Frequenzschätzung vor allem für große Versätze verschlechtert. Neben der Bewertung von Frequenzversatz- und Kanalkoeffizientenschätzern werden zur Bestimmung des Symbolzeitversatzes in dieser Arbeit sowohl der optimale als auch praktisch realisierbare Schätzer für den Zeitversatz hergeleitet. Aus den gewonnenen Ergebnissen ergibt sich, dass die Frequenzbereichssynchronisation deutlich von dem tatsächlichen Frequenzversatz abhängt. Darauf aufbauend werden zwei Synchronisationskonzepte vorgestellt und anhand der Bitfehlerwahrscheinlichkeit auf Systemebene be-

wertet. Dabei zeigt sich, dass die Abhängigkeit der Schätzungen von dem Frequenzversatz durch eine Kompensationsstufe reduziert werden muss, um eine unbeeinträchtigte Systemleistung zu erzielen. Ein Vergleich der Komplexität der Zeitbereichssynchronisation mit dem Frequenzbereichsansatz verdeutlicht, dass der Zeitbereichsansatz die effizienteste Möglichkeit zur Synchronisation in exklusiv vergebenen Spektrum bietet. Der Frequenzbereichsansatz ermöglicht jedoch bei gleicher Leistung die Reduktion der Komplexität in Szenarien mit fragmentierten Spektrumsbelegungen. Zur Verifikation der entwickelten Frequenzbereichssynchronisation wird diese in einem Messaufbau unter praktischen Bedingungen getestet. Die Messergebnisse zeigen, dass die Resultate für die Systemleistung aus den Simulationen auch in der Praxis bestätigt werden können. Die Rahmenverlustrate, die in der Messung erzielt wurde, befindet sich jedoch oberhalb der Nullmarke und verdeutlicht so den Nachteil des mit der Blockverarbeitung verbundenen Frequenzbereichsansatzes. Um diesem Nachteil entgegen zu wirken, werden Lösungsansätze vorgestellt, mit denen eine verlustfreie Übertragung bei gleichzeitig mäßig steigender Komplexität ermöglicht werden.

Diese Arbeit kommt zusammenfassend zu dem Ergebnis, dass bei exklusivem Spektrumszugriff der Einsatz der beschriebenen Frequenzbereichssynchronisation die gleiche Leistung wie vergleichbare Zeitbereichsmethoden erzielt. Darüber hinaus übertrifft die Frequenzbereichssynchronisation ihr Zeitbereichsäquivalent in fragmentierten Spektrumsbelegungen und macht hierbei eine Komplexitätsreduktion bei gleichbleibender Leistung möglich. Somit trägt die hier entwickelte Frequenzbereichssynchronisation zum effizienten Design von Übertragungssystemen für fragmentierte Spektren bei und leistet damit einen Beitrag zur Bewältigung der Herausforderungen der zukünftigen Mobilfunknetze.

Schlagwörter: Frequenzbereichssynchronisation, Filterbankbasierte Mehrträgerverfahren, Adaptive Spektrumsnutzung.

CONTENTS

I	DISSERTATION	1
1	INTRODUCTION	2
1.1	Challenges in 5G cellular networks	2
1.2	Thesis contributions and outline	3
2	BACKGROUND, RELATED WORK, AND PROBLEM STATEMENT	5
2.1	Signal model for multicarrier systems	5
2.2	Shared spectrum access	14
2.3	Related work	20
2.4	Problem statement	23
3	FREQUENCY DOMAIN APPROACH TO SYNCHRONIZATION	25
3.1	Preamble	26
3.2	Frame detection	34
3.3	Frequency offset and symbol timing estimation	40
3.4	Channel estimation	56
4	CONCEPT EVALUATION	63
4.1	Synchronization concepts	63
4.2	Simulation-based evaluation	66
4.3	Computational complexity	72
4.4	Measurement-based verification	78
5	CONCLUSION AND FUTURE WORK	88
II	APPENDIX	90
A	COVARIANCE MATRIX OF FREQUENCY DOMAIN NOISE	91
B	REGULARITY CONDITIONS	93
C	ERROR FLOORS	95
D	TD CFO ESTIMATION WITH DIFFERENT PREAMBLES	99
E	MEASURED FER WITH CONFIDENCE INTERVALS	100
	BIBLIOGRAPHY	101
	GLOSSARY OF SYMBOLS	110
	GLOSSARY OF ACRONYMS	114
	INDEX	116
	SCIENTIFIC CAREER	117
	LIST OF PUBLICATIONS	119

Part I
DISSERTATION

INTRODUCTION

The introduction of GSM networks in the early 1990s and its further success laid the foundation of today's mobile connected world. What started as a mobile voice service with GSM as the second generation of cellular networks (2G)¹ evolved with the standards UMTS (3G) and LTE (4G) [52] towards a high-speed mobile data network. With the success of mobile services the number of customers and their traffic volume increased drastically over the past years. It is predicted to accelerate even further in the future as shown in a study conducted by Cisco [21]. As a consequence, more spectrum is and will be dedicated to wireless communication networks as part of the digital dividend [1] to facilitate the needed growth in network capacity. Nevertheless, suitable spectrum is a limited and expensive resource and it is fragmented by services other than mobile communication, e. g., terrestrial video broadcasting, that prevents the simple increase of the system's bandwidth in the range below 6 GHz. Hence, new cellular system designs need to cope with an increasing fragmentation of the available spectral resource.

1.1 CHALLENGES IN 5G CELLULAR NETWORKS

Despite the fragmentation and scarcity of available spectrum, which demands for an increase in spectral efficiency of the fifth generation of cellular networks (5G) currently under development, the type of traffic to be sent over cellular networks is predicted to change as well [21]. As of today video streaming generates the major share of mobile data traffic and is predicted to further increase. Additionally to the human-centric traffic, machine-type communication powered by the internet of things is predicted to increasingly contribute to the growing mobile traffic. As a result of this contradicting requirements on the cellular network, which is to support a few high data rate users as well as many low data rate devices, concepts for 5G networks are being developed and discussed in [58] and [92] as part of the EU research projects METIS and 5GNOW, respectively. Both concepts suggest the use of physical layer designs based on filterbank multicarrier (FBMC) to efficiently utilize the

¹ The first generation of cellular networks was based on analog technology. Even though GSM became the first digital system to be successfully deployed worldwide it is considered the second generation [52].

fragmented spectrum and to enable spectrum sharing. FBMC is favored over cyclic prefix (CP) orthogonal frequency division multiplex (OFDM), which is part of the current LTE physical layer in 4G, because classical OFDM would require a large number of guard bands to effectively realize spectrum sharing [39, 80]. The new physical layer enables a paradigm shift in the design of cellular networks from a coordinated system to a shared usage of the spectrum in an uncoordinated, i. e., asynchronous, fashion, as the authors in [92] propose. The paradigm shift from exclusive and coordinated to shared and uncoordinated spectrum access results in a change of spectrum utilization and coexistence scenarios, not only in the context of 5G, but also for other wireless systems, e. g., the enhancement of professional mobile radio systems by broadband data services, which is the focus of the EU research project Emphatic [63].

These new ways of accessing the spectrum implicate that existing solutions for coordination and synchronization, that are designed for the exclusive usage of spectrum by a single system, need to be rethought.

1.2 THESIS CONTRIBUTIONS AND OUTLINE

The frequency domain (FD) approach to synchronization enables coexistence as well as efficient handling of multiple users by independent processing of subbands in shared spectrum access networks. With this thesis we contribute analytical as well as practical results to the research about FD synchronization schemes, which are summarized in the following list.

- *We propose a resource-efficient preamble design and frame structure to enable spectrally efficient transmission in fragmented spectrum.*
- *We analytically evaluate the performance of frame detection and derive the lower bounds for offset estimations for the FD synchronization scheme. Furthermore, we compare them with common time domain (TD) methods to assess possible drawbacks of shifting the processing domain from time to frequency.*
- *We derive an optimal symbol timing offset (STO) estimator, and propose and evaluate practical STO, carrier frequency offset (CFO), and channel estimators based on the same preamble design.*
- *We develop FD synchronization concepts based on the previously derived estimators for the application in practical transmission schemes. Additionally, their performance and complexity are assessed and compared to TD solutions.*

- *We evaluate the described concepts by measurements to verify the feasibility of the FD approach in practice.*

These contributions are described in the remaining part of this thesis, which is organized as follows.

In Chapter 2 a generic multicarrier signal model is derived and its diverse characteristics are defined in the context of adaptive spectrum sharing. The results of a practical case study on fragmented spectrum usage with CP-OFDM and FBMC are presented as a motivation for the research question posed in this work. The chapter concludes with a discussion of the related work on FD synchronization that is followed by the presentation of the problem statement.

In Chapter 3 we motivate the use of our preamble design and investigate the performance of the proposed frame detection scheme. The derivation and evaluation of the lower bounds of the offset estimation is used in the following to benchmark the proposed estimators, which are derived under consideration of the criteria of optimality and practicability. Furthermore, in this chapter the re-use of the proposed preamble for channel estimation purposes is discussed and investigated and the influence of residual offsets is evaluated.

In Chapter 4 we develop a synchronization concept based on the presented FD estimation algorithms. We use a TD concept as a reference design for the following simulation-based evaluation of the estimation and BER performance as well as for the complexity analysis. The results from the simulation study reveal the most promising FD algorithms that are used in the measurement campaign for a system performance evaluation that takes practical aspects into account. The outcome of this thesis is summarized in Chapter 5, followed by a discussion on future work based on the FD approach to synchronization.

BACKGROUND, RELATED WORK, AND PROBLEM STATEMENT

In this chapter a generic signal model for filterbank multicarrier systems is introduced. The properties of FBMC are highlighted and their implications for a system design are shown by means of a practical case study on spectrum sharing. The research question is formulated as an outcome of the case study followed by a discussion of the related work.

2.1 SIGNAL MODEL FOR MULTICARRIER SYSTEMS

In today's wireless communication systems the multicarrier concept has been widely adopted in current standards, e. g., LTE and IEEE 802.11n [52], due to its ability to cope with intersymbol-interference and ease of channel equalization [60].

The concept of filterbank multicarrier transmission dates back to the 1960s and the work of Chang [61] who proposed a bandwidth-efficient analog concept for parallel transmission of pulse amplitude modulation (PAM) symbols. Saltzberg extended it to quadrature amplitude modulation (QAM) symbol transmission in [68]. Finally, it was adopted to digital systems by Bellanger and Daguët [11] and further studied by Hirosaki [35]. Thereafter, related FBMC concepts gained interest for application in LTE and are currently under discussion for the air interface of 5G cellular networks as a successor of CP-OFDM [58, 92].

In the following, the discrete-time baseband signal model of a generic uniform multicarrier system is derived based on the signal model presented in [25]. Modulation of the complex-valued symbols $q_{k,u}$ by the synthesis filterbank (SFB), where u is the block index and k is the subchannel index, results in the time-discrete output signal

$$s[nT_s] = \sum_{u \in \mathbb{U}} \sum_{k \in \mathbb{K}_u} q_{k,u} p_T[nT_s - uT_\Delta] e^{j2\pi f_\Delta k n T_s} \quad (2.1)$$

with the sample duration of T_s . k is chosen from the set of available subchannels \mathbb{K}_u out of the set $\mathbb{K} = \{-K/2 + 1, \dots, -1, 0, 1, \dots, K/2\}$ with a subchannel spacing of f_Δ . K is equivalent to the size of the inverse discrete Fourier transform (DFT) for the case that a discrete Fourier transform polyphase network

(DFT-PPN) approach to filterbank design is taken [86, 87]. The DFT-PPN design is assumed in the following if not otherwise stated. T_Δ is the time between successive symbols $q_{k,u}$, where \mathcal{U} is defined as the set of blocks that constitutes a frame. A block is also known as a multicarrier symbol in the literature. The time-discrete prototype filter functions for modulation and demodulation, $p_T[nT_s]$ and $p_R[nT_s]$, respectively, are real-valued, even-symmetric, and normalized with respect to the Euclidean norm. Except for the case of CP-OFDM they have a length of βT_Δ , with β representing the overlapping factor of the modulated symbols in the TD.

At the receiver side the received signal $r[nT_s]$ yields

$$r[nT_s] = (h[nT_s] * s[nT_s - \tau])e^{j2\pi f_\Delta \nu nT_s} e^{j\phi} + \eta[nT_s]. \quad (2.2)$$

τ and ν represent the STO and the normalized CFO, respectively. Thereby, ν is normalized with respect to the subchannel spacing f_Δ . The channel impulse response is given by $h[nT_s]$ and the common phase shift is defined by ϕ . $\eta[nT_s]$ describes zero-mean, circular-symmetric Gaussian noise, which is modeled as an additive contribution according to the commonly used additive white Gaussian noise (AWGN) model.

Demodulation with the analysis filterbank (AFB) results in the recovered symbols

$$\begin{aligned} \tilde{q}_{k,u} &= \sum_{n=-\infty}^{\infty} r[nT_s] p_R[nT_s - uT_\Delta] e^{-j2\pi f_\Delta k n T_s} \\ &= \sum_{n=-\infty}^{\infty} h_k s[nT_s - \tau] e^{j2\pi f_\Delta \nu n T_s} e^{j\phi} \\ &\quad \times p_R[nT_s - uT_\Delta] e^{-j2\pi f_\Delta k n T_s} + \Psi_{k,u} \end{aligned} \quad (2.3)$$

with the filtered noise samples $\Psi_{k,u}$. h_k are the coefficients of the channel transfer function which are derived from the channel impulse response $h[nT_s]$ by Fourier transform under the assumption that the channel transfer function is approximately constant over the bandwidth of one subchannel. Hence, h_k is considered independent of the offsets τ and ν in the following.

For the simplification of the notation, the cross and auto ambiguity functions are introduced. The cross ambiguity function $c(\tau, \nu)$ between pulse shape $p_T[nT_s]$ and $p_R[nT_s]$ is defined as

$$c(\tau + (u - u')T_\Delta, \nu) = \sum_{n=-\infty}^{\infty} p_T[nT_s - uT_\Delta - \tau] p_R[nT_s - u'T_\Delta] e^{j2\pi f_\Delta \nu n T_s} \quad (2.4)$$

with u and u' equal to the block index at the transmitter and receiver, respectively.

For $u = u'$ it simplifies to

$$\begin{aligned} c_u(\tau, \nu) &= \sum_{n=-\infty}^{\infty} p_T[nT_s - uT_\Delta - \tau] p_R[nT_s - uT_\Delta] e^{j2\pi f_\Delta \nu n T_s} \\ &= \sum_{n=-\infty}^{\infty} p_T[nT_s - \tau] p_R[nT_s] e^{j2\pi f_\Delta \nu (nT_s + uT_\Delta)}. \end{aligned} \quad (2.5)$$

In case that $p[nT_s] = p_T[nT_s] = p_R[nT_s]$, the cross ambiguity function leads to the auto ambiguity function

$$a(\tau + (u - u')T_\Delta, \nu) = \sum_{n=-\infty}^{\infty} p[nT_s - uT_\Delta - \tau] p[nT_s - u'T_\Delta] e^{j2\pi f_\Delta \nu n T_s}. \quad (2.6)$$

For $u = u'$ the expression can be simplified in correspondence to (2.5) as

$$\begin{aligned} a_u(\tau, \nu) &= \sum_{n=-\infty}^{\infty} p[nT_s - uT_\Delta - \tau] p[nT_s - uT_\Delta] e^{j2\pi f_\Delta \nu n T_s} \\ &= \sum_{n=-\infty}^{\infty} p[nT_s - \tau] p[nT_s] e^{j2\pi f_\Delta \nu (nT_s + uT_\Delta)}. \end{aligned} \quad (2.7)$$

Hence, the auto ambiguity function covers those cases in which the same filter¹ is used in the SFB and the AFB [52].

With the insertion of the definition from (2.1) in (2.3), the demodulated symbol yields

$$\begin{aligned} \tilde{q}_{k,u} &= e^{-j2\pi f_\Delta k \tau} e^{j\phi} (q_{k,u} h_k c_u(\tau, \nu) \\ &\quad + \sum_{u' \in \mathbb{U}} \sum_{\substack{k' \in \mathbb{K}_u \\ (u', k') \neq (u, k)}} q_{k',u'} h_{k'} c(\tau + (u - u')T_\Delta, \nu + k - k')) \\ &\quad + \Psi_{k,u}. \end{aligned} \quad (2.8)$$

The factor $e^{-j2\pi f_\Delta k \tau}$ stems from the relation between the time delay τ of a signal $x[nT_s]$ and the corresponding linear phase shift in dependence of the frequency of its Fourier-transformed FD representation X_k according to

$$\mathcal{F}\{x[nT_s - \tau]\} = X_k e^{-j\frac{2\pi}{T} k \tau}. \quad (2.9)$$

$\mathcal{F}\{\cdot\}$ denotes the DFT operation in this context.

Summarizing the interference terms as follows

$$i_{k,u}(\tau, \nu) = \sum_{u' \in \mathbb{U}} \sum_{\substack{k' \in \mathbb{K}_u \\ (u', k') \neq (u, k)}} q_{k',u'} h_{k'} c(\tau + (u - u')T_\Delta, \nu + k - k') \quad (2.10)$$

¹ Orthogonal FBMC schemes with $p_T[nT_s] \neq p_R[nT_s]$ are called bi-orthogonal filterbanks and discussed in more details in [69, 73]. Even though the derivations in this work can be applied to them, the focus is on orthogonal filterbanks.

results in the compact representation of the demodulated signal from (2.8)

$$\tilde{q}_{k,u} = e^{-j2\pi f_{\Delta} k \tau} e^{j\phi} (q_{k,u} h_k c_u(\tau, \nu) + \iota_{k,u}(\tau, \nu)) + \Psi_{k,u}. \quad (2.11)$$

For the ideal case of distortion-free transmission, the filterbank is considered near-perfect and perfect reconstructing if $\tilde{q}_{k,u} \approx q_{k,u}$ and $\tilde{q}_{k,u} = q_{k,u}$ hold, respectively. Hence, a multicarrier scheme is also called (near-) orthogonal if this condition is fulfilled [74]. Perfect reconstruction is assumed in the following for the work in this thesis, and any interference from near-perfect reconstruction is considered to be smaller than the interference from noise and thus neglected in the system model. More background on perfect reconstruction and orthogonality in multicarrier systems are given in [15, 40, 72, 73, 74, 88]. Furthermore, the reader is referred to [7, 33, 86, 87] for a description of the underlying principles of transmultiplexers and filterbanks.

2.1.1 Multicarrier architectures

The perfect reconstruction property can be achieved for different filterbank architectures. In [25], Farhang-Boroujeny divided these architectures into three categories:

- **CP-OFDM:** Multicarrier scheme based on rectangular prototype filters with additional cyclic prefix extension for transmission of complex-valued symbols.
- **FBMC-QAM:** Multicarrier scheme with non-overlapping subchannels based on suitable prototype filters for transmission of complex-valued symbols.
- **FBMC-PAM:** Multicarrier scheme with overlapping subchannels based on suitable prototype filters for transmission of real-valued symbols.

The categories are shortly discussed in the following sections.

2.1.2 CP-OFDM

CP-OFDM is the commonly used multicarrier scheme in wireless communication today due to its simple implementation and its low complexity. The prototype filter is based on the rectangular window, which leads to an IDFT and DFT operation of size K for modulation and demodulation, respectively.

In the following, $T = KT_s$ defines the time between two successive complex-valued blocks without taking the cyclic prefix into account. The insertion of

the cyclic prefix extension of duration T_{cp} leads to the overall block duration of $T_{\Delta} = T + T_{cp}$. Furthermore, the subchannel spacing is set to $f_{\Delta} = \frac{1}{T}$. Hence, the generic signal model from (2.1) adapted to CP-OFDM yields

$$s[nT_s] = \sum_{u \in \mathcal{U}} \sum_{k \in \mathcal{K}_u} q_{k,u} p_T[nT_s - u(T + T_{cp})] e^{j \frac{2\pi}{T} k n T_s} \quad (2.12)$$

with the rectangular prototype filter

$$p_T[nT_s] = \Pi \left[\frac{nT_s}{T_{\Delta}} \right] = \begin{cases} \frac{1}{\sqrt{K}}, & \text{for } -T_{\Delta}/2 < nT_s \leq T_{\Delta}/2 \\ 0, & \text{otherwise.} \end{cases} \quad (2.13)$$

For the demodulation stage the receive filter

$$p_R[nT_s] = \Pi \left[\frac{nT_s}{T} \right] = \begin{cases} \frac{1}{\sqrt{K}}, & \text{for } -T/2 < nT_s \leq T/2 \\ 0, & \text{otherwise} \end{cases} \quad (2.14)$$

has the length T . Hence, (2.3) leads to

$$\begin{aligned} \tilde{q}_{k,u} &= \sum_{n=-\infty}^{\infty} h_k s[nT_s - \tau] e^{j \frac{2\pi}{T} \nu n T_s} e^{j\phi} \\ &\quad \times p_R[nT_s - u(T + T_{cp})] e^{-j \frac{2\pi}{T} k n T_s} + \Psi_{k,u} \\ &= e^{-j \frac{2\pi}{T} k \tau} e^{j\phi} (q_{k,u} h_k c_u(\tau, \nu) + \iota_{k,u}(\tau, \nu)) + \Psi_{k,u}. \end{aligned} \quad (2.15)$$

With $T_{cp} = 0$, i. e., $p_T[nT_s] = p_R[nT_s]$, the OFDM scheme is orthogonal with subchannels indices $k_{\Delta} \in \mathbb{Z}$ and in case of an ideal channel, i. e., $\tau = \nu = \phi = 0$ and $h_k = 1$, according to the following condition

$$\begin{aligned} a((u - u')T, k_{\Delta}) &= \sum_{n=-\infty}^{\infty} p_T[nT_s - uT] p_R[nT_s - u'T] e^{j \frac{2\pi}{T} k_{\Delta} n T_s} \\ &= \delta_{u,u'} \delta_{k_{\Delta}}. \end{aligned} \quad (2.16)$$

$\delta_{u,u'}$ and $\delta_{k_{\Delta}}$ are Kronecker deltas defined as

$$\delta_{u,u'} = \begin{cases} 1, & \text{for } u = u' \\ 0, & \text{otherwise} \end{cases} \quad (2.17)$$

and

$$\delta_{k_{\Delta}} = \begin{cases} 1, & \text{for } k_{\Delta} = 0 \\ 0, & \text{otherwise.} \end{cases} \quad (2.18)$$

It is desirable to maximize the density of the symbols $q_{k,m}$ on the time-frequency lattice to achieve a high bandwidth efficiency of the multicarrier

scheme [25, 40]. However, the Balian-Low-theorem states that if an orthogonal multicarrier scheme based on complex symbol transmission deploys the maximum symbol density of $\varphi = \frac{1}{T_{\Delta}f_{\Delta}} = 1$, i.e., $T_{CP} = 0$ and $f_{\Delta} = \frac{1}{T}$, the pulse shape $p[nT_s]$ cannot be energy-limited both in time or frequency domain according to the $\mathbb{L}_2(\mathbb{R})$ norm [12, 13, 15]. Hence, an orthogonal filterbank scheme with maximum bandwidth efficiency does not support well-localized² prototype filters and prevents the introduction of any filtering directly at $p[nT_s]$ without distortion of the orthogonality. For the case that $T_{CP} > 0$, the cyclic prefix can be windowed and a reduction of the side lobes of the transfer function of $p[nT_s]$ is achieved at the cost of a reduced bandwidth efficiency of $\varphi = \frac{T}{T+T_{CP}} < 1$ [25, 91]. This approach is called windowed or filtered OFDM and still fulfills the perfect reconstruction condition. However, for good out-of-band reduction a longer T_{CP} is beneficial, resulting in a decrease in bandwidth efficiency.

2.1.3 FBMC-QAM

Instead of increasing the symbol duration by T_{CP} , the FBMC-QAM scheme increases the subchannel spacing f_{Δ} . In doing so the filter function $p[nT_s]$ can be arbitrarily chosen with the constraint that two adjacent subchannels do not overlap in FD to establish orthogonality. It follows a frequency division multiplexing approach in which every subchannel is separated from its adjacent subchannels. This approach is called FBMC-QAM or filtered multitone (FMT) and is described in [25, 55, 84]. It allows to transmit complex-valued symbols, but has the drawback of a bandwidth efficiency of $\varphi < 1$ due to the non-overlapping subchannels. FBMC-QAM is discussed for power line communications [85] and is taken into consideration as a physical layer candidate for 5G networks. Nevertheless, the decrease in bandwidth efficiency compared to the case with $\varphi = 1$ lets us opt for the analysis of the FBMC-PAM scheme, in particular the OQAM-OFDM scheme, which combines the support for pulse shaping and maximum bandwidth efficiency as described in the following section.

2.1.4 FBMC-PAM

FBMC-PAM offers two ways of efficient transmission of real symbols, cosine-modulated multitone (CMT) and OQAM-OFDM. The latter is also known as FBMC-OQAM or staggered multitone. The transmission of real symbols is

² Well-localized refers to the energy concentration of the filter in the time-frequency lattice.

necessary to avoid restrictions on the prototype filter design due to the Balian-Low theorem, as discussed later on in this section. Both schemes are closely related, as shown in [26]. However, OQAM-OFDM is the scheme that has already been intensively studied in the EU projects PHYDYAS, EMPHATIC, and METIS and is considered as one of the most promising physical layer candidates for 5G. For that reason, this work focuses on the OQAM-OFDM scheme in the following. In OQAM-OFDM the real and imaginary parts of the complex-valued QAM modulated symbols $q_{k,u}$ are staggered in time by half a symbol period $T_\Delta = T/2$. The real-valued symbols are constructed as follows

$$\begin{aligned} d_{k,m} &= \Re\{q_{k,u}\} \\ d_{k,m+1} &= \Im\{q_{k,u}\}, \end{aligned} \quad (2.19)$$

which leads to $\mathcal{C}\{\mathbb{M}\} = 2\mathcal{C}\{\mathbb{U}\}$. The symbols $d_{k,m}$ are multiplied by the factor $\theta_{k,m} = j^{\text{mod}(m+k,2)}$, which depends on the block index m and subchannel index k . It enables the real-field orthogonality of the OQAM symbols [74]. Modulation of the symbols $d_{k,m}$ by the SFB results in the time-discrete output signal

$$s[nT_s] = \sum_{m \in \mathbb{M}} \sum_{k \in \mathbb{K}_u} \theta_{k,m} d_{k,m} p[nT_s - mT/2] e^{j \frac{2\pi}{T} k n T_s} \quad (2.20)$$

with the set of OQAM symbols \mathbb{M} . (2.20) is derived from (2.1) with the symbol duration between QAM symbols set to $T = KT_s$ and a subchannel spacing equal to $f_\Delta = \frac{1}{T}$. The prototype filter function of length βT is defined as $p[nT_s] = p_T[nT_s] = p_R[nT_s]$. It follows from (2.3) that

$$\begin{aligned} \tilde{d}_{k,m} &= \sum_{n=-\infty}^{\infty} h_k s[nT_s - \tau] e^{j \frac{2\pi}{T} \nu n T_s} e^{j\phi} \\ &\quad \times p[nT_s - mT/2] e^{-j \frac{2\pi}{T} k n T_s} + \Psi_{k,m} \\ &= e^{-j \frac{2\pi}{T} k \tau} e^{j\phi} (\theta_{k,m} d_{k,m} h_k a_m(\tau, \nu) + \iota_{k,m}(\tau, \nu)) + \Psi_{k,m} \end{aligned} \quad (2.21)$$

with the interference term from (2.10) adapted to yield

$$\begin{aligned} \iota_{k,m}(\tau, \nu) &= \sum_{m' \in \mathbb{M}} \sum_{\substack{k' \in \mathbb{K}_u \\ (m', k') \neq (m, k)}} \theta_{k',m'} d_{k',m'} h_{k'} \\ &\quad \times a(\tau + (m - m')T/2, \nu + k - k'). \end{aligned} \quad (2.22)$$

It follows from the structure of OQAM-OFDM that the interference $\iota_{k,m}(0, 0)$ for $h_k = 1$ is either real or imaginary-valued, which only depends on the parameters k and m [74]. Hence, the QAM symbols $q_{k,u}$ can be recovered by taking the real part of the received symbol $\tilde{d}_{k,m}$ according to

$$\tilde{q}_{k,u} = \Re\{\theta_{k,m}^* \tilde{d}_{k,m}\} + j \Re\{\theta_{k,m+1}^* \tilde{d}_{k,m+1}\}. \quad (2.23)$$

OQAM-OFDM circumvents the limitation in the choice of prototype filters set by the Balian-Low theorem by establishing the orthogonality only in the real-field. Hence, the orthogonality condition from [74] formulated with the ambiguity function yields

$$\begin{aligned} & \Re \left\{ \sum_{n=-\infty}^{\infty} p[nT_s - mT/2]p[nT_s - m'T/2]e^{j\frac{2\pi}{T}(k-k')nT_s} \right. \\ & \quad \left. \times j^{\text{mod}(m-m'+k-k',2)} \right\} \\ & = \Re \left\{ a((m-m')T/2, k-k') j^{\text{mod}(m-m'+k-k',2)} \right\} = \delta_{m,m'}\delta_{k-k'}. \end{aligned} \quad (2.24)$$

This condition can be fulfilled in case of an ideal channel by a suitable prototype filter design. More on the orthogonality of OQAM-OFDM and its relation to Gabor frame theory can be found in [14].

By alternating between the real and imaginary subspace for transmission of the real-valued symbols, the OQAM-OFDM scheme allows to double the real-valued symbol density such that $\varphi = \frac{T}{T/2} = 2$ [25]. As one complex-valued symbol carries twice the information of a real-valued symbol the maximum bandwidth efficiency is achieved.

2.1.5 Prototype filter design

It is beneficial to use well-localized prototype filters in both time and frequency domain to increase the robustness against synchronization errors which improves the system's performance in double-dispersive channels [41] and lowers out-of-band emissions [25]. Hence, OQAM-OFDM offers a new degree of freedom for the prototype filter design compared to classical OFDM.

In CP-OFDM $p[nT_s]$ is fixed to a rectangular prototype filter in TD which results in a poor localization of the filter's transfer function in the FD.

However, for the case of OQAM-OFDM different approaches exist that lead to well-localized prototype filters in both time and frequency domain and that fulfill or come close to the discrete orthogonality condition in (2.24). The following list of filter candidates does not claim to be complete, but should provide an overview of the design procedures of prototype filters commonly used in the literature. Further studies on prototype filter design for OQAM-OFDM can be found in [14, 16, 23, 24, 74].

- **Square root raised cosine filter:** A common filter design for band limited FIR filters [18], which is as well used for single carrier transmission. A closed-form expression of the prototype filter can be obtained.

- **Isotropic orthogonal transformation algorithm (IOTA):** A procedure that results in an orthogonal prototype filter design derived from the family of the extended Gaussian functions. A Gaussian basic pulse shape is maximally localized in both time and frequency domain, but it is not orthogonal. Hence, it cannot be applied directly in orthogonal system designs. A further generalization of the IOTA is provided in [15]. It bases on the discrete Zak transform of suitable even-symmetric and finite pulses. The IOTA-based pulses allow for adaption of their energy concentration in the time-frequency lattice according to the channel conditions, as discussed in [41].
- **Filter designs based on the frequency sampling technique (FST):** A pulse design technique that is based on the discrete frequency representation of the pulse. This procedure is described in [89] and yields well-contained pulses in the frequency domain.

In this work the pulses $p[nT_s]$ used for OQAM-OFDM are based on the frequency sampling technique. The FST offers a simple design procedure which is based on a single parameter in case that β is equal to 3 or 4 and offers a good spectral containment. The most common prototype filters considered in literature about OQAM-OFDM results from the PHYDYAS project and are constructed based on the FST. For that reason and for its good spectral localization, these prototype filters are chosen for our investigations in this work.

For illustration of the localization properties, the ambiguity functions for the rectangular prototype filter with $T_{cp} = 0$ as used in OFDM and a prototype filter based on the FST are given in Figure 2.1, where the vertical grid represents multiples of the symbol duration T and the horizontal grid represents the subchannel spacing of f_{Δ} . For the use in shared spectrum networks, the low out-of-band leakage is desired to minimize interference to and from other subbands. The prototype filters used for OQAM-OFDM already have this property because the transfer function of the pulse shaping filter is only allowed to overlap with its neighboring subchannels to establish orthogonality. It follows from the Heisenberg-Gabor uncertainty principle [25] that the prototype filter cannot be maximally concentrated in both time and frequency domain. The rectangular filter, shown in Figure 2.1a, is well-localized on the time grid but shows a poor localization on the frequency grid. The FST filter, however, offers a good trade-off between time and frequency localization, as presented in Figure 2.1b. Its energy is concentrated well within the horizontal grid ranging from $\nu = -2$ to 2 and is not spread out as shown in Figure 2.1a for the rectangular filter. Hence, it is assumed in this work that only filters are used whose transfer function overlaps with the adjacent subchannels only.

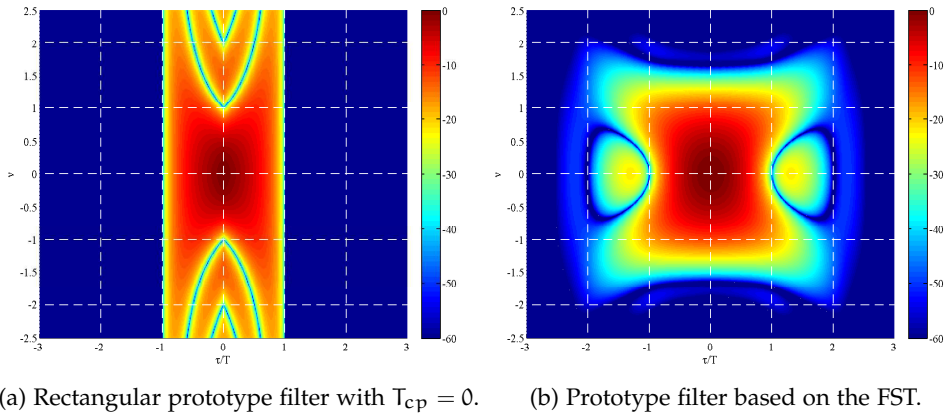


Figure 2.1: Illustration of the ambiguity functions in dB for different prototype filters plotted over the time-frequency lattice.

2.1.6 Concluding remarks

In the previous sections a generic signal model for multicarrier transmission based on the ambiguity function has been presented and is used for the definition of the signal models for CP-OFDM and OQAM-OFDM. Following a discussion on the property of OQAM-OFDM to deploy well-localized prototype filter functions, its advantage over CP-OFDM is illustrated with the help of ambiguity functions. The results show that OQAM-OFDM has the potential to increase spectrum utilization by using prototype filters where the energy is well-localized in time and frequency. This potential is further investigated in the following study on shared spectrum access.

2.2 SHARED SPECTRUM ACCESS

The good frequency localization of the prototype filter used for OQAM-OFDM in contrast to the rectangular prototype filter becomes obvious from Figure 2.1. It is apparent that the introduction of OQAM-OFDM enables more efficient resource allocations with application in multi-user access [54], e. g., frequency division multiple access with asynchronous or relaxed uplink synchronization, shared spectrum usage, e. g., allocation of several coexisting systems within the same band as discussed in [36], and band separation, e. g., intersystem coexistence between adjacent bands.

The evaluation of these applications can be considered as an issue of sub-channel rejection at receiver side as well as out-of-band leakage at transmitter side and their effect on other users, other inband systems, or other systems in adjacent bands. Simulation-based coexistence studies have been conducted

in [39, 75, 80, 93] to show the potential of OQAM-OFDM in these scenarios. One approach to dynamic spectrum access is the spectrum pooling concept for OFDM systems which uses locally or temporarily not utilized parts of the spectrum in an overlay manner [90]. The concept of non-contiguous OFDM (NC-OFDM) provides a physical layer technique to increase the efficiency in spectrum utilization in heterogeneous networks. However, it results in various co-channel coexistence situations with either one or more users or systems accessing the fragmented spectral resource. In the following a case study is presented that uses the NC-OFDM concept to establish coexistence between narrow band users and a multicarrier system where the focus is on the performance of the multicarrier system in dependence of the architecture.

2.2.1 *A measurement-based case study of NC-OFDM*

A practical evaluation of NC-OFDM concepts that deploy CP-OFDM and OQAM-OFDM has been reported in [82]. Therein it is shown that OQAM-OFDM can increase the efficient utilization of the spectrum with respect to practical performance metrics. The study is described shortly in the following to illustrate that the theoretically derived properties of prototype filters for OQAM-OFDM can be transferred to practical relevant benefits. Furthermore, the study points out that additional measures compared to exclusive spectrum usage are necessary for practical implementations of shared spectrum access. Our study concentrates on the evaluation of NC-OFDM system designs in terms of achievable frame error rate (FER) versus signal-to-interference ratio (SIR) in dependence of the number of subchannels used as guard subchannels and its practical validation by offline measurements.

For the case study we chose a scenario in which a multicarrier system coexists with a narrowband system, which is emulated by a wireless microphone link, at a center frequency of 750 MHz. This scenario is motivated by the discussion about white space utilization in the UHF band in the context of cognitive radio networks [57] but is not limited to it. A similar scenario that is relevant to cellular networks is the refarming of GSM spectrum to LTE where one or more GSM links need to be conserved. Such a scenario is for example described in [78]. The multicarrier schemes adopt the IEEE 802.11a standard [5], referred to as WiFi in the following, for the system design. Even though conventional WiFi systems are operating at 2.4 and 5 GHz, there are efforts to adopt the system design for usage in the TV white space. Besides experimental results to deploy WiFi in the UHF band [9], new approaching standards, e. g., IEEE 802.11af [6], enable WiFi-like connectivity with the aim

to increase spectrum utilization. While common WiFi systems itself offer no opportunity to adaptively change their spectrum allocation, i. e., subchannel allocation, we added the concept of spectrum pooling by the introduction of the set of utilized subchannel indices \mathbb{K}_u .

The received signal with interference $r_w[nT_s]$ is derived from the signal model in (2.2) according to

$$r_w[nT_s] = (h[nT_s] * s[nT_s - \tau])e^{j\frac{2\pi}{T}vnT_s}e^{j\phi} + w[nT_s] + \eta[nT_s] \quad (2.25)$$

and includes the contribution from other systems $w[nT_s]$, called interference in the following. While the introduction of a notch at the spectral parts occupied by $w[nT_s]$ is straightforward in case of multicarrier transmission, the commonly used TD synchronization methods at receiver side are degraded by the interfering signal. The TD synchronization algorithms do not make use of the AFB, and the possibility to remove the interference at the demodulation stage is left unused. However, in [56] a method is proposed to cancel the spectrum parts occupied by $w[nT_s]$. It transforms $r[nT_s]$ in the FD followed by interference cancellation by multiplying the interfered frequency bins with zero. The interference-free signal is transformed back to the TD before passing it to the TD synchronization algorithm. For the measurements the cascade of AFB, multiplication of each subchannel with either 1 or 0, and SFB is approximated by a filter operation of the received signal $r[nT_s]$. It can be compactly written as

$$r'_w[nT_s] = r_w[nT_s] * h_C[nT_s] \quad (2.26)$$

with the interference canceling filter $h_C[nT_s]$ defined according to

$$h_C[nT_s] = \sum_{k \in \mathbb{K}_u} p[nT_s] e^{-j\frac{2\pi}{T}knT_s}. \quad (2.27)$$

The filtered signal $r'_w[nT_s]$ is then passed to the TD synchronization scheme. The signal $r_w[nT_s]$ is used for data recovery after synchronization, i. e., the offsets τ and ν are close to zero in (2.25). The cascade of the interference canceling filter $h_C[nT_s]$ from (2.27) and the channel impulse response $h[nT_s]$ can be treated as a new channel impulse response $h'[nT_s] = h[nT_s] * h_C[nT_s]$. However, the noise contribution $\eta[nT_s]$ formerly considered to be white will be colored according to $\eta'[nT_s] = h_C[nT_s] * \eta[nT_s]$ for the TD synchronization. Furthermore, the previously linear phase rotation as a result of the CFO is distorted. Even though the performance of the CFO estimation is slightly degraded [47], the introduction of $h_C[nT_s]$ is advantageous as becomes obvious from the following results. The use of a prefiltering stage enables TD synchronization even at low SIR. The SIR is defined here as the ratio between

the received power from the interference-free received signal $r'_w[nT_s]$ and the received interference power from $w[nT_s]$ across the whole bandwidth. In the measurements the SIR is adjusted with the help of a variable attenuator which is inserted in the cable connecting the interfering transmitter. The attenuated signal from the interfering transmitter is combined with the signal from the multicarrier transmitter to be fed to the multicarrier receiver. The adjustments yield an SIR range from -35 dB to 5 dB. The power spectral density (PSD) of the combined signal $r_w[nT_s]$ at a sampling rate of $f_s = 10$ MHz is illustrated in Figure 2.2. The channel is considered frequency-flat due to the use of cable

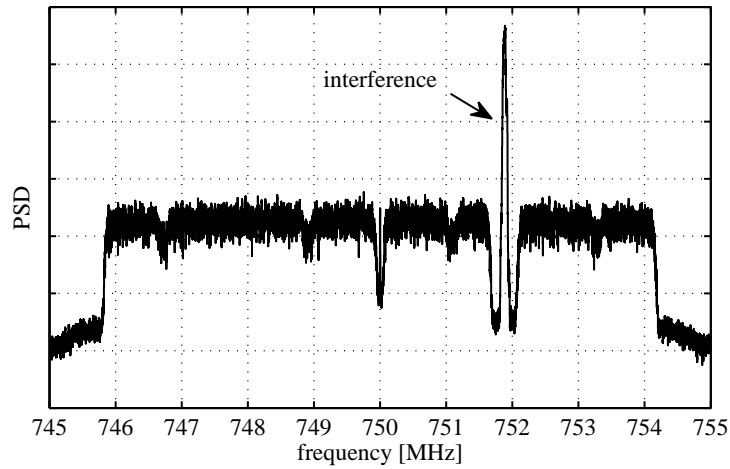


Figure 2.2: Power spectrum density at the receiver.

connections instead of wireless transmission. The signal-to-noise ratio (SNR) level is defined as the ratio between received signal power and received noise power across the whole bandwidth and is kept constant at a level of 21 dB. Hence, the dominant distortion stems from the interference rather than from the noise contribution.

According to the WiFi specification, the number of subchannels is $K = 64$ and the data symbols are QPSK modulated with a code rate of $2/3$. Convolution coding is applied at the transmitter and hard-bit Viterbi decoding is performed at receiver side. The subchannel spacing is $f_\Delta = f_s/K = 156.25$ kHz. For the case of CP-OFDM the cyclic prefix length is set to $T_{cp} = T/4$ and for the case of OQAM-OFDM the pulse $p[nT_s]$ is designed with $\beta = 4$ and a design parameter equal to 0.97196 .

Three different NC-OFDM allocations are used in the measurements that are represented by the sets of subchannel indices \mathbb{K}_0 , \mathbb{K}_1 and \mathbb{K}_3 , which correspond to the number of used subchannels with $K_0 = 52$, $K_1 = 51$, and $K_3 = 49$, respectively. The set of subchannel indices \mathbb{K}_0 is defined as $\mathbb{K}_0 = \{-26, \dots, -1, 1, \dots, 26\}$ and excludes the center carrier as well as guard

subchannels at the edges of the spectrum. The sets \mathbb{K}_1 and \mathbb{K}_3 are derived from it by removing one and three indices, respectively, from \mathbb{K}_0 at the corresponding frequency location of the interference. For the design of the prefiltering stage in (2.27) the set \mathbb{K}_3 is used for all three scenarios to enable a fair comparison.

The performance of the multicarrier systems is evaluated in terms of frame loss rate (FLR) and FER over SIR with $5 \cdot 10^2$ transmitted frames per measurement trial. The FLR is thereby defined as the ratio of the number of detected and transmitted frames and the FER is defined as the ratio of the number of error-free received frames and the number of detected frames. A frame is error-free if it yields a bit error rate (BER) equal to zero after channel decoding. The measured FLR based on the received signal $r_w[nT_s]$, tagged as direct, and $r'_w[nT_s]$, tagged as prefiltering, is shown in Figure 2.3. From the

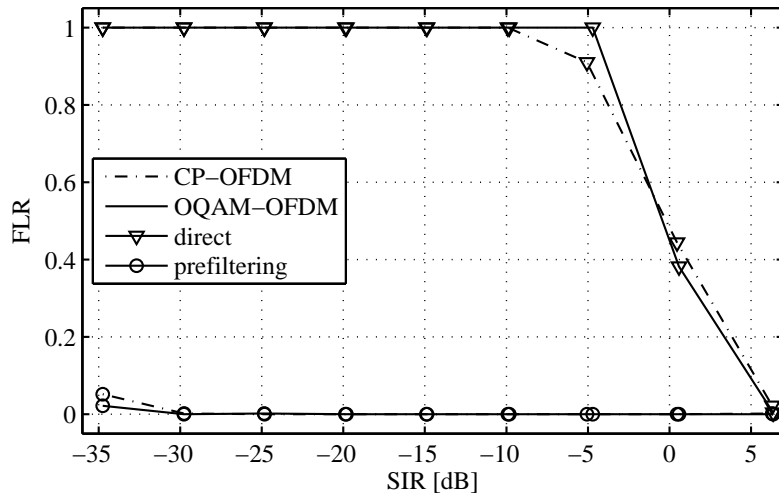


Figure 2.3: FLR versus SIR at an SNR of 21 dB in the presence of narrowband interference.

analysis it becomes obvious that at a low SIR the prefiltering stage enables the utilization of NC-OFDM systems with common receiver designs that has been developed for exclusive spectrum usage. The similar performance of CP-OFDM and OQAM-OFDM results from the use of the well-localized prototype filter $p[nT_s]$ in (2.27) for both systems. However, the outcome of the FER analysis, provided in Figure 2.4, shows the clear advantage of OQAM-OFDM over CP-OFDM. The FER is evaluated with respect to the number of guard subchannels left unused around the frequency location of the interfering system. The indicated intervals represent a confidence interval of 0.95. Starting with no guard subchannel, which corresponds to the used set \mathbb{K}_0 , the number of guard subchannels is increased to 1 (\mathbb{K}_1) and 3 (\mathbb{K}_3).

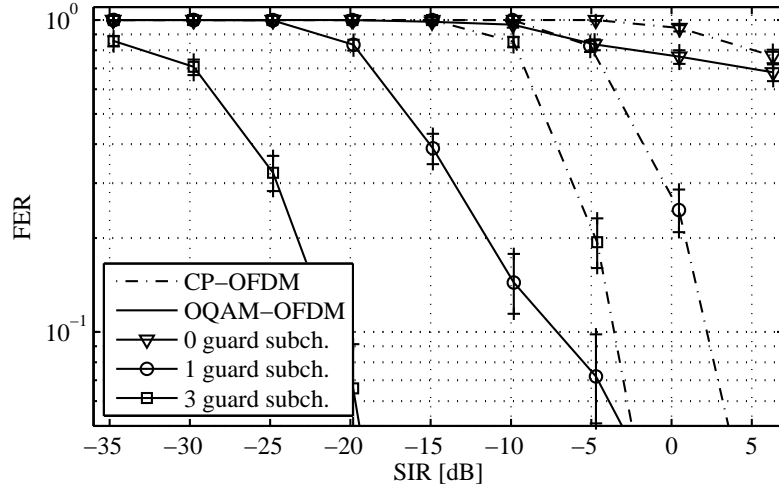


Figure 2.4: FER versus SIR at an SNR of 21 dB.

The results show that the OQAM-OFDM architecture turns the property of well-localized prototype filters, which is illustrated in Figure 2.1, into a robustness against narrowband interference and achieves a FER of 10^{-1} at an SIR of -21 dB and -6.5 dB for 3 and 1 guard subchannels, respectively. The CP-OFDM scheme needs an SIR that is up to 17 dB higher compared to the OQAM-OFDM case to achieve the same FER.

2.2.2 Concluding remarks

The study illustrates in a practical manner that the use of filterbanks with well-localized prototype filters leads to a significant increase in spectrum utilization, because less guard bands are needed. Hence, an appropriate FBMC physical design improves the spectral efficiency of wireless networks and enables simple spectrum sharing. Nevertheless, the study also shows that a suitable synchronization stage is essential to enable transmission in shared spectrum scenarios and that an alternative synchronization approach in the frequency domain seems favorable.

2.2.3 Research question arising from the case study

The need for separate synchronization of each non-contiguous user band leads to the desire to deploy the advantages of the AFB for demodulation at the synchronization stage. Based on the idea of FD synchronization the following research question is formulated.

Can the frequency domain approach to synchronization be advantageous in terms of performance and complexity in shared spectrum scenarios compared to equivalent time domain solutions?

An answer to this question will be given in the course of this thesis. In general we assume that common preamble-based TD algorithms, as for example presented in [29], can be applied with prefiltering with a minor loss in performance, as discussed in Section 2.2.1. For that reason, TD algorithms that deploy other ways of interference cancellation are not considered here. They are mostly applied in multi-user scenarios and base on the maximum-likelihood estimation as for example described in [28, 30, 37]. Because the focus of this work is on FD processing, suitable TD synchronization schemes and respective lower bounds on the estimation errors are only considered for reference where needed in the progress of this work.

2.3 RELATED WORK

In this section the related work on the topic of data-aided FD synchronization for OQAM-OFDM is summarized. The focus is on data-aided synchronization schemes because they have proven to be robust and practical in many frame-based applications, e. g., LTE and WiFi.

In 2010 Stitz et. al. describe a pilot-based approach to FD synchronization in their work [77]. The pilots, that are used for STO, CFO, and channel estimation, are embedded in the payload part of the frame and protected against intersystem interference by auxiliary pilots [38]. The authors assume that the received frame is coarsely synchronized, i. e., the frame start and the CFO is roughly known and compensated by means of TD solutions.

Their approach to STO estimation utilize the relation defined in (2.9). The closed-form expression for the estimation of the STO τ based on the received symbols at pilot location $\tilde{b}_{k,m}$ from (2.21) yields

$$\hat{\tau}_{k,m}^{\text{Stitz}} = \frac{\angle(\theta_{k,m}^{-1} \tilde{b}_{k,m}) - \angle(\theta_{k+k_{\Delta},m}^{-1} \tilde{b}_{k+k_{\Delta},m})}{2\pi k_{\Delta}}. \quad (2.28)$$

$b_{k,m}$ represents the pilot symbols that are part of the transmitted symbol stream $d_{k,m}$ in (2.20). k_{Δ} defines the spacing between pilot-bearing subchannels and has a direct influence on the unambiguous estimation range of $\hat{\tau}_{k,m}^{\text{Stitz}}$. The estimation bases on the difference between symbols with the same block index m . Hence, the metric is robust against a common phase shift. However, it becomes obvious from (2.21) that the estimate is influenced by the interference $\iota_{k,m}$ as well as by the channel coefficients h_k . The authors reduce

the effect of $\iota_{k,m}$ by boosting the pilot symbols to effectively reduce the influence of the interference on the estimates. Nevertheless, they assume that the coherence bandwidth of the channel, i. e., the correlation between h_k and h_{k+k_Δ} , is large enough such that averaging over all available estimates $\hat{\tau}_{k,m}^{\text{Stitz}}$ yields a sufficient estimate. In the progress of their work a combined STO and channel estimation scheme is proposed to improve the result by iteratively estimation and compensation with a three-tap equalizer. The deployment of a three-tap equalizer enables the compensation of the STO directly in the FD at the cost of a higher complexity compared to single-tap solutions. A similar approach to STO estimation has been reported for CP-OFDM in [20]. However, in CP-OFDM the blocks do not overlap in time and, hence, preceding and following blocks have no influence in a coarsely synchronized system as it is the case for OQAM-OFDM. CFO estimation based on a common pilot-based algorithm that measures the phase difference in time direction has been presented by the same authors in [76]. The CFO is obtained by evaluation of the phase difference between pilots in time direction in correspondence to the estimation of the STO by calculation of the phase difference between pilots in frequency direction. Hence, the expression of the CFO estimate yields

$$\hat{\nu}_{k,m}^{\text{Stitz}} = \frac{\angle(\theta_{k,m}^{-1} \tilde{b}_{k,m}) - \angle(\theta_{k,m+m_\Delta}^{-1} \tilde{b}_{k,m+m_\Delta})}{\pi m_\Delta}. \quad (2.29)$$

m_Δ defines the difference in the block index between pilot symbols. Assuming a sufficiently large coherence time of the channel, the estimate $\hat{\nu}_{k,m}^{\text{Stitz}}$ is mainly influenced by the term $\iota_{k,m}$ and noise. Averaging over multiple pilot symbols yields a method to reduce the effects of interference and noise similar to the case of STO estimation. The results, which are provided as the BER performance over the time-frequency plane, reveal that the proposed scheme can achieve sufficient performance only if the interference from the surrounding payload symbols is iteratively canceled. Furthermore, the proposed scheme assumes some form of pre-synchronization which makes it unsuitable for initial frame synchronization.

In 2010 Amini and Farhang-Boroujeny described in [8] CFO and STO estimation algorithms for CMT and OQAM-OFDM based on a preamble block, which is isolated from the payload part and in which only every second sub-channel is occupied. Hence, the interference from surrounding symbols to the pilot symbol is avoided. A formal description of the preamble is given by

$$b_{k,m} = \begin{cases} \lambda_k, & k \in \mathbb{K}_2 \text{ for } m = 0 \\ 0, & \text{otherwise} \end{cases} \quad (2.30)$$

with the BPSK sequence $\lambda_k \in \{-1, 1\}$. m is set to 0 to indicate the block index at the start of a frame. The subset \mathbb{K}_2 of \mathbb{K}_u contains in good ap-

proximation only $K_2 = K_u/2$ subchannels. It follows that either even- or odd-numbered indices out of the set of utilized subchannels K_u are used for the pilot symbols. K_u is defined as the number of subchannels used for transmission. The preamble structure enables the CFO to be estimated in the FD using a maximum-likelihood (ML) approach. The CFO is estimated and corrected prior to STO estimation. The optimal timing is achieved by sample-wise demodulation of the received TD signal and a subsequent maximum search of the received power at the occupied subchannels in the FD. Other than in [77] the authors avoid interference by isolation of the pilot symbols from the payload part of the frame. However, the zero symbols lead to an inefficient overall frame structure. Furthermore, the estimations are based on maximum searches which lead to a high computational complexity of the algorithms. Especially for the STO estimation, the sample-wise demodulation of the received signal prevents the use of low complexity, DFT-based block-wise processing.

The work in [65] from Saeedi-Sourck and Sadri utilize a modified version of the preamble structure proposed in [8]. The authors keep the concept of an isolated preamble, but utilize M_b preamble blocks instead of only a single block according to

$$b_{k,m} = \begin{cases} \lambda_k, & k \in K_2 \text{ for } m \in \{0, 2, \dots, M_b\} \\ 0, & \text{otherwise.} \end{cases} \quad (2.31)$$

Only every second OQAM-OFDM block is occupied with pilot symbols to avoid self-interference. The modified preamble enables a closed-form CFO estimation by the repetition of identical preamble symbols, which lowers the complexity in comparison to [8]. This closed-form approach is also presented in [66]. The STO is estimated based on the received energy in the FD, as previously discussed in [8].

In [67] the same authors present a near-ML estimator for CFO and STO based on a preamble from [65], where the number of occupied OQAM-OFDM blocks is reduced to two. Hence, the definition of the preamble yields

$$b_{k,m} = \begin{cases} \lambda_k, & k \in K_2 \text{ for } m \in \{0, 2\} \\ 0, & \text{otherwise.} \end{cases} \quad (2.32)$$

The authors propose an iterative approach to CFO and STO estimation that comes close to the ML estimator. They achieve a better performance with their CFO estimation algorithm in comparison to [8] and [31].

Van Caekenberghe et. al. investigate in [17] the joint CFO and STO estimation in the FD using a preamble design defined as

$$b_{k,m} = \begin{cases} \lambda_k, & k \in \mathbb{K}_2 \text{ for } m \in \{0,4\} \\ 0, & \text{otherwise.} \end{cases} \quad (2.33)$$

In contrast to the approaches discussed previously, they utilize an early-late detector for STO estimation, which needs the large block spacing of four blocks to work. Not only results the large block spacing in an undesired large resource allocation of the preamble, it also limits the estimation range of the proposed closed-form CFO estimator which is based on (2.29). Hence, this approach requires additional resources compared to the FD approach described in [67] and results in a limited estimation range of the CFO.

TD algorithms for synchronization that are based on the ML approach are also suitable for synchronization in shared spectrum, e. g., multi-user synchronization, as discussed in [30, 31]. However, they do not deploy the band-rejection properties of the AFB and, hence, their performance will suffer from high-power interfering signals. For that reason, they are not considered to be an appropriate alternative for FD processing in this work.

The previously discussed work assumes that frame detection is achieved by other means prior to offset estimation. However, in a practical system with no strict timing coordination, i. e., WiFi, frame detection is the initial step of synchronization. Nevertheless, no analysis on FD frame detection exists in the context of OQAM-OFDM. Only the work from Stitz et. al. [34], in which the authors present a preamble-based synchronization scheme for exponential modulated filterbanks, briefly describes initial frame detection in the FD. However, in their approach to FD synchronization the authors introduce a multi-tap equalization to compensate for the effect of timing offsets. Hence, it makes an accurate estimation of the STO unnecessary. This approach is further studied in [22] and [62] but increases the overall system complexity. For that reason, we focus on the offset estimation and single-tap equalization in the FD in combination with offset compensation in the TD.

2.4 PROBLEM STATEMENT

Even though the related work provides ideas to achieve FD synchronization, the proposed solutions either suffer from a limited estimation range due to self-interference or they need a high computational effort combined with an inefficient frame structure. Furthermore, an analysis of the lower bound on the variance of the estimation error as well as a direct comparison with TD

solutions in terms of performance and complexity is still missing. Hence, the research question is not answered in the literature yet.

To provide an answer to the research question it is split into several questions which are presented in the following.

1. *What is a suitable preamble design for FD synchronization in terms of resource efficiency and estimation range?*
2. *What is the performance of frame detection as part of initial frame synchronization in the FD?*
3. *Is the lower bound on the variance of the estimators in FD the same as in TD? What are optimal and practical realizations of STO and CFO estimators?*
4. *How does the FD synchronization perform in terms of accuracy and complexity compared to TD approaches?*

These questions will guide through the following chapters and finally result in a conclusive answer to the research question.

FREQUENCY DOMAIN APPROACH TO SYNCHRONIZATION

In this chapter a resource-efficient frame structure for FD synchronization is developed. Based on the preamble design, the probability of missed detection and false alarm of the presented frame detection metric is derived and evaluated. Furthermore, the lower bounds on the variance of the STO, CFO, and channel coefficient estimations are calculated and the optimal estimators are discussed. Additionally, more practical estimators for the STO are proposed and evaluated. Parts of the work that is presented in this and the following chapters have already been published in [83].

The following system parameters and settings are used for the simulation-based evaluation if not otherwise stated.

- The number of subchannels K is set to 64 with $\mathbb{K}_u = \{-K/2 + 1, -K/2 + 1, \dots, K/2\}$ and $\mathbb{K}_2 = \{-K/2 + 1, -K/2 + 3, \dots, K/2 - 2, K/2\}$. It follows that the number of all usable subchannels is $K_u = 64$ and the number of subchannels occupied by the preamble pilots is $K_2 = 32$. For the simulation results in Chapter 3 the number of payload symbols and auxiliary pilots is set to zero. In Chapter 4 the number of OQAM-OFDM payload symbols is set to four and QPSK modulation is applied. The number of realizations used in the Monte-Carlo simulations is 10^5 .
- The prototype filter $p[nT_s]$ results from the FST approach to filter design introduced in [89]. The filter is defined by the overlapping factor $\beta = 3$ and the design parameter equal to 0.91697069.
- The STO τ is discrete uniformly distributed in steps of T_s in the range of $\{-T/4 + T_s, T/4 - T_s\}$, if not otherwise stated. The normalized CFO ν is uniformly distributed in the range of $(-0.5, 0.5)$. For the case of Rayleigh fading τ refers to the delay of the rounded mean path delay of each realization.
- The Rayleigh fading channel is emulated with an exponential-decaying power delay profile (PDP) according to $E[|h[nT_s]|^2] \propto e^{-\frac{1}{2}n}$ with $n \in \{0, 1, \dots, K/8 - 1\}$. Furthermore, a normalization of the PDP is applied such that $\sum_{n=0}^{K/8-1} E[|h[nT_s]|^2] = 1$. The channel impulse response $h[nT_s]$ is defined such that its mean delay $\bar{\tau}_n$, which is rounded to the next mul-

tuple of T_s , is centered at time instance $nT_s = 0$ of the channel impulse response. The mean delay $\bar{\tau}_h$ is defined in [52] as $\bar{\tau}_h = \frac{\sum_{\tau_h} \tau_h h[nT_s]^2}{\sum_{\tau_h} h[nT_s]^2}$. The channel is static for each run but is varied between runs.

- The channel coefficients which are estimated at the pilot locations are linearly interpolated to obtain estimation values for the remaining subchannels. The one-tap channel equalization bases on the estimated values for the analysis of the system level performance and it is only assumed for the case of ideal synchronization that the coefficients are known. Furthermore, it is assumed that the approximation of a flat fading channel per subchannel holds in the sequel of this thesis.

3.1 PREAMBLE

In this section the preamble design is developed. Therefore, the achievable estimation range, the influence from interference, and the use of auxiliary pilots are discussed which leads to a design proposal that is based on the criteria efficiency and functionality. In this context efficiency means the use of a minimum amount of resources to achieve the desired functionality preferably with algorithms of low complexity, e. g., closed-form estimators or estimators based on the auto correlation function. Furthermore, TD reference designs of preambles are discussed for later use in this work.

3.1.1 Pilot symbol distribution

The functionality that has to be achieved is frame detection and offset estimation. The capability to estimate the channel is not in the focus of this work. However, the proposed preamble design enables common channel estimation schemes to be deployed, which is discussed in this work in the context of synchronization.

In FD processing the SFB and AFB introduce interference to the pilot symbols due to the interleaved structure of the OQAM-OFDM scheme even though no STO and CFO is present, which follows from the definition of the interference in (2.22). The amount of interference is further increased by non-zero values of the STO and CFO. Hence, a preamble design that mitigates the intersymbol interference (ISI) and intercarrier interference (ICI) at receiver side after demodulation is favorable. From the ambiguity function in Figure 3.1 it becomes apparent that a pilot spacing with $m_\Delta \geq 2$ and $k_\Delta \geq 2$ leads to significant reduction of interference from neighboring pilots. The degradation of the received amplitude of the signal and the introduction of interference from

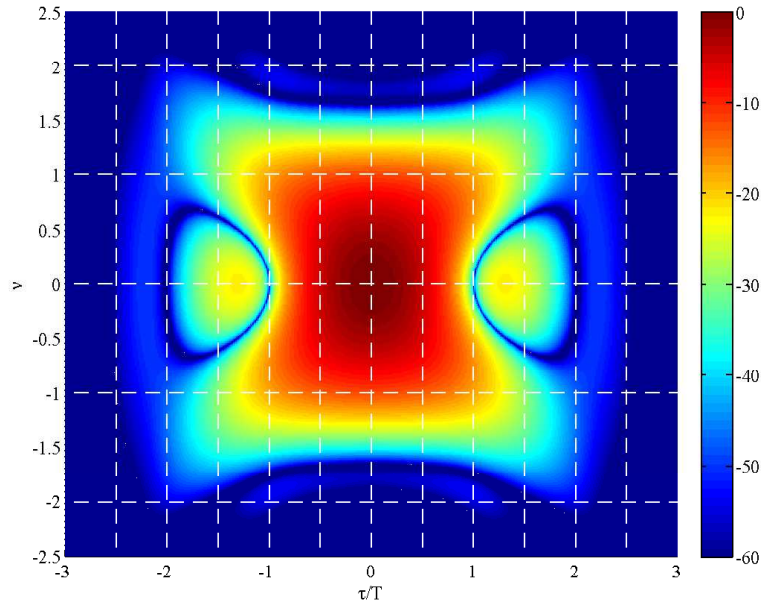


Figure 3.1: Ambiguity function of a FST pulse in dB plotted over the time-frequency lattice. The vertical grid indicates the $T/2$ block spacing and the horizontal grid represents the subchannel grid with spacing of f_{Δ} .

neighboring symbols put limits on the performance of the FD processing, as reported in [77]. The calculation of the amplitude reduction as well as the contribution from the interference $\iota_{k,m}$ from (2.22) in dependence of τ and ν can be achieved with the help of the ambiguity function for a given prototype filter. However, the quantitative evaluation of a specific prototype filter is disregarded in this work in favor of a qualitative result that is suitable for the class of well-localized prototype filters. Even though a large pilot spacing results in less interference, it is not desirable to increase the pilot spacing m_{Δ} beyond two blocks for two reasons. Firstly, for $m_{\Delta} > 2$ the preamble occupies more resources than needed to achieve its functionality. Secondly, with $m_{\Delta} > 2$ the CFO estimation range is reduced as pointed out in the following.

The requirement on the FD algorithms is to achieve an unambiguous CFO estimation in the range of $(-0.5, 0.5)$, as common TD schemes offer. The CFO estimation from (2.29) and the $T/2$ symbol spacing of OQAM-OFDM lead to the following constraint on the maximum symbol spacing m_{Δ}

$$\left| \angle(e^{j\frac{2\pi}{T}\nu m_{\Delta} T/2}) \right| = |\pi\nu m_{\Delta}| < \pi. \quad (3.1)$$

The constraint is fulfilled for a maximum CFO of $|\nu| = 0.5$ only if $m_{\Delta} < 2$. Hence, the pilot spacing should not exceed $m_{\Delta} = 2$ for the CFO estimation range to come close to $|\nu| = 0.5$.

The corresponding argumentation is also valid for the STO estimation from (2.28) and leads to the following constraint on the STO estimation

$$\left| \angle(e^{j\frac{2\pi}{T}k_{\Delta}\tau}) \right| = \left| \frac{2\pi k_{\Delta}\tau}{T} \right| < \pi. \quad (3.2)$$

It results in the maximum subchannel distance to be $k_{\Delta} = 2$ to achieve unambiguous STO estimation in the range of $\{-T/4 + T_s, T/4 - T_s\}$, expressed in multiples of T_s . $k_{\Delta} = 2$ leads to a nearly seamless estimation of the STO taking into account the $T/2$ symbol spacing and block-wise demodulation.

3.1.2 Frequency domain preamble design and frame structure

It follows from the previous considerations that the minimum number of $T/2$ -spaced preamble blocks is set to three. However, the ambiguity function in Figure 3.1 suggests the introduction of one guard block to reduce the interference from payload symbols on the pilot symbols. Even though the preamble

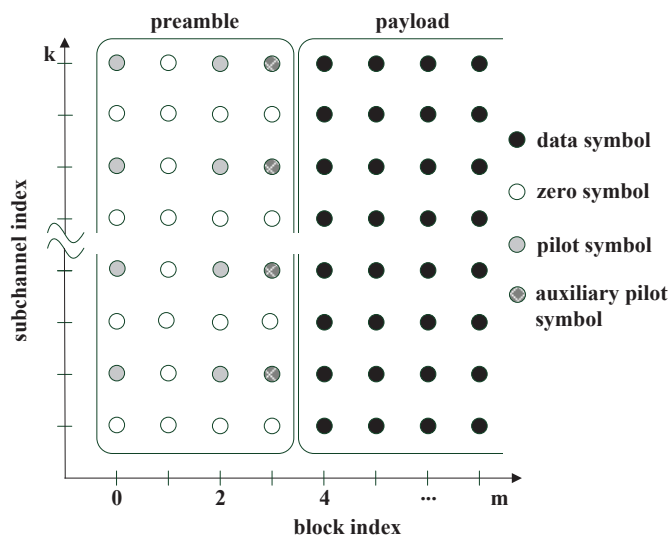


Figure 3.2: Representation of the proposed frame structure.

could be reduced to a subset of the available subchannels \mathbb{K}_u , as it is the case for the preamble design in LTE, this procedure is not suitable for spectrum-adaptive systems. In shared spectrum access the available set \mathbb{K}_u is scenario-dependent and a subset of \mathbb{K} , that is predefined for the preamble, may lead to the undesirable case that no pilot symbol can be allocated. The preamble structure, presented in Figure 3.2, has first been reported in [81]. It provides a trade-off between low self-interference and an appropriate offset estimation range for both STO and CFO. It occupies only every second subchannel and

every second OQAM-OFDM block for separation of the pilots. The pilot spacing in time and frequency direction allows the STO and the normalized CFO to be estimated in the range of $\{-T/4 + T_s, T/4 - T_s\}$ and $(-0.5, 0.5)$, respectively. An example of the structure of a frame using the described preamble is given in Figure 3.2. The same preamble design without auxiliary pilots has been proposed for synchronization in [65] where the preamble and the payload part are completely separated by guard blocks to lower the interference to the preamble part. However, the introduction of guard blocks results in additional overhead and lowers the efficiency. The preamble design as well as the following investigation on frame detectors and estimators can be used in other FBMC systems, e. g., FMT, given that the subchannels are sufficiently separated. Adaption of the FD approach to CP-OFDM, however, seems not feasible because ICI will dramatically increase the self-interference due to the vast overlapping of subchannels.

3.1.3 Auxiliary pilots

The concept of auxiliary pilots has first been reported in [38] to enable the use of pilots for channel estimation in OQAM-OFDM and is evaluated in this work in the context of synchronization. In the proposed preamble design auxiliary pilots can mitigate the distortion of the pilot symbols caused by the succeeding payload symbols. The interference from the payload symbols is obtained prior to transmission with the help of the distortion-free system response of the SFB and AFB. Table 3.1 illustrates an example of a system response which can be derived from the ambiguity function through sampling at the grid points. The pure imaginary interference $\iota_{k,m'}$ defined in (2.22),

$k' \backslash m'$	-2	-1	0	1	2
-1	0.13	-j0.22	-0.24	j0.22	0.13
0	0	0.56	1	0.56	0
1	0.13	j0.22	-0.24	-j0.22	0.13

Table 3.1: Example of a two-dimensional impulse response of the filterbank system.

can be pre-calculated for the distortion-free case, i. e., $\tau = \nu = 0$ and $h_k = 1$, from the data symbols $d_{k,m}$ to be transmitted. Assuming well-localized prototype filters, the interference summation can be restricted to the data symbols in the vicinity of the pilot symbol which is summarized in the set of block indices \mathbb{M}_i and subchannel indices \mathbb{K}_i . Hence, setting $\mathbb{M}_i \in \{-2, -1, 0, 1, 2\}$

and $\mathbb{K}_i \in \{-1, 0, 1\}$ is sufficient when taking into consideration the ambiguity function presented in Figure 3.1. Hence, the calculation of the interference $\iota'_{k,m}(\tau, \nu)$, derived from (2.22), yields

$$\iota'_{k,m}(\tau, \nu) = \sum_{m' \in \mathbb{M}_i} \sum_{\substack{k' \in \mathbb{K}_i \\ (m', k') \neq (m, k)}} \theta_{k', m'} d_{k', m'} \alpha((m - m')T/2, k - k'). \quad (3.3)$$

The sparse design of the preamble reduces the amount of symbols that causes interference to the group of payload symbols. The pilot symbols within the preamble cause no mutual interference due to the perfect reconstruction property of the filterbank for $m' = \{-2, 2\}$, as given in Table 3.1. The values of the auxiliary pilot symbols $d_{k,3}$ can be calculated from (3.3) according to [77]

$$d_{k,3} = \frac{-\Im\{\theta_{k,2}^* \iota'_{k,2}(\tau, \nu)\}}{\alpha(-T/2, 0)}. \quad (3.4)$$

The auxiliary pilots are placed directly next to the pilot symbols at which the interference needs to be canceled. This location results in the smallest amplitude of $d_{k,3}$, as a comparison with the system impulse response in Table 3.1 reveal. Hence, the energy to spend on the auxiliary pilots is minimized and the influence of the auxiliary pilots on the pilot symbols for $\tau \neq 0$ and $\nu \neq 0$ is reduced. The use of auxiliary pilots reduces the amount of guard blocks needed between preamble and payload part to a minimum while limiting the interference from the payload part. The pilots at block index $m = 0$ are considered to be free of interference from the payload symbols and no additional auxiliary pilots are introduced.

3.1.4 Preamble definitions and properties

For the analytical treatment of the preamble design, the payload part and the auxiliary pilots are not taken into account. Hence, the signal model of the preamble leads to the same definition as the one presented in (2.32) and yields

$$b_{k,m} = \begin{cases} \lambda_k, & k \in \mathbb{K}_2 \text{ for } m = \{0, 2\} \\ 0, & \text{otherwise.} \end{cases} \quad (3.5)$$

The subset \mathbb{K}_2 contains either even- or odd-numbered indices out of the set of utilized subchannels \mathbb{K}_u . The pilot sequence $b_{k,m}$ is defined such that the first and the second symbol are identical to simplify the FD algorithm design¹ and to enable the utilization of the preamble for TD synchronization, as

¹ Nevertheless, the FD algorithms derived in this work can be adapted to non-identical sequences as well.

discussed in the next section. As a result of the independence of the individual pilot symbols, the sequence $b_{k,m}$ can be arbitrarily chosen. The sequence can be optimized to achieve peak-to-average power ratio (PAPR) reduction of the TD preamble signal which allows for power boosting of the preamble. Furthermore, the arbitrary sequence design can be used, e. g., for implicit signaling of cell or user identifications to reduce signaling overhead in the network. The pilots in the preamble are boosted by the factor

$$\gamma = 2\sqrt{K/K_u} \quad (3.6)$$

which results in $d_{k,m} = \gamma b_{k,m}$ and $\tilde{b}_{k,m} = \tilde{d}_{k,m}$. The factor $\theta_{k,m}$ is the same for each pilot symbol as follows from the preamble design in which either even or odd indices are set to zero. Hence, without loss of generality the factor $\theta_{k,m}$ is assumed to be 1 and neglected in the signal model in the following.

3.1.5 Time domain preamble

For the TD algorithms, that are introduced as a reference implementation to the FD approach in Chapter 4, a TD preamble signal is assumed that includes two identical parts with $s[nT_s] = s[nT_s + T]$ to enable auto correlation based frame detection and synchronization, as presented in [29, 71]. The signal property can be produced by extending the sparsely-occupied preamble from (3.5) according to

$$b_{k,m}^{\text{TD}} = \begin{cases} \lambda_k, & k \in \mathbb{K}_2 \text{ for } m = \{0, 2, \dots, 2\beta\} \\ 0, & \text{otherwise} \end{cases} \quad (3.7)$$

with the pilot symbols $d_{k,m} = \gamma b_{k,m}^{\text{TD}}$. It results in the desired property

$$s[nT_s] = s[nT_s + T] \text{ for } nT_s \in \{(\beta - 1)T, \dots, \beta T - T_s\}. \quad (3.8)$$

However, the FD preamble, as defined in (3.5), achieves the condition in (3.8) approximately with

$$s[nT_s] \approx s[nT_s + T] \text{ for } nT_s \in \{(\beta - 1)T/2, \dots, (\beta + 1)T/2 - T_s\} \quad (3.9)$$

as a result of the sparse occupancy with pilot symbols in time directions. Hence, in addition to the deployment of the preamble for FD synchronization, it can be used for TD processing as well. Furthermore, the real- or imaginary-valued pilot symbols in the FD result in a conjugate symmetry of the TD signal per block of pilot symbols. This conjugate symmetry can be used for TD synchronization, as reported in [48, 49, 79].

Despite the use for synchronization, the low self-interference between pilots makes the preamble design suitable for channel estimation purposes, as discussed in [46]. The channel estimation performance is analyzed in the sequel to complement the offset estimation study. Hence, the presented preamble can be used for frame detection, synchronization, and channel estimation at the receiver without the need for additional training sequences for short frame length. For that case our work provides a comprehensive study on the receiver design for FD processing based on the discussed preamble. For the case of longer frames or fast varying channel conditions additional pilot symbols, that need to be embedded in the payload part of the frame, should be used for phase and channel tracking.

3.1.6 Signal model of the frequency domain preamble

From the representation of the transmitted and received signals, as defined in (2.20) and (2.21), respectively, the signal model of the preamble is derived. It is used in the following for the analytical derivation of the Cramér-Rao vector bound (CRVB) of the offset estimations. It follows from the prototype filter function and the preamble design that the FD samples $\tilde{b}_{k,m}$ can be considered mutually separated. Hence, each received pilot symbol $\tilde{b}_{k,m}$ can be treated individually and (2.21) yields

$$\begin{aligned} \tilde{b}_{k,0} &= \gamma b_{k,0} h_k e^{-j \frac{2\pi}{T} k \tau} e^{j\phi} \\ &\times \underbrace{\sum_{n=-\infty}^{\infty} p[nT_s - \tau] p[nT_s] e^{j \frac{2\pi}{T} \nu n T_s}}_{a_0 = a(\tau, \nu)} + \Psi_{k,0} \end{aligned} \quad (3.10)$$

for $m = 0$ and

$$\begin{aligned} \tilde{b}_{k,2} &= \gamma b_{k,2} h_k e^{-j \frac{2\pi}{T} k \tau} e^{j\phi} \\ &\times \sum_{n=-\infty}^{\infty} p[nT_s - T - \tau] p[nT_s - T] e^{j \frac{2\pi}{T} \nu n T_s} + \Psi_{k,2} \end{aligned} \quad (3.11)$$

for $m = 2$. $\tilde{b}_{k,2}$ can be rewritten more compactly as

$$\begin{aligned} \tilde{b}_{k,2} &= \gamma b_{k,2} h_k e^{-j \frac{2\pi}{T} k \tau} e^{j\phi} \\ &\times \underbrace{\sum_{n=-\infty}^{\infty} p[nT_s - \tau] p[nT_s] e^{j \frac{2\pi}{T} \nu (nT_s + T)}}_{a_2 = a(\tau + T, \nu) = a_0 e^{j2\pi\nu}} + \Psi_{k,2}. \end{aligned} \quad (3.12)$$

It is derived in Appendix A that the FD noise bins $\Psi_{k,m}$ have the same statistical properties as $\eta[nT_s]$ and, hence, they can be treated as white Gaussian

noise. In the following the parameters τ and ν are neglected for readability in $a_0(\tau, \nu)$ and $a_2(\tau, \nu)$. Furthermore, a_0 and a_2 only differ in phase such that $|a| = |a_0| = |a_2|$ holds. Reformulation of (3.10) and (3.12) in matrix notation yields

$$\tilde{\mathbf{b}} = \gamma e^{j\phi} \mathbf{A} \mathbf{E} \mathbf{H} \mathbf{b} + \boldsymbol{\Psi} \quad (3.13)$$

with

$$\mathbf{A} = \begin{bmatrix} a_0 \mathbf{I} & \mathbf{0} \\ \mathbf{0} & a_2 \mathbf{I} \end{bmatrix} \in \mathbb{C}^{W \times W} \quad (3.14)$$

$$\mathbf{E} = \begin{bmatrix} \text{diag}(e^{-j\frac{2\pi}{T}k\tau}) & \mathbf{0} \\ \mathbf{0} & \text{diag}(e^{-j\frac{2\pi}{T}k\tau}) \end{bmatrix} \in \mathbb{C}^{W \times W} \quad (3.15)$$

$$\mathbf{H} = \begin{bmatrix} \text{diag}(h_k) & \mathbf{0} \\ \mathbf{0} & \text{diag}(h_k) \end{bmatrix} \in \mathbb{C}^{W \times W} \quad (3.16)$$

$$\mathbf{b} = \begin{bmatrix} b_0 \\ b_2 \end{bmatrix} \in \mathbb{C}^{W \times 1} \quad (3.17)$$

and

$$\boldsymbol{\Psi} = \begin{bmatrix} \boldsymbol{\Psi}_0 \\ \boldsymbol{\Psi}_2 \end{bmatrix} \in \mathbb{C}^{W \times 1} \quad (3.18)$$

where $W = 2K_2$ is the number of utilized demodulated preamble symbols, called observations in the following. In this notation each row of a vector or matrix is related to one subchannel, denoted by the index k . In (3.15), this index directly affects the value of the diagonal elements of the matrix \mathbf{E} . Furthermore, the definitions $\mathbf{b}_i = [\dots, b_{k-1,i}, b_{k,i}, b_{k+1,i}, \dots]^T \forall k \in \mathbb{K}_2$ and $\boldsymbol{\Psi}_i = [\dots, \Psi_{k-1,i}, \Psi_{k,i}, \Psi_{k+1,i}, \dots]^T \forall k \in \mathbb{K}_2$ are used in the sequel.

3.1.7 Concluding remarks

In this section we proposed and discussed a preamble design, that is suitable for the FD approach to synchronization, to answer the first question posed in the problem statement.

The preamble design results from a trade-off between estimation range and robustness against interference from neighboring symbols. Hence, it facilitates the utilization of the FD approach to synchronization and leads to an efficient frame structure due to the introduction of auxiliary pilots. Furthermore, a signal model based on the proposed preamble design has been derived for the use in the analytical evaluation of the frame detection and offset estimation, which are presented in the following sections.

3.2 FRAME DETECTION

In this section the metric for frame detection in the FD is introduced and analytically evaluated.

In TD processing the common frame detection metric is based on an auto correlation window that is shifted sample-wise. In FD processing a sample-wise shift of the received signal requires a complete demodulation process per sample shift which would lead to a high computational complexity of the algorithms. Hence, the focus of this work is on block-wise demodulation to efficiently perform detection and estimation in the FD. Frame detection is performed prior to STO and CFO estimation on the stream of received symbols $\tilde{b}_{k,m}$. The decision whether a frame start has been detected or not is discussed for TD synchronization schemes in [71]. The metric is adapted to FD processing according to

$$C_b^A[m] = \left| \frac{2}{W} \sum_{k \in \mathbb{K}_2} \tilde{b}_{k,m} \tilde{b}_{k,m+2}^* \right|. \quad (3.19)$$

Thereby, the superscript $.^A$ indicates that the absolute value is taken. The power normalization of the metric is approximated by

$$Q_b[m] = \frac{1}{W} \sum_{k \in \mathbb{K}_2} (|\tilde{b}_{k,m}|^2 + |\tilde{b}_{k,m+2}|^2) \quad (3.20)$$

$$\approx \frac{2}{W} \sum_{k \in \mathbb{K}_2} |\tilde{b}_{k,m}|^2. \quad (3.21)$$

Based on $C_b^A[m]$ and $Q_b[m]$ the maximum search over the block index \hat{m} according to

$$\hat{m} = \underset{\hat{m}}{\operatorname{argmax}} \left(\frac{C_b^A[\hat{m}]}{Q_b[\hat{m}]} \right) \quad (3.22)$$

delivers an estimate of the frame start. The decision whether a preamble has been acquired or not is performed on the rule

$$C_b^A[\hat{m}] > \rho Q_b[\hat{m}] \quad (3.23)$$

where $0 < \rho < 1$ defines the threshold value. It follows that the detected block index \hat{m} is equal to $m = 0$ if (3.23) is true. The index m is discarded in the following for readability. Two measures are of importance to characterize the quality of the detection algorithm: probability of missed detection $P_{m,d}$ and probability of false alarm $P_{f,a}$. Both probabilities depend on the decision threshold ρ . The first one indicates the probability of a detection failure if a preamble is present but is not detected. The second one provides the probability that a preamble is detected if only noise is received. Further information on the fundamentals of detection theory are given in [45].

3.2.1 Derivation of frame detection probabilities

We now focus on deriving a suitable threshold value to achieve a desired $P_{m,d}$, which depends on the parameters SNR and the number of observations W . The calculation follows the derivation of $P_{m,d}$ and $P_{f,a}$ for the TD signal, as presented in [70]. The conditional probability that C_b^A is below the normalized threshold value ρQ_b is given as

$$P(C_b^A < \rho Q_b) = \int_{-\infty}^{\rho Q_b} f(C_b^A | Q_b) dC_b^A. \quad (3.24)$$

The detailed derivations of the probability density functions (PDF) $f(C_b^A)$ and $f(Q_b)$, and the conditional PDF $f(C_b^A | Q_b)$ are calculated in the following for the AWGN case, i. e., $\mathbf{H} = \mathbf{I}$. For the derivation of the $P_{m,d}$ and $P_{f,a}$, the distribution of the metrics need to be calculated. Using the signal model from (3.13), the correlation metric $C_b[m]$, which is derived from $C_b^A[m]$ in (3.19), yields

$$C_b[m] = \frac{2}{W} \sum_{k \in \mathbb{K}_2} \tilde{b}_{k,m}^* \tilde{b}_{k,m+2}. \quad (3.25)$$

Setting $m = 0$ and discarding the index m for simplicity in $C_b[m]$, the metric C_b can be written in the matrix notation derived from (3.13) as

$$C_b = \frac{2}{W} \tilde{\mathbf{b}}_0^H \tilde{\mathbf{b}}_2 = \frac{2}{W} (\gamma e^{j\phi} \mathbf{a}_0 \mathbf{E} \mathbf{b}_0 + \boldsymbol{\Psi}_0)^H (\gamma e^{j\phi} \mathbf{a}_2 \mathbf{E} \mathbf{b}_2 + \boldsymbol{\Psi}_2). \quad (3.26)$$

Equation (3.26) can be approximated for small values of τ and ν , resulting in $\mathbf{a}_0 \approx \mathbf{a}_2 \approx \mathbf{1}$ and $\mathbf{E} = \mathbf{I}$, according to

$$\begin{aligned} C_b &= \frac{2}{W} (\gamma \mathbf{b}_0 + \boldsymbol{\Psi}_0)^H (\gamma \mathbf{b}_2 + \boldsymbol{\Psi}_2) \\ &= \underbrace{\gamma^2}_{\kappa_1} + \underbrace{\frac{2\gamma}{W} \mathbf{b}_0^H \boldsymbol{\Psi}_2}_{\kappa_2} + \underbrace{\frac{2\gamma}{W} \boldsymbol{\Psi}_0^H \mathbf{b}_2}_{\kappa_3} + \underbrace{\frac{2}{W} \boldsymbol{\Psi}_0^H \boldsymbol{\Psi}_2}_{\kappa_4}. \end{aligned} \quad (3.27)$$

ϕ is set to zero without loss of generality here. For further analysis, C_b is split into its real part C_b^R and its imaginary part C_b^I and their statistical properties are evaluated independently for each summand κ_i , as described in [70]. It follows for κ_1 that $\Re\{\kappa_1\} = \gamma^2$ and $\Im\{\kappa_1\} = 0$. Given that $\boldsymbol{\Psi}$ is circular-symmetric white Gaussian noise, i. e., $\boldsymbol{\Psi}_0^R = \Re\{\boldsymbol{\Psi}_0\} \sim \mathcal{N}(0, \frac{\sigma_{\boldsymbol{\Psi}}^2}{2})$ and $\boldsymbol{\Psi}_0^I = \Im\{\boldsymbol{\Psi}_0\} \sim \mathcal{N}(0, \frac{\sigma_{\boldsymbol{\Psi}}^2}{2})$, κ_2 and κ_3 are i.i.d. normal distributed with the variances and mean values following

$$\Re\{\kappa_2\} \sim \Im\{\kappa_2\} \sim \Re\{\kappa_3\} \sim \Im\{\kappa_3\} \sim \mathcal{N}\left(0, \frac{\sigma_{\boldsymbol{\Psi}}^2 \gamma^2}{W}\right). \quad (3.28)$$

Using the central limit theorem for the evaluation of κ_4 yields

$$\Re\{\kappa_4\} \sim \Im\{\kappa_4\} \sim \mathcal{N}\left(0, \frac{\sigma_\Psi^4}{W}\right). \quad (3.29)$$

Merging these intermediate results ends up in a normally distributed PDF of C_b^R and C_b^I according to

$$f(C_b^R) = \mathcal{N}\left(\gamma^2, \frac{2\sigma_\Psi^2\gamma^2 + \sigma_\Psi^4}{W}\right) \quad (3.30)$$

$$f(C_b^I) = \mathcal{N}\left(0, \frac{2\sigma_\Psi^2\gamma^2 + \sigma_\Psi^4}{W}\right). \quad (3.31)$$

Taking the absolute value of C_b according to $C_b^A = \sqrt{(C_b^R)^2 + (C_b^I)^2}$ results in C_b^A to be Rician-distributed. For large values of W the approximation $f(C_b^A) \approx f(C_b^R)$ can be made due to the dominant influence of $f(C_b^R)$ on the distribution.

From (3.20), by discarding the index m and using the matrix notation, it follows that

$$\begin{aligned} Q_b &= \frac{2}{W}(\gamma\mathbf{b}_0 + \boldsymbol{\Psi}_0)^H(\gamma\mathbf{b}_0 + \boldsymbol{\Psi}_0) \\ &= \underbrace{\gamma^2}_{\vartheta_1} + \underbrace{\frac{4\gamma}{W}\mathbf{b}_0^H\boldsymbol{\Psi}_0^R}_{\vartheta_2} + \underbrace{\frac{2}{W}(\boldsymbol{\Psi}_0^R)^H\boldsymbol{\Psi}_0^R}_{\vartheta_3} + \underbrace{\frac{2}{W}(\boldsymbol{\Psi}_0^I)^H\boldsymbol{\Psi}_0^I}_{\vartheta_4} \end{aligned} \quad (3.32)$$

with $\vartheta_1 = \gamma^2$ and $\vartheta_2 \sim \mathcal{N}(0, \frac{4\gamma^2\sigma_\Psi^2}{W})$. ϑ_3 can be reformulated as

$$\vartheta_3 = \frac{2}{W} \sum_{w=1}^{\frac{W}{2}} |\Psi_w^R|^2 \quad (3.33)$$

and is modeled as a chi-square distribution according to $\vartheta_3 \sim \frac{\sigma_\Psi^2}{W} \chi_{\frac{W}{2}}^2$. The scaled chi-square distribution can be transformed into a gamma distribution, which itself can be approximated by a normal distribution with $\vartheta_3 \sim \mathcal{N}(\frac{\sigma_\Psi^2}{2}, \frac{\sigma_\Psi^4}{W})$ for a large number of W . Using the same argumentation, it follows for ϑ_4 that $\vartheta_4 \sim \mathcal{N}(\frac{\sigma_\Psi^2}{2}, \frac{\sigma_\Psi^4}{W})$. Merging the results under the verified assumption that the covariances of ϑ_i are zero leads to

$$f(Q_b) = \mathcal{N}\left(\gamma^2 + \sigma_\Psi^2, \frac{4\gamma^2\sigma_\Psi^2 + 2\sigma_\Psi^4}{W}\right). \quad (3.34)$$

The conditional PDF $f(C_b^A|Q_b)$ can be calculated with the help of [44]. Its mean μ and variance σ^2 are given by

$$\mu_{C_b^R|Q_b} = \mu_{C_b^R} + \frac{\sigma_{C_b^R, Q_b}^2}{\sigma_{Q_b}^2}(Q_b - \mu_{Q_b}) \quad (3.35)$$

$$\sigma_{C_b^R|Q_b}^2 = \sigma_{C_b^R}^2 - \frac{\left(\sigma_{C_b^R, Q_b}^2\right)^2}{\sigma_{Q_b}^2} \quad (3.36)$$

with the covariance

$$\sigma_{C_b^R, Q_b}^2 = E[C_b^R Q_b] - \mu_{C_b^R} \mu_{Q_b}. \quad (3.37)$$

After some calculations and with

$$E[C_b^R Q_b] = \gamma^4 + \gamma^2 \sigma_\Psi^2 + \frac{2\gamma^2 \sigma_\Psi^2}{W} \quad (3.38)$$

the covariance is given by $\sigma_{C_b^R, Q_b}^2 = \frac{2\gamma^2 \sigma_\Psi^2}{W}$. Now (3.35) and (3.36) can be expressed as

$$\mu_{C_b^R|Q_b} = \frac{\gamma^2}{2\gamma^2 + \sigma_\Psi^2} (Q_b + \gamma^2) \quad (3.39)$$

$$\sigma_{C_b^R|Q_b}^2 = \frac{\sigma_\Psi^2}{W(2\gamma^2 + \sigma_\Psi^2)} (2\gamma^4 + 4\gamma^2 \sigma_\Psi^2 + \sigma_\Psi^4) \quad (3.40)$$

and $f(C_b^A|Q_b) = \mathcal{N}(\mu_{C_b^R|Q_b}, \sigma_{C_b^R|Q_b}^2)$ can be calculated depending on W and the ratio $\frac{\gamma^2}{\sigma_\Psi^2}$. The ratio $\frac{\gamma^2}{\sigma_\Psi^2}$ corresponds to an SNR per subchannel in the FD. Integration over Q_b provides the P_{md} equal to

$$P_{md} = \int_0^\infty f(Q_b) \int_{-\infty}^{\rho Q_b} f(C_b^A|Q_b) dC_b^A dQ_b. \quad (3.41)$$

The P_{fa} can be derived for the case that only noise is present and $\tilde{b}_{k,m} = \Psi_{k,m}$ holds. Then, the metric $C_\Psi[m]$ is defined similar to (3.19) as

$$C_\Psi[m] = \frac{2}{W} \sum_{k \in \mathbb{K}_2} \Psi_{k,m} \Psi_{k,m+2}^* \quad (3.42)$$

and from (3.20) $Q_\Psi[m]$ yields

$$Q_\Psi[m] \approx \frac{2}{W} \sum_{k \in \mathbb{K}_2} |\Psi_{k,m}|^2. \quad (3.43)$$

A false alarm occurs when the threshold is exceeded, which can be formulated as follows

$$(C_\Psi[m])^2 > \rho^2 (Q_\Psi[m])^2. \quad (3.44)$$

Here, $(C_\Psi[m])^2 = |C_\Psi[m]|^2$ has been chosen following the derivation in [70], which allows to simplify the calculation of the PDF. The derivation of the PDFs is given in the sequel, where the index m is omitted for readability. Concerning the derivation of P_{fa} , adapting (3.30) and (3.31) to match (3.42) directly results in the following distributions for the real and imaginary parts

$$\Re\{C_\Psi\} \sim \Im\{C_\Psi\} \sim \mathcal{N}\left(0, \frac{\sigma_\Psi^4}{W}\right). \quad (3.45)$$

Modifying the decision rule to utilize the squared absolute value of C_Ψ results in C_Ψ^2 to be chi-square distributed with two degree of freedoms according to $C_\Psi^2 \sim \frac{\sigma_\Psi^4}{W} \chi_2^2$. The relation between the chi-square and the gamma distribution further leads to

$$f(C_\Psi^2) = \Gamma\left(1, \frac{2\sigma_\Psi^4}{W}\right). \quad (3.46)$$

From (3.34) it follows analogously for Q_Ψ that

$$f(Q_\Psi) = \mathcal{N}\left(\sigma_\Psi^2, \frac{2\sigma_\Psi^4}{W}\right). \quad (3.47)$$

$f(C_\Psi^2)$ and $f(Q_\Psi)$ can be used to calculate the P_{fa} . If independence of Q_Ψ and C_Ψ^2 is assumed, the P_{fa} is given by

$$P_{fa} = \int_0^\infty f(Q_\Psi) \int_{\rho^2 Q_\Psi^2}^\infty f(C_\Psi^2) dC_\Psi^2 dQ_\Psi. \quad (3.48)$$

It has been shown in [70] for the TD metric that σ_Ψ^2 is only a scaling factor for $f(C_\Psi^2)$ and $f(Q_\Psi)$, resulting in P_{fa} to be independent of the noise power. For the analytical derivation of the P_{fa} for the case that payload symbols plus noise are present the detection metric is performed on the demodulated symbols $\tilde{b}_{k,m}$. However, compared to the case with pure noise the received symbols in the FD are no longer normally distributed but depend on a discrete modulation alphabet. A tractable analytical solution can be obtained only if we approximate the distributions with normal distributions, resulting in expressions for $f(Q_\Psi)$ and $f(C_\Psi^2)$ that are equivalent to the case of pure noise. Hence, this P_{fa} case is only evaluated based on simulations.

The analytical description of the probabilities and their derivation turns out to be equivalent to the TD solutions derived in [70] as a consequence of the assumptions about the signal that can be made for the time and the frequency domain signals in equal measure.

3.2.2 Evaluation

The previously derived analytical expressions for P_{md} and P_{fa} are compared against the simulation-based results in Figure 3.3. For the comparison, a worst-case scenario with $\gamma^2/\sigma_\Psi^2 = 2$ is chosen, which corresponds to an SNR of 0 dB. The analytical derivation of P_{md} over the threshold value ρ is based on the assumption that the STO and CFO are small.

To take the influence of the offsets into account, two scenarios are considered in the simulations. Firstly, the P_{md} for the ideal case with no offset is evaluated, presented as the lower solid curve in Figure 3.3. Secondly, the offset-afflicted P_{md} is plotted, represented by the upper solid curve. The curve of

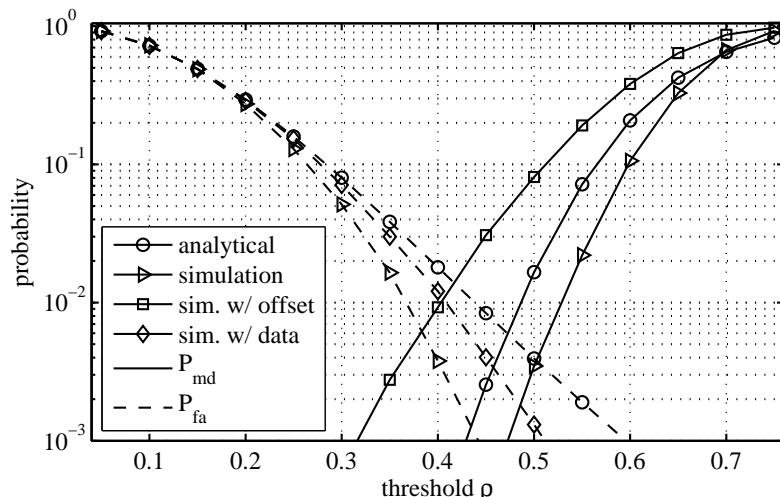


Figure 3.3: Theoretically derived $P_{m,d}$ and $P_{f,a}$ and simulation results for $W = 64$ and $\gamma^2/\sigma_\Psi^2 = 2$.

the analytically derived performance lies in between these two. The analytical and zero-offset results well agree with the results for the corresponding TD metric presented in [70]. Furthermore, it shows that in the presence of STO and CFO, the detection rate degrades due to the amplitude degradation of the received preamble symbols and the introduction of interference.

The analytically derived $P_{f,a}$, which assumes the presence of pure noise, is given by the upper dashed curve in Figure 3.3. It provides a pessimistic performance prediction compared to the outcome of the simulations, given by the two lower dashed curves. The difference stems from the approximations made during the derivation of $P_{f,a}$. For the simulation results, two different scenarios are differentiated here. The lower dashed curve states the detection performance in the presence of pure noise, whereas the dashed line in the middle specifies the case that offset-afflicted payload symbols are received. For frame detection in TD, these two cases are considered equal, because the TD multicarrier signal is assumed to be distributed according to a normal distribution, yielding similar characteristics as the noise [70]. For the FD approach, however, this assumption is no longer valid, as it is indicated by the simulation results. This may be related to the fact that the detection metric is performed on the demodulated received symbols; the assumption that the statistics of the symbols affecting the detection follow a normal distribution seems to be a too optimistic here. From Figure 3.3 the choice $\rho = 0.4$ leads to a trade-off between $P_{f,a}$ and $P_{m,d}$ that minimizes both metrics at an SNR of 0 dB and in case of offsets. Because the frame detection is the first stage in the synchronization process, STOs and CFOs are likely to be present. The corresponding evaluation of the $P_{m,d}$ versus SNR is presented in Figure 3.4

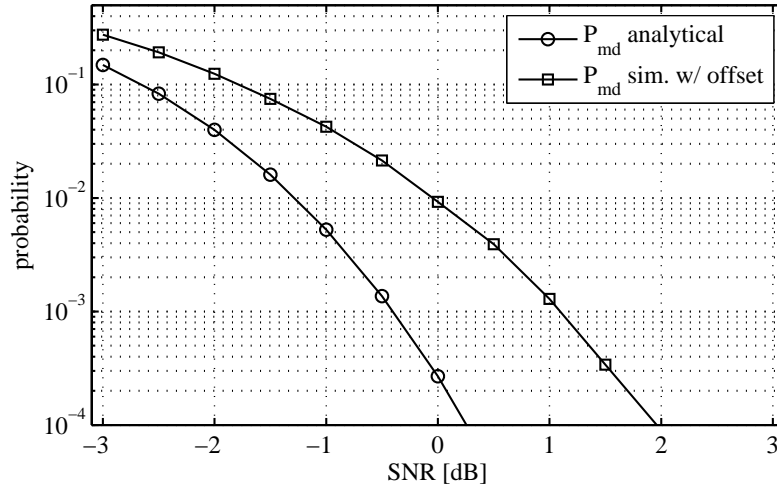


Figure 3.4: P_{md} versus SNR for a threshold of $\rho = 0.4$.

for a threshold of $\rho = 0.4$. It follows that a P_{md} below 10^{-4} can be reached for an SNR level above 2 dB while taking offsets into consideration.

3.2.3 Concluding remarks

In this section we showed that the analytical evaluation of the probabilities of false alarm and missed detection for the frame detection in the FD can be treated in a similar way as its TD counterpart, presented in [70]. However, the influence of offsets on the FD frame detection needs to be evaluated by simulations and leads to a degradation of the performance in comparison to the TD solutions. Furthermore, we derived a suitable threshold value to achieve a defined P_{md} from the derived analytical framework.

The outcome of this section answers the question how frame detection performs in the FD, which has been posed in the problem statement. The results of this section will be used for initial frame synchronization in the measurement study described in Chapter 4.

3.3 FREQUENCY OFFSET AND SYMBOL TIMING ESTIMATION

In this section the ML estimator (MLE) for the CFO is presented and the MLE for the STO is derived. Due to the limited estimation range of this symbol timing estimator, two alternative STO estimators are motivated and described. In addition, the CRVB is obtained as a lower bound on the variance of the estimators.

3.3.1 CFO estimation

After frame acquisition the block index \hat{m} , that characterizes the start of the preamble sequence, is known. Hence, \hat{m} is set to zero to simplify the notation in the following. Based on the estimation of the first preamble symbol, a coarse estimation of the CFO, which still suffers from ICI and ISI, can be obtained in closed form according to

$$\hat{\nu} = \frac{1}{2\pi} \angle \left(\sum_{k \in \mathbb{K}_2} \tilde{b}_{k,2} \tilde{b}_{k,0}^* \right). \quad (3.49)$$

The corresponding metric applied to two identical signal parts in the TD yields the MLE for the CFO. It has been derived in [53] and is also used in [65]. For small offsets, when the influence of interference and amplitude degradation can be neglected, the metric for the FD yields the MLE and achieves the CRVB, as shown in the evaluation section. In case of larger offsets the estimator is not only influenced by noise but also by interference from neighboring subchannels and the misalignment of the transmit and receive filters. Hence, due to the simplicity and the optimality in case of small offsets the MLE from [53] is considered a useful and practical solution for FD estimation and is further evaluated for FD processing in this work.

3.3.2 STO estimation - MLE

The ML STO estimator is derived from the signal model in (3.13), as described in the following. The logarithm of the likelihood function $l(\tilde{\mathbf{b}}|\mathbf{v})$, neglecting irrelevant additive factors, is given by

$$\begin{aligned} \ln(l(\tilde{\mathbf{b}}|\mathbf{v})) &= -(\tilde{\mathbf{b}} - \gamma e^{j\phi} \mathbf{A} \mathbf{E} \mathbf{H} \mathbf{b})^H \mathbf{C}_{\Psi}^{-1} (\tilde{\mathbf{b}} - \gamma e^{j\phi} \mathbf{A} \mathbf{E} \mathbf{H} \mathbf{b}) \\ &= \frac{-T_s}{\sigma_{\Psi}^2} (\tilde{\mathbf{b}} - \gamma e^{j\phi} \mathbf{A} \mathbf{E} \mathbf{H} \mathbf{b})^H (\tilde{\mathbf{b}} - \gamma e^{j\phi} \mathbf{A} \mathbf{E} \mathbf{H} \mathbf{b}) \end{aligned} \quad (3.50)$$

with the parameter vector $\mathbf{v} = [\tau, \nu, \phi]^T$. As a result of the preamble design the covariance matrix

$$\mathbf{C}_{\Psi} = \frac{\sigma_{\Psi}^2}{T_s} \mathbf{I} \quad (3.51)$$

is derived as a subset of $\mathbf{C}_{\Psi}^{K \times K}$ where only the subchannels with indices $k \in \mathbb{K}_2$ are considered. The matrix $\mathbf{C}_{\Psi}^{K \times K}$ is defined in Appendix A. Setting the derivation of (3.50) with respect to τ equal to zero results in the ML condition for the STO estimator.

From (2.9) it follows that each received preamble symbol $\tilde{\mathbf{b}}_i$ contains independent information about the parameter τ and can be evaluated individually. Hence, for one received preamble block $\tilde{\mathbf{b}}_i$ the MLE condition in case of AWGN, i. e., $\mathbf{H} = \mathbf{I}$, yields

$$\begin{aligned}
 \frac{\partial \ln(l(\tilde{\mathbf{b}}_i|\mathbf{v}))}{\partial \tau} &= \frac{\partial}{\partial \tau} \left(\frac{-T_s}{\sigma_\Psi^2} (\tilde{\mathbf{b}}_i - \gamma e^{j\phi} \mathbf{a}_i \mathbf{E}_i \mathbf{b}_i)^H (\tilde{\mathbf{b}}_i - \gamma e^{j\phi} \mathbf{a}_i \mathbf{E}_i \mathbf{b}_i) \right) \\
 &= \frac{\partial}{\partial \tau} \left(\frac{-T_s}{\sigma_\Psi^2} \sum_{k \in \mathbb{K}_2} |\tilde{b}_{k,i} - \gamma e^{j\phi} a_i e^{-j\frac{2\pi}{T} k \tau} b_{k,i}|^2 \right) \quad (3.52) \\
 &= \frac{\partial}{\partial \tau} \left(\frac{-T_s}{\sigma_\Psi^2} \sum_{k \in \mathbb{K}_2} (|\tilde{b}_{k,i}|^2 + |\gamma a_i b_{k,i}|^2 \right. \\
 &\quad \left. - \tilde{b}_{k,i} \gamma e^{-j\phi} a_i^* e^{j\frac{2\pi}{T} k \tau} b_{k,i}^* + \tilde{b}_{k,i}^* \gamma e^{j\phi} a_i e^{-j\frac{2\pi}{T} k \tau} b_{k,i}) \right) \\
 &= \sum_{k \in \mathbb{K}_2} k \left(\tilde{b}_{k,i} e^{-j\phi} e^{j\frac{2\pi}{T} k \tau} b_{k,i}^* - \tilde{b}_{k,i}^* e^{j\phi} e^{-j\frac{2\pi}{T} k \tau} b_{k,i} \right) \\
 &= 0
 \end{aligned}$$

with $\mathbf{E}_i \in \mathbb{C}^{\frac{W}{2} \times \frac{W}{2}}$ equal to the upper left or lower right submatrix of \mathbf{E} , depending on the index i . The last step of calculation is valid under the assumption of small time and frequency offsets, i. e., $a_i = 1$. From (3.52) the term

$$\sum_{k \in \mathbb{K}_2} k |\tilde{b}_{k,i}| \sin(\angle \tilde{b}_{k,i} - \angle b_{k,i} - \phi - \frac{2\pi}{T} k \tau) = 0 \quad (3.53)$$

can be extracted. For $\phi \approx 0$ the simplification $\sin(x) \approx x$ can be applied which results in the following closed-form expression for the STO estimation

$$\begin{aligned}
 \hat{\tau}_{\text{MLE},i} &= \frac{T}{2\pi} \frac{\sum_{k \in \mathbb{K}_2} k |\tilde{b}_{k,i}| (\angle \tilde{b}_{k,i} - \angle b_{k,i} - \phi)}{\sum_{k \in \mathbb{K}_2} k^2 |\tilde{b}_{k,i}|} \quad (3.54) \\
 &= \frac{T}{2\pi} \left(\frac{\sum_{k \in \mathbb{K}_2} k |\tilde{b}_{k,i}| (\angle \tilde{b}_{k,i} - \angle b_{k,i})}{\sum_{k \in \mathbb{K}_2} k^2 |\tilde{b}_{k,i}|} - \frac{\phi \sum_{k \in \mathbb{K}_2} k |\tilde{b}_{k,i}|}{\sum_{k \in \mathbb{K}_2} k^2 |\tilde{b}_{k,i}|} \right).
 \end{aligned}$$

Under the assumption that $|\tilde{b}_{k,i}|$ is approximately constant and for a symmetric allocation of the subchannels, the sum $\sum_{k \in \mathbb{K}_2} k |\tilde{b}_{k,i}|$ is zero and the MLE becomes independent of the common phase shift ϕ . However, the allocation of subchannels is scenario-dependent and symmetry is not necessarily provided. Hence, the MLE is in general influenced by the common phase.

Merging the estimates for both preamble blocks yields the final MLE

$$\hat{\tau}_{\text{MLE}} = \frac{1}{2} \sum_{i \in \{0,2\}} \hat{\tau}_{\text{MLE},i}. \quad (3.55)$$

For \mathbb{K}_2 being a sufficiently large set or at sufficiently high SNR the MLE is unbiased [44]. The estimation of the MLE is limited by the phase ambiguity of the subchannel with the highest subchannel index k . Setting the maximum subchannel index $|k_{\max}| = K/2 - 1$ into (2.9) yields the phase of $e^{-j\frac{2\pi}{T}(\frac{K}{2}-1)\tau}$ to be smaller than π only for $|\tau| \leq T_s$. Furthermore, the assumption that $\phi \approx 0$ is not always justified and, hence, the MLE is not considered a practical option for STO estimation.

3.3.3 STO estimation - CFE

The limitation of the estimation range can be overcome by a suboptimal solution in which the difference in phase between two neighboring pilots of the same symbol at different subchannels are used. In the following this method is called closed-form estimator (CFE) and has been proposed for embedded pilot symbols in [77]. Hence, the closed-form expression for the estimation of τ is motivated by (2.28) and formulated as

$$\hat{\tau}_{\text{CFE}} = \frac{T}{2\pi\Delta_k} \angle \left(\sum_{i \in \{0,2\}} \sum_{k \in \mathbb{K}_p} \frac{\tilde{b}_{k,i} \tilde{b}_{k+\Delta_k,i}^*}{b_{k,i} b_{k+\Delta_k,i}^*} \right). \quad (3.56)$$

The set of available subchannel indices for estimation is \mathbb{K}_p . \mathbb{K}_p is a subset of \mathbb{K}_2 that only contains those indices k which fulfill the condition that the index $k + \Delta_k$ is as well an element of \mathbb{K}_2 . Additionally, it follows from the preamble design that $\Delta_k = 2$ is the difference in subchannel indices of the pilots.

The estimate $\hat{\tau}_{\text{CFE}}$ yields the STO τ based on the mean delay $\bar{\tau}_h$ of the channel. Furthermore, for the estimation to hold it is assumed that the coherence bandwidth B_c is sufficiently large such that the pilots at indices k and $k + \Delta_k$ experience approximately the same phase of the channel [77]. For the approximation of a maximum delay spread τ_{RMS} at which the condition is fulfilled we take the definition of the coherence bandwidth $B_c \gtrsim \frac{1}{2\pi\tau_{\text{RMS}}}$ from [52]. It follows that the pilot spacing Δ_k needs to fulfill $\Delta_k \leq \frac{T}{2\pi\tau_{\text{RMS}}} \lesssim TB_c$. A fixed pilot spacing of $\Delta_k = 2$, resulting from the preamble design, leads to the approximation of the maximum normalized delay spread that is tolerable according to $\frac{\tau_{\text{RMS}}}{T} \leq \frac{1}{2\pi\Delta_k} = 0.079$.

Furthermore, with $\Delta_k = 2$ the unambiguous STO estimation range expressed in integer multiples of T_s is $\{-T/4 + T_s, T/4 - T_s\}$. Hence, the CFE offers a more practical solution compared to the MLE approach. A solution for the condition $E[\hat{\tau}_{\text{CFE}}] = \tau$, which shows that the CFE is unbiased, cannot

be found in a simple way. For that reason, we focus on the noise-free case with $h_k = 1$ only. Insertion of $\tilde{b}_{k,i} = \gamma e^{j\phi} a_i e^{-j\frac{2\pi}{T}k\tau} b_{k,i}$ in (3.56) yields

$$\begin{aligned} \hat{\tau}_{\text{CFE}} &= \frac{T}{2\pi\Delta_k} \angle \left(\sum_{i \in \{0,2\}} \sum_{k \in \mathbb{K}_p} \frac{\tilde{b}_{k,i} \tilde{b}_{k+\Delta_k,i}^*}{b_{k,i} b_{k+\Delta_k,i}} \right) \\ &= \frac{T}{2\pi\Delta_k} \angle \left(\gamma^2 |a_i|^2 \sum_{i \in \{0,2\}} \sum_{k \in \mathbb{K}_p} e^{j\frac{2\pi}{T}\Delta_k\tau} \right) \\ &= \frac{T}{2\pi\Delta_k} \angle \left(\gamma^2 |a_i|^2 2K_p e^{j\frac{2\pi}{T}\Delta_k\tau} \right) = \tau, \end{aligned} \tag{3.57}$$

which illustrates that the estimate $\hat{\tau}_{\text{CFE}}$ is unbiased.

3.3.4 STO estimation - CCE

Different to this closed-form expression of the STO, the cross correlation based estimator (CCE) is based on finding the τ that maximizes the absolute value of the cross correlation $\sum_{k \in \mathbb{K}_2} \tilde{b}_{k,i} b_{k,i}^* e^{j\frac{2\pi}{T}k\tau}$. The cross correlation approach to FD synchronization has first been proposed in [81]. By maximizing the expression the ML condition in (3.52) is minimized. It results in the metric

$$\hat{\tau}_{\text{CCE}} = \underset{-T/4+T_s \leq \hat{\tau} \leq T/4-T_s}{\operatorname{argmax}} \left(\left| \sum_{i \in \{0,2\}} \sum_{k \in \mathbb{K}_2} (\tilde{b}_{k,i} e^{-j\pi\hat{\tau}i}) (b_{k,i} e^{-j\frac{2\pi}{T}k\hat{\tau}})^* \right| \right). \tag{3.58}$$

The estimate of the CFO $\hat{\nu}$, obtained in (3.49), is used to counteract the distortion effect of the CFO on the cross correlation. In contrast to the estimate $\hat{\tau}_{\text{CFE}}$, the CCE estimates τ based on the strongest path of the channel impulse response, which leads to a difference in the estimation of the frame start position between the CFE and the CCE. In the following the evaluation of the estimators is based on the mean delay rather than on the delay of the strongest path or the time instance of the first path. The decision for the mean delay as the reference time is motivated by the fact that the energy of the preamble is spread over the different channel paths. However, the center of its energy, the first-order moment of the normalized path energy of the channel impulse response, is located at the mean delay $\bar{\tau}_h$, as defined in the beginning of this chapter. Hence, the evaluation of the estimation error will be biased for the CCE in multipath scenarios by the difference between the time instance of the strongest path and the mean delay. Furthermore, the estimation is affected by rounding effects due to the choice of the trial values for τ to be integer multiples of T_s . The use of integer multiples of the sample duration T_s makes

the CCE different from the closed-form estimations, where $\hat{\tau}$ can result in real decimal numbers. However, it is beneficial to choose a limited set of trial values in the range of $\{-T/4 + T_s, T/4 - T_s\}$ for reasons of complexity² and to achieve an unambiguous estimation. Under the assumption that $\hat{\nu} = \nu$, it is calculated in the following that $\hat{\tau}_{\text{CCE}}$ matches τ for the noise-free case. By discarding irrelevant scaling factors and phase shifts for simplicity it follows from (3.58) that

$$\begin{aligned} & \underset{-T/4+T_s \leq \tilde{\tau} \leq T/4-T_s}{\operatorname{argmax}} \left(\left| \sum_{i \in \{0,2\}} \sum_{k \in \mathbb{K}_2} e^{-j \frac{2\pi}{T} k \tau} e^{j \frac{2\pi}{T} k \tilde{\tau}} b_{k,i} b_{k,i}^* \right| \right) \\ &= \underset{-T/4+T_s \leq \tilde{\tau} \leq T/4-T_s}{\operatorname{argmax}} \left(\left| \sum_{i \in \{0,2\}} \sum_{k \in \mathbb{K}_2} e^{-j \frac{2\pi}{T} k (\tilde{\tau} - \tau)} \right| \right). \end{aligned} \quad (3.59)$$

The expression in (3.59) is maximized if $\tilde{\tau} = \tau$, which indicates that the estimator is unbiased at high SNR.

3.3.5 Cramér-Rao vector bound - frequency domain

The CRVB for CFO and STO estimation is derived to obtain lower bounds on the estimation performance of the discussed estimators. The CRVB depends on the parameter vector $\mathbf{v} = [\tau, \nu, \phi]^T$ [44]. Even though the common phase shift ϕ is not estimated it is taken into account for CRVB calculation to analyze the dependence of τ and ν on ϕ . ϕ is usually estimated by the channel estimation in combination with the channel coefficients and equalized accordingly in a practical system.

The derivation of the regularity condition, as a pre-condition to the CRVB, is presented in Appendix B. With the log-likelihood function from (3.50), the entries of the Fisher information matrix \mathbf{F} are calculated according to

$$\mathbf{F}_{(i,j)} = -\mathbb{E} \left[\frac{\partial^2 \ln(l(\tilde{\mathbf{b}}|\mathbf{v}))}{\partial v_i \partial v_j} \right] \quad \forall i, j \in \{1, 2, 3\} \quad (3.60)$$

where for $\mathbf{F}_{(i,i)}$ the following identity is given in [44] as

$$-\mathbb{E} \left[\frac{\partial^2 \ln(l(\tilde{\mathbf{b}}|\mathbf{v}))}{\partial v_i \partial v_i} \right] = \mathbb{E} \left[\left(\frac{\partial \ln(l(\tilde{\mathbf{b}}|\mathbf{v}))}{\partial v_i} \right)^2 \right]. \quad (3.61)$$

² Even though only integer multiples of T_s are used in this work, trial values on the base of fractions of the sample duration T_s can be applied as well. However, the number of calculations increases with the number of trial values.

The matrix entry $F_{(1,1)}$, which is related to the estimation of τ , yields

$$\begin{aligned} F_{(1,1)} &= \mathbb{E} \left[\left(\frac{\partial}{\partial \tau} \left(\frac{-\Gamma_s}{\sigma_\Psi^2} (\tilde{\mathbf{b}} - \gamma e^{j\phi} \mathbf{A} \mathbf{E} \mathbf{H} \mathbf{b}) \right)^{\text{H}} (\tilde{\mathbf{b}} - \gamma e^{j\phi} \mathbf{A} \mathbf{E} \mathbf{H} \mathbf{b}) \right) \right]^2 \\ &= \frac{\Gamma_s^2}{\sigma_\Psi^4} \mathbb{E} \left[\left(-\gamma e^{-j\phi} \mathbf{b}^{\text{H}} \mathbf{H}^{\text{H}} \frac{\partial \mathbf{E}^{\text{H}} \mathbf{A}^{\text{H}}}{\partial \tau} \boldsymbol{\Psi} - \gamma e^{j\phi} \boldsymbol{\Psi}^{\text{H}} \mathbf{H} \frac{\partial \mathbf{E} \mathbf{A}}{\partial \tau} \mathbf{b} \right)^2 \right] \end{aligned} \quad (3.62)$$

which is simplified by replacing $\tilde{\mathbf{b}} - \gamma e^{j\phi} \mathbf{A} \mathbf{E} \mathbf{H} \mathbf{b}$ with $\boldsymbol{\Psi}$. Further assessment of the expression leads to

$$\begin{aligned} F_{(1,1)} &= \frac{\Gamma_s^2}{\sigma_\Psi^4} \mathbb{E} \left[\left(\gamma e^{-j\phi} \mathbf{b}^{\text{H}} \mathbf{H}^{\text{H}} \frac{\partial \mathbf{E}^{\text{H}} \mathbf{A}^{\text{H}}}{\partial \tau} \boldsymbol{\Psi} \right)^2 \left(\gamma e^{j\phi} \boldsymbol{\Psi}^{\text{H}} \mathbf{H} \frac{\partial \mathbf{E} \mathbf{A}}{\partial \tau} \mathbf{b} \right)^2 \right. \\ &\quad \left. + 2 \left(\gamma e^{-j\phi} \mathbf{b}^{\text{H}} \mathbf{H}^{\text{H}} \frac{\partial \mathbf{E}^{\text{H}} \mathbf{A}^{\text{H}}}{\partial \tau} \boldsymbol{\Psi} \right) \left(\gamma e^{j\phi} \boldsymbol{\Psi}^{\text{H}} \mathbf{H} \frac{\partial \mathbf{E} \mathbf{A}}{\partial \tau} \mathbf{b} \right) \right]. \end{aligned} \quad (3.63)$$

When taking the expectation only the last summand results in a non-zero contribution because $\mathbb{E}[(\Psi_{k,m})^2] = 0$ and $\mathbb{E}[\Psi_{k,m}^* \Psi_{k,m}] = \sigma_\Psi^2$ hold. Furthermore, due to the Rayleigh fading property of the channel, i. e., $\mathbb{E}[\mathbf{H}^{\text{H}} \mathbf{H}] = \mathbf{I}$, it follows that

$$\begin{aligned} F_{(1,1)} &= \frac{2\gamma^2 \Gamma_s^2}{\sigma_\Psi^2} \left(\mathbf{b}^{\text{H}} \frac{\partial \mathbf{E}^{\text{H}} \mathbf{A}^{\text{H}}}{\partial \tau} \frac{\partial \mathbf{E} \mathbf{A}}{\partial \tau} \mathbf{b} \right) \\ &= \frac{2\gamma^2 \Gamma_s^2}{\sigma_\Psi^2} \left(\mathbf{b}^{\text{H}} \left(\frac{\partial \mathbf{E}^{\text{H}}}{\partial \tau} \mathbf{A}^{\text{H}} + \mathbf{E}^{\text{H}} \frac{\partial \mathbf{A}^{\text{H}}}{\partial \tau} \right) \left(\frac{\partial \mathbf{A}}{\partial \tau} \mathbf{E} + \mathbf{A} \frac{\partial \mathbf{E}}{\partial \tau} \right) \mathbf{b} \right). \end{aligned} \quad (3.64)$$

Replacing $\frac{\partial \mathbf{E}}{\partial \tau}$ with $\text{diag} \left(\frac{-j2\pi k}{T} \right) \mathbf{E}$ and with $\mathbf{E}^{\text{H}} \mathbf{E} = \mathbf{I}$, (3.64) leads to

$$\begin{aligned} F_{(1,1)} &= \frac{2\gamma^2 \Gamma_s^2}{\sigma_\Psi^2} \left(\mathbf{b}^{\text{H}} \left(\text{diag} \left(\frac{4\pi^2 k^2}{T^2} \right) \mathbf{A}^{\text{H}} \mathbf{A} \right. \right. \\ &\quad \left. \left. + \text{diag} \left(\frac{j2\pi k}{T} \right) \mathbf{A}^{\text{H}} \frac{\partial \mathbf{A}}{\partial \tau} + \text{diag} \left(-\frac{j2\pi k}{T} \right) \frac{\partial \mathbf{A}^{\text{H}}}{\partial \tau} \mathbf{A} \right. \right. \\ &\quad \left. \left. + \frac{\partial \mathbf{A}^{\text{H}}}{\partial \tau} \frac{\partial \mathbf{A}}{\partial \tau} \right) \mathbf{b} \right). \end{aligned} \quad (3.65)$$

The upper and the lower half of the matrices can be treated separately, because the corresponding symbols \mathbf{b}_0 and \mathbf{b}_2 are considered mutually inde-

pendent. When discarding the matrix notation and making use of the correspondence $\mathbf{b}_i^H \text{diag} \left(\frac{-j2\pi k}{T} \right) \mathbf{b}_i = \frac{-j2\pi}{T} \sum_{k \in \mathbb{K}_u} k$, (3.65) results in

$$\begin{aligned} \mathbf{F}_{(1,1)} &= \frac{2\gamma^2 T_s^2}{\sigma_\Psi^2} \left(\frac{4\pi^2}{T^2} (|a_0^2| + |a_2^2|) \sum_{k \in \mathbb{K}_u} k^2 \right. \\ &\quad \left. + \frac{j2\pi}{T} \left(a_0^* \frac{\partial a_0}{\partial \tau} - a_0 \frac{\partial a_0^*}{\partial \tau} + a_2^* \frac{\partial a_2}{\partial \tau} - a_2 \frac{\partial a_2^*}{\partial \tau} \right) \sum_{k \in \mathbb{K}_u} k \right. \\ &\quad \left. + \left(\frac{\partial a_0^*}{\partial \tau} \frac{\partial a_0}{\partial \tau} + \frac{\partial a_2^*}{\partial \tau} \frac{\partial a_2}{\partial \tau} \right) W \right) \end{aligned} \quad (3.66)$$

where W is the number of observations per block. W is equal to the elements used in the set of subchannels \mathbb{K}_2 .

Replacing $\frac{\partial}{\partial \tau}$ with $\frac{\partial}{\partial v}$ in (3.64) and further calculation yields

$$\begin{aligned} \mathbf{F}_{(2,2)} &= \frac{2\gamma^2 T_s^2}{\sigma_\Psi^2} \left(\mathbf{b}^H \left(\frac{\partial \mathbf{A}^H}{\partial v} \frac{\partial \mathbf{A}}{\partial v} \right) \mathbf{b} \right) \\ &= \frac{2\gamma^2 T_s^2 W}{\sigma_\Psi^2} \left(\frac{\partial a_0^*}{\partial v} \frac{\partial a_0}{\partial v} + \frac{\partial a_2^*}{\partial v} \frac{\partial a_2}{\partial v} \right). \end{aligned} \quad (3.67)$$

For the derivation of $\mathbf{F}_{(3,3)}$ the replacement of $\frac{\partial}{\partial \tau}$ with $\frac{\partial}{\partial \phi}$ in (3.62) leads to

$$\begin{aligned} \mathbf{F}_{(3,3)} &= \frac{-\gamma^2 T_s^2}{\sigma_\Psi^4} \mathbb{E} \left[\left(e^{-j\phi} \mathbf{b}^H \mathbf{H}^H \mathbf{E}^H \mathbf{A}^H \Psi - e^{j\phi} \Psi^H \mathbf{E} \mathbf{A} \mathbf{H} \mathbf{b} \right)^2 \right] \\ &= \frac{2\gamma^2 T_s^2}{\sigma_\Psi^4} \mathbb{E} \left[\left(\mathbf{b}^H \mathbf{H}^H \mathbf{E}^H \mathbf{A}^H \Psi \right) \left(\Psi^H \mathbf{E} \mathbf{A} \mathbf{H} \mathbf{b} \right) \right]. \end{aligned} \quad (3.68)$$

Using the same argumentation regarding Ψ as for the calculation of (3.64), it follows that

$$\mathbf{F}_{(3,3)} = \frac{2\gamma^2 T_s^2}{\sigma_\Psi^2} \left(\mathbf{b}^H \left(\mathbf{A}^H \mathbf{E}^H \mathbf{E} \mathbf{A} \right) \mathbf{b} \right) = \frac{2\gamma^2 T_s^2 W}{\sigma_\Psi^2} (|a_0|^2 + |a_2|^2). \quad (3.69)$$

The off-diagonals of \mathbf{F} are derived in (3.70), (3.71), and (3.72) in the following. Due to the symmetry of second derivatives it follows for the off-diagonals that $\mathbf{F}_{(i,j)} = \mathbf{F}_{(j,i)}$. The calculation of $\mathbf{F}_{(1,2)}$ yields

$$\begin{aligned} \mathbf{F}_{(1,2)} &= \frac{T_s}{\sigma_\Psi^2} \mathbb{E} \left[\frac{\partial}{\partial \tau} \frac{\partial}{\partial v} \left(\Psi^H \Psi \right) \right] \\ &= \frac{-T_s}{\sigma_\Psi^2} \mathbb{E} \left[\frac{\partial}{\partial \tau} \left(\gamma e^{-j\phi} \mathbf{b}^H \mathbf{H}^H \mathbf{E}^H \frac{\partial \mathbf{A}^H}{\partial v} \Psi + \gamma e^{j\phi} \Psi^H \frac{\partial \mathbf{A}}{\partial v} \mathbf{E} \mathbf{H} \mathbf{b} \right) \right] \\ &= \frac{\gamma^2 T_s}{\sigma_\Psi^2} \left(\mathbf{b}^H \mathbf{E}^H \frac{\partial \mathbf{A}^H}{\partial v} \frac{\partial \mathbf{A} \mathbf{E}}{\partial \tau} \mathbf{b} + \mathbf{b}^H \frac{\partial \mathbf{A}^H \mathbf{E}^H}{\partial \tau} \frac{\partial \mathbf{A}}{\partial v} \mathbf{E} \mathbf{b} \right) \\ &= \frac{\gamma^2 T_s}{\sigma_\Psi^2} \left(W \left(\frac{\partial a_0^*}{\partial v} \frac{\partial a_0}{\partial \tau} + \frac{\partial a_2^*}{\partial v} \frac{\partial a_2}{\partial \tau} \right) \right. \\ &\quad \left. + \frac{j2\pi}{T} \sum_{k \in \mathbb{K}_u} k \left(\frac{\partial a_0^*}{\partial v} a_0 + \frac{\partial a_2^*}{\partial v} a_2 - a_0^* \frac{\partial a_0}{\partial v} - a_2^* \frac{\partial a_2}{\partial v} \right) \right). \end{aligned} \quad (3.70)$$

$\mathbf{F}_{(1,3)}$ and $\mathbf{F}_{(2,3)}$ are derived in analogy and result in

$$\mathbf{F}_{(1,3)} = - \left(W \left(a_0^* \frac{\partial a_0}{\partial \tau} + a_2^* \frac{\partial a_2}{\partial \tau} - \frac{\partial a_0^*}{\partial \tau} a_0 - \frac{\partial a_2^*}{\partial \tau} a_2 \right) + \frac{j4\pi}{T} \sum_{k \in \mathbb{K}_u} k (|a_0|^2 + |a_2|^2) \right) \frac{j\gamma^2 T_s}{\sigma_\Psi^2} \quad (3.71)$$

and

$$\mathbf{F}_{(2,3)} = \frac{-j\gamma^2 T_s W}{\sigma_\Psi^2} \left(a_0^* \frac{\partial a_0}{\partial \nu} + a_2^* \frac{\partial a_2}{\partial \nu} - \frac{\partial a_0^*}{\partial \nu} a_0 - \frac{\partial a_2^*}{\partial \nu} a_2 \right). \quad (3.72)$$

The ambiguity functions a_0 and a_2 are determined by the prototype filter $p[nT_s]$ and the offsets τ and ν . Hence, their partial derivatives, and therefore \mathbf{F} , have to be evaluated for different prototype filters individually. Depending on the prototype filter, the derivation of a closed-form expression for the CRVB is difficult to obtain. For that reason, we have opted to use a numerical approach here. The CRVB is then given by the numerical matrix inversion of \mathbf{F} according to

$$\text{CRVB}(\mathbf{v}_i) = \mathbf{F}_{(i,i)}^{-1}. \quad (3.73)$$

The Fisher information matrix is independent of the channel matrix \mathbf{H} that is included in the signal model from (3.13). Hence, the CRVB on the variance of the estimation is valid for both AWGN and Rayleigh fading channels.

For the case of unbiased estimators the CRVB is related to the root mean square error (RMSE) according to $\text{RMSE} = \sqrt{\text{CRVB}}$ [44], which is used as a measure of the deviation of an estimation in the following. A representation of the derived RMSE over the offset plane is given in Figure 3.5a for the STO and in Figure 3.5b for the CFO estimation. The results in Figure 3.5 illustrate the increase of the variance of the estimates with increasing offsets. The mismatch of the SFB and AFB and the resulting amplitude degradation leads to a loss in information about the parameter to be estimated, however, the noise variance is not affected by the mismatch. Hence, the increase of the variance occurs from an effective decrease of the SNR per subchannel. Furthermore, it is apparent from \mathbf{F} that the common phase shift ϕ has no effect on the CRVB of τ and ν .

3.3.6 Cramér-Rao vector bound - time domain

After derivation of the FD CRVB, the question posed in Section 2.4 whether the lower bound on the variance of the estimation differs between time and frequency domain, demands for a comparable expression of the CRVB for the

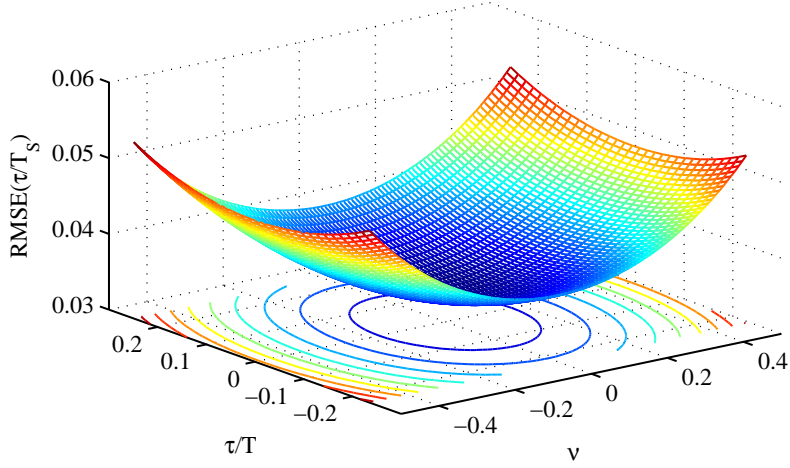
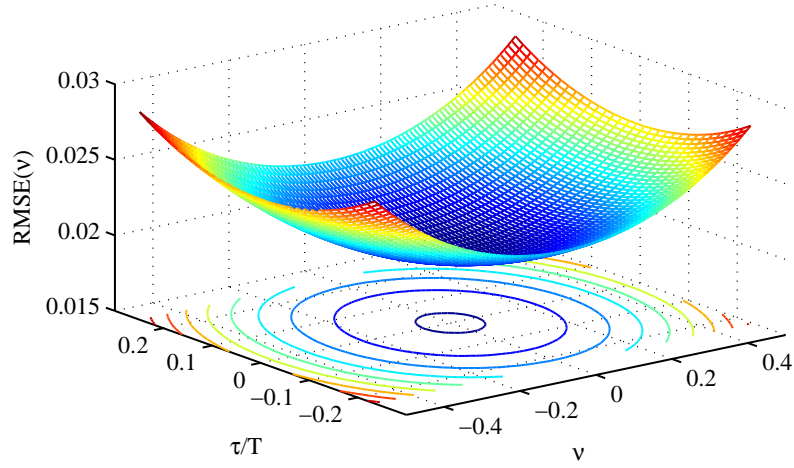

 (a) RMSE derived from the CRVB for the normalized STO τ/T_s .

 (b) RMSE derived from the CRVB for the normalized CFO v .

 Figure 3.5: CRVB in dependence of the offsets τ and v at an SNR of 0 dB. The influence of the CFO on the CRVB can be observed.

TD. In [29] the CRVB^{TD}, based on the preamble described in (3.7), is defined as

$$\text{CRVB}^{\text{TD}}(\tau) = \frac{(KT_s)^2}{8\pi^2 W^{\text{TD}} \text{SNR}} \frac{1}{\left[\frac{1}{K_u} \sum_{k \in K_u} \left(k - \frac{1}{K_u} \sum_{k \in K_u} k \right)^2 \right]} \quad (3.74)$$

and

$$\text{CRVB}^{\text{TD}}(v) = \frac{3}{2(\pi T_s)^2 (W^{\text{TD}})^3 \text{SNR}}. \quad (3.75)$$

The CRVB^{TD} reveals no dependence on the offset parameter τ and v due to the TD processing. Hence, no filterbank mismatch is present. For that reason, the offsets are set to zero for the calculation of the FD CRVB, if not otherwise stated. In addition, for the comparison of the CRVB with the CRVB^{TD} both

have to be normalized with respect to the SNR. Taking into consideration that OQAM-OFDM blocks are shifted half a symbol period $T/2$ the resulting SNR yields

$$\text{SNR} = \frac{\Theta_{\text{sample}}}{\Theta_{\text{noise}}} = \frac{2}{\sigma_n^2} \tag{3.76}$$

where Θ_{sample} is the power per sample and Θ_{noise} represents the noise power. For the boosted pilots of the FD preamble, the ratio of the power of the frequency bin Θ_{bin} and Θ_{noise} per utilized subchannel, given that $\sigma_n^2 = \sigma_\Psi^2$, is

$$\frac{\Theta_{\text{bin}}}{\Theta_{\text{noise}}} = \frac{|\gamma|^2}{\sigma_\Psi^2} = \frac{4K}{K_u \sigma_\Psi^2} = \frac{2K}{K_u} \text{SNR}. \tag{3.77}$$

The equality of σ_n^2 and σ_Ψ^2 is derived in Appendix A. The processing gain of the FD approach can be intuitively explained: By processing only the subchannels bearing a pilot, half the noise power present at unoccupied subchannels is abandoned and not used in the metric. However, in the TD metric no equivalent noise filtering takes place. The second parameter, which is important for the evaluation of the CRVB and comparison between the time and frequency domain method, is the number of observations. While the TD estimate is based on $W^{\text{TD}} = 2K$ samples, we utilize only $W = K_u$ observations for the FD method. The relation between these two yields

$$\frac{W}{W^{\text{TD}}} = \frac{K_u}{2K} \leq \frac{1}{2}. \tag{3.78}$$

Hence, the sparse preamble exhibits a loss of at least factor of two in number of observations W . However, the evaluation shows that for $K_u = K$ the gains and losses compensate each other approximately.

The performance of the STO and CFO estimators is discussed by means of the RMSE obtained by simulation in the following sections.

3.3.7 Evaluation of STO estimation

In Figure 3.6 the CRVB and CRVB^{TD} for the STO estimation are plotted in addition to the RMSE of the discussed estimators in AWGN and Rayleigh fading channels. The MLE for the STO, as defined in (3.55), achieves the CRVB at an SNR of 27 dB and with the limited range of offsets of $\{-T_s, T_s\}$. Hence, the results verify that the MLE is unbiased and asymptotically optimal [44]. However, at lower SNR the MLE performance degrades with respect to the CRVB due to an increasing influence of the noise on the metric, as discussed in [64]. The MLE under Rayleigh fading conditions is not considered as, in general, the assumption that $\phi \approx 0$ is not justified. The CFE approaches the

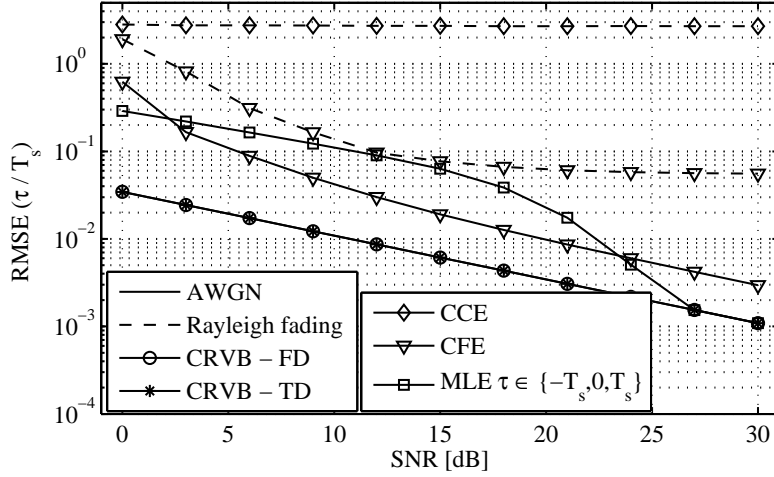


Figure 3.6: RMSE of the STO estimation versus SNR.

CRVB but shows to be suboptimal since a gap between the RMSE of the estimation and the theoretical bound persists even for high SNR values in case of AWGN. The gap can be explained by the fact that the CFE metric from (3.56) does not take into consideration the subchannel index k as it is the case for the MLE metric in (3.54). Hence, the CFE metric does not deploy the complete received information.

Furthermore, the CFE performance is shown for the case of arbitrary offset values. In contrast, the CRVB is calculated with no offset present and shows the best-case scenario for the estimation, as a comparison with Figure 3.5a reveals. The robustness of the CFE against interference, shown by the lack of an error floor for high SNR, is discussed in Appendix C. However, the performance of the CFE is significantly lowered by the Rayleigh fading. The degradation stems from the spread of received power over multiple channel taps and the corresponding effect of different paths on the received pilot symbols, which finally result in an error floor for high SNR. In case of AWGN and for the given number of realizations the CCE, based on the trial values $\tilde{\tau}$ as multiple of T_s , produces no error. It complies with the observation that the CRVB is well below the rounding threshold of 0.5. Hence, the discrete set of trial values lead to no errors. For the case of Rayleigh fading, the high RMSE of the CCE stems from the fact that the CCE estimates the timing based on the strongest path, which deviates from the mean delay taken as timing reference in this work.

Since Figure 3.5 indicates that the CFO has the most dominant effect on the estimation performance, the influence of the CFO on the RMSE of the STO estimation is evaluated. The results are presented in Figure 3.7, where the RMSE is plotted versus fixed values of ν while τ is spanning the complete

range of offsets. The $CRVB^{TD}$ is a single value for the given SNR as it is not a function of the offsets. However, the CRVB depends on the offsets and is averaged over τ at fixed values of ν for the evaluation. The CRVB slightly increases with increasing absolute value of ν due to the loss in received energy. The CFE shows a corresponding behavior for the same reason, whereas no dependence of the performance of the CCE on the CFO can be observed in both AWGN and Rayleigh fading.

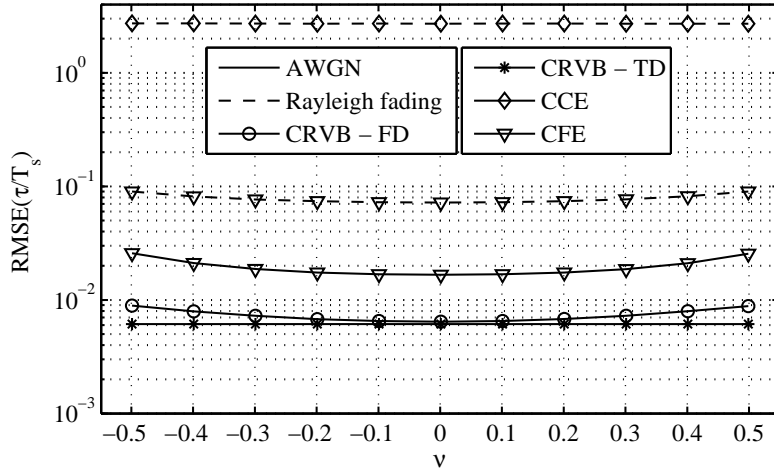


Figure 3.7: RMSE of the STO estimation versus CFO at an SNR of 15 dB. The CRVB is averaged over the STOs.

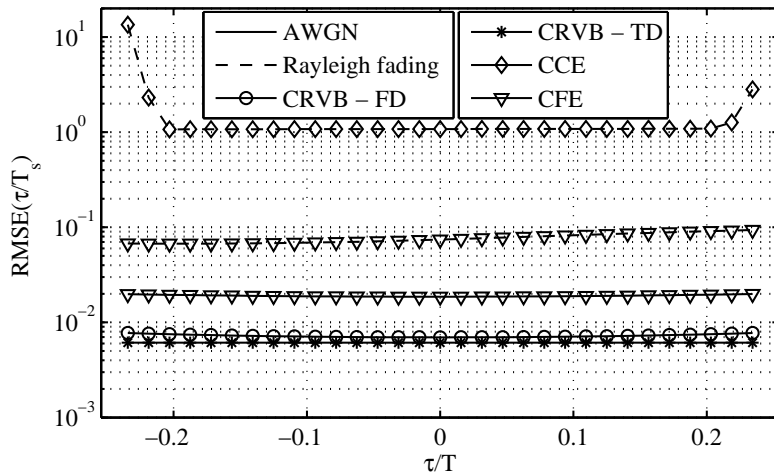


Figure 3.8: RMSE of the STO estimation versus STO at an SNR of 15 dB. The CRVB is averaged over the CFOs.

In Figure 3.8 the corresponding results for fixed τ show only an insignificant dependence of the CRVB and the error of the CFE on the STO in AWGN channels. However, the Rayleigh fading channel affects the course of the RMSE for the CFE and CCE as a result of the delay spread of the channel

impulse response. For the CFE the RMSE increases slightly with increasing values of τ , whereas for the CCE the channel degrades the estimation at the edge of the block, i. e., at STO values $|\tau|$ that are close to $T/4$.

3.3.8 Effect of subchannel distribution on STO estimation

From the closed-form expressions of the CRVB^{TD} in (3.74) and (3.75) it follows that only the STO estimation performance is influenced by the distribution of the pilots according to \mathbb{K}_u within the available spectrum. Hence, the focus is on the STO estimation for the case of different subchannel allocations and the CFO estimation is omitted. The CRVB^{TD} from (3.74) is scaled by the function $f(\mathbb{K}_u)$, defined as

$$f(\mathbb{K}_u) = \left(\frac{1}{K_u} \sum_{k \in \mathbb{K}_u} \left(k - \frac{1}{K_u} \sum_{k \in \mathbb{K}_u} k \right)^2 \right)^{-1} \tag{3.79}$$

for fixed values of K_u, W , and the SNR.

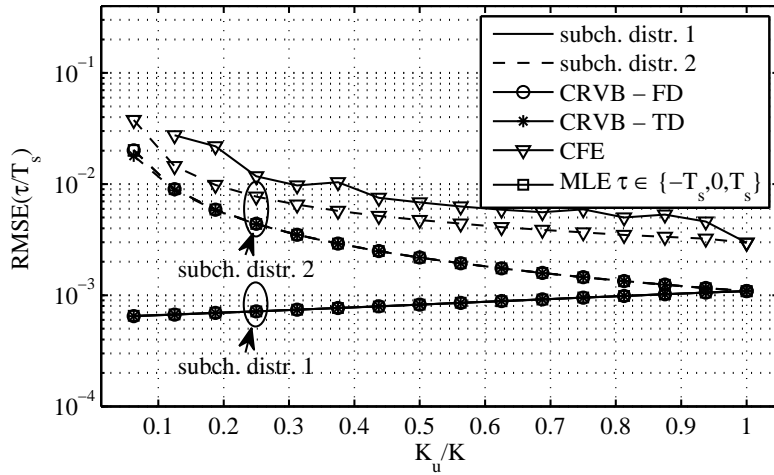


Figure 3.9: RMSE of different STO estimators versus spectrum allocation for $K = 64$ and an SNR of 30 dB. The MLE achieves the CRVB for all allocations.

The minimum value of the CRVB^{TD} can be achieved by dividing the subchannel indices in two groups which are maximally separated. Such a best-case distribution can be achieved for $K = 64, K_u = 8$, and $\mathbb{K}_u = \{-31, -30, -29, -28, 29, 30, 31, 32\}$, denoted as subchannel distribution 1 in Figure 3.9. Grouping all available pilot indices in one block, e. g., with $K = 64, K_u = 8$, and $\mathbb{K}_u = \{-3, -2, -1, 0, 1, 2, 3, 4\}$, maximizes $f(\mathbb{K}_u)$ and leads to a worst-case distribution, labeled subchannel distribution 2.

It can be observed from the results in Figure 3.9 that differences in the achievable variance of the estimation can vary up to one order of magnitude. The dependency of the CRVB for the STO estimation on the allocation can be explained by the difference in occupied overall bandwidth, as pointed out in [64]. Hence, a constant offset is irrelevant as equation (3.79) reveals. The CFE disregards this information by the pairwise evaluation of the received pilots and only depends on the number of pilot pairs in \mathbb{K}_p . The MLE, however, utilizes this information and its RMSE overlap with both the lower bound for time and frequency domain. In a practical scenario, the distribution is subject to the available spectrum allocation and as a consequence the estimation performance is considered to be somewhere in between the two discussed cases.

3.3.9 Evaluation of CFO estimation

Following the discussion of the STO estimation, the evaluation of the CFO estimation is provided in Figure 3.10.

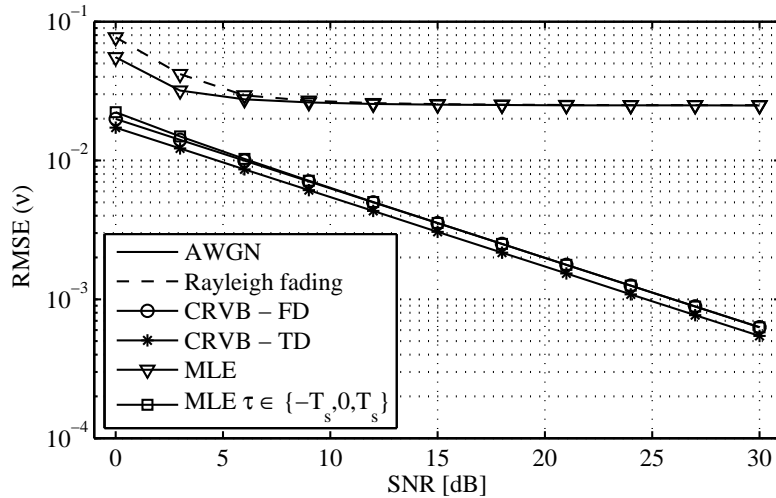


Figure 3.10: RMSE of the normalized CFO estimation versus SNR.

The CRVB estimation for FD processing shows a slightly higher bound compared to CRVB^{TD} , which results from the different approximations that are used during the derivation of CRVB^{TD} . For verification of the derived CRVB, the MLE of the CFO is simulated with zero frequency offset and a small timing offset range of $\{-T_s, T_s\}$. For that case, the curve for MLE in Figure 3.10 matches the derived CRVB which suggests that the derivation of CRVB^{TD} for CFO estimation is too optimistic.

Nevertheless, in simulations with offsets that span the complete offset range the MLE achieves a variance of its estimation error that approaches the CRVB only for low SNR for both AWGN and Rayleigh fading channels. For higher values of the SNR the RMSE results in an error floor. Comparison of the performance curves from Figure 3.11 with the CRVB, shown in Figure 3.5b, leads to the conclusion that the error floor is produced by the remaining intrinsic interference from ICI between pilot symbols in the presence of frequency offsets. The error floor is discussed and calculated in the Appendix C. Even though the CRVB degrades only slightly with increasing CFO, the difference between the CRVB and the MLE is one order of magnitude higher for the absolute value of the CFO close to 0.5 compared to the case of zero CFO. The difference results from the intrinsic interference, which is not taken into account for the calculation of the CRVB. For the case that the absolute value of

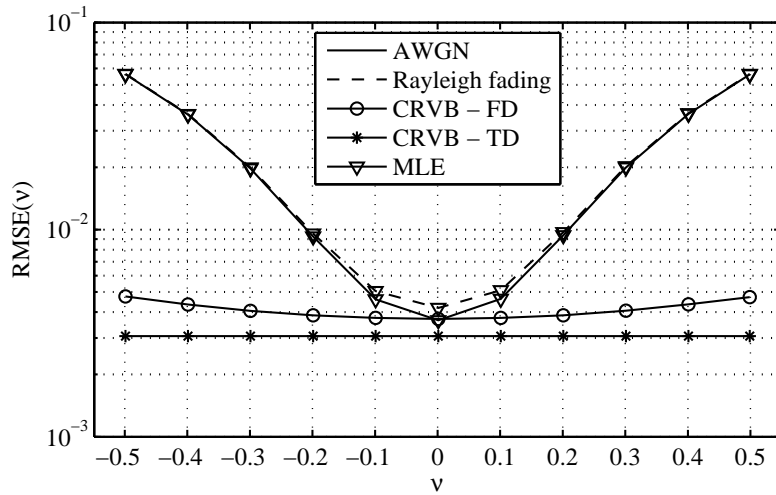


Figure 3.11: RMSE of the CFO estimation versus CFO at an SNR of 15 dB.

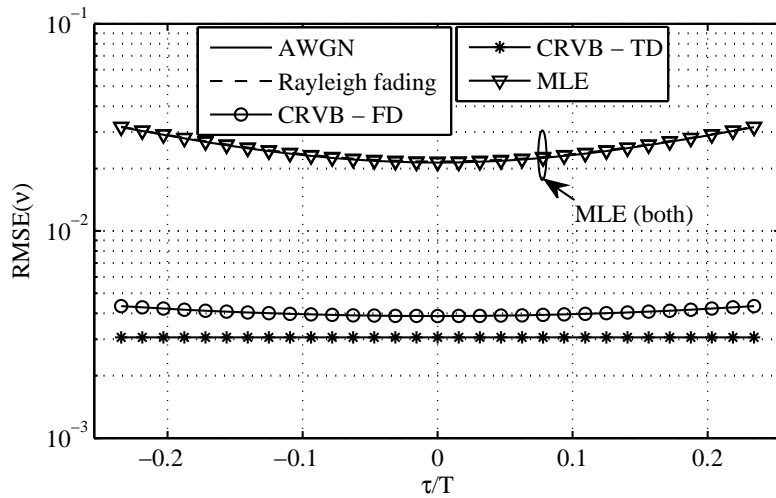


Figure 3.12: RMSE of the CFO estimation versus STO at an SNR of 15 dB.

CFO is below 0.1, the MLE almost achieves the CRVB. Hence, for that case it is concluded that the resulting interference is sufficiently small such that an estimate close to the optimum can be achieved.

In contrast to the strong dependence between the RMSE and the CFO, the STO has no significant effect on the CFO estimation, as can be observed by the RMSE plotted versus STO in Figure 3.12. The CFO estimation itself is performed on each subchannel and is not affected by the STO-induced phase-shift described in (2.9), which is constant between symbols over time. The dominant effect of the RMSE is the distortion by the CFO over which is averaged to obtain the results shown in Figure 3.12.

3.3.10 Concluding remarks

In this section we answered the question posed in the problem statement concerning the difference in theoretical performance between the FD and TD approach, proposed practical estimators, and evaluated their performance. We conclude that the FD approach achieves the same theoretical performance as its TD counterpart and is only slightly degraded by the mismatch of the filterbanks. Furthermore, we showed that the FD CFO estimator is primarily degraded by the CFO-induced interference. The STO estimators, however, showed to be robust against the effects of offsets and no error floor can be observed. Hence, for an applicable system concept the effect of the CFO on the estimation has to be reduced to achieve a satisfying estimation of the CFO.

3.4 CHANNEL ESTIMATION

In this section the possibility to estimate the channel coefficients is analyzed based on the preamble design from (3.5) in addition to the offset estimation reported in the previous section. The focus of this work is on synchronization, however, the channel estimation is influenced by residual synchronization errors. Furthermore, the equalization can reduce the effects of a non-perfect offset estimation, e. g., STO-induced phase shift, to minimize the BER and FER and improve the system performance. Hence, the effects of residual synchronization errors on the channel estimation performance are analyzed to evaluate their influence on the channel estimation in the following. In addition, the degradation of the channel estimation in relation to the delay spread of the channel is simulated to show the limits of channel estimation with the proposed preamble design in the presence of multipath propagation. The channel estimation is processed in the FD in multicarrier systems due to its

simplicity. It complements the approach to shift the signal processing entirely in the FD for reasons of flexibility and interference rejection. Sparse preambles have already been used for channel estimation in [43, 46] in the context of OQAM-OFDM.

The preamble design, presented in Section 3.1, offers two OQAM-OFDM blocks for estimation. For the task of channel estimation one block is sufficient. However, by utilizing two blocks a processing gain is achieved. Hence, in the following the channel estimation is averaged over the two available pilots per subchannel according to

$$\hat{h}_k = \frac{1}{2} \sum_{l \in \{0,2\}} \frac{\tilde{b}_{k,\hat{m}+l}}{b_{k,l}}. \quad (3.80)$$

(3.80) is a commonly known metric for CP-OFDM, discussed for example in [52] and deployed in pilot-based channel estimation, e. g., in LTE.

3.4.1 Signal model for channel estimation

Even though this single-tap estimation is commonly used in CP-OFDM, where ISI is removed by the cyclic prefix, this metric can also be used in OQAM-OFDM. However, as will be shown in the following evaluation, this single-tap channel estimation is degraded by ISI if the channel has a large delay spread. However, the influence from ISI is not considered in the following derivation.

For the derivation of the lower bound of the variance of the channel estimation, the signal model from (3.13) is extended and the common phase term $e^{j\phi}$ is included in the complex-valued channel coefficient matrix \mathbf{H} . From (3.13) the new signal model is defined as

$$\tilde{\mathbf{b}} = \gamma \mathbf{H} \mathbf{A} \mathbf{E} \mathbf{b} + \Psi \quad (3.81)$$

which can be reduced to

$$\tilde{\mathbf{b}}_k = \gamma h_k \mathbf{A}_k \mathbf{E}_k \mathbf{b}_k + \Psi_k \quad (3.82)$$

for the evaluation of the channel estimation performance. This reduction to one subchannel is possible as a result of the independence of the estimation of each channel coefficient h_k from its neighboring coefficients. Hence, each subchannel can be treated individually and it is sufficient to analyze only one

subchannel. The corresponding matrices for the signal model in (3.82) are defined as

$$\tilde{\mathbf{b}}_k = \begin{bmatrix} \tilde{b}_{k,0} \\ \tilde{b}_{k,2} \end{bmatrix} \quad (3.83)$$

$$\mathbf{A}_k = \begin{bmatrix} a_0 & 0 \\ 0 & a_2 \end{bmatrix} \quad (3.84)$$

$$\mathbf{E}_k = \begin{bmatrix} e^{j\frac{2\pi}{T}k\tau} & 0 \\ 0 & e^{j\frac{2\pi}{T}k\tau} \end{bmatrix} \quad (3.85)$$

$$\mathbf{b}_k = \begin{bmatrix} b_{k,0} \\ b_{k,2} \end{bmatrix} \quad (3.86)$$

and

$$\Psi_k = \begin{bmatrix} \Psi_{k,0} \\ \Psi_{k,2} \end{bmatrix}. \quad (3.87)$$

Thereby, the matrix \mathbf{A}_k is independent of the subchannel index k .

3.4.2 Cramér-Rao vector bound - channel estimation

Based on the signal model (3.82), the log-likelihood function results in

$$\begin{aligned} \ln(l(\tilde{\mathbf{b}}_k|\mathbf{w})) &= -(\tilde{\mathbf{b}}_k - \gamma h_k \mathbf{A}_k \mathbf{E}_k \mathbf{b}_k)^H \mathbf{C}_{\Psi}^{-1} (\tilde{\mathbf{b}}_k - \gamma h_k \mathbf{A}_k \mathbf{E}_k \mathbf{b}_k) \quad (3.88) \\ &= \frac{-T_s}{\sigma_{\Psi}^2} (\tilde{\mathbf{b}}_k - \gamma h_k \mathbf{A}_k \mathbf{E}_k \mathbf{b}_k)^H (\tilde{\mathbf{b}}_k - \gamma h_k \mathbf{A}_k \mathbf{E}_k \mathbf{b}_k) \end{aligned}$$

with $\mathbf{w} = [h_k^R, h_k^I]$. In the following, the complex channel coefficient is split into its real and imaginary part according to $h_k = h_k^R + jh_k^I$. Hence, the log-likelihood function yields

$$\begin{aligned} \ln(l(\tilde{\mathbf{b}}_k|\mathbf{w})) &= \frac{-T_s}{\sigma_{\Psi}^2} \left(\tilde{\mathbf{b}}_k^H \tilde{\mathbf{b}}_k - \tilde{\mathbf{b}}_k^H \gamma (h_k^R + jh_k^I) \mathbf{A}_k \mathbf{E}_k \mathbf{b}_k \quad (3.89) \right. \\ &\quad - \mathbf{b}_k^H \mathbf{E}_k^H \mathbf{A}_k^H \gamma (h_k^R - jh_k^I) \tilde{\mathbf{b}}_k \\ &\quad \left. + \mathbf{b}_k^H \mathbf{E}_k^H \mathbf{A}_k^H \mathbf{A}_k \mathbf{E}_k \mathbf{b}_k \gamma^2 ((h_k^R)^2 + (h_k^I)^2) \right). \end{aligned}$$

With $\mathbf{b}_k^H \mathbf{E}_k^H \mathbf{A}_k^H \mathbf{A}_k \mathbf{E}_k \mathbf{b}_k = |a_0|^2 + |a_2|^2 = 2|a|^2$, (3.89) leads to

$$\begin{aligned} \ln(l(\tilde{\mathbf{b}}_k|\mathbf{w})) &= \frac{-T_s}{\sigma_{\Psi}^2} \left(\tilde{\mathbf{b}}_k^H \tilde{\mathbf{b}}_k - \tilde{\mathbf{b}}_k^H \gamma (h_k^R + jh_k^I) \mathbf{A}_k \mathbf{E}_k \mathbf{b}_k \quad (3.90) \right. \\ &\quad \left. - \mathbf{b}_k^H \mathbf{E}_k^H \mathbf{A}_k^H \gamma (h_k^R - jh_k^I) \tilde{\mathbf{b}}_k + 2|a|^2 \gamma^2 ((h_k^R)^2 + (h_k^I)^2) \right). \end{aligned}$$

As a precondition to the derivation of the CRVB, the fulfillment of the regulatory condition is verified in Appendix B. Due to the common assumption of a Rayleigh fading channel, where the real and imaginary part of the channel coefficient are i.i.d., the Fisher information matrix $\mathbf{F}^H \in \mathbb{R}^{2 \times 2}$ is a diagonal matrix with $\mathbf{F}_{(1,1)}^H = \mathbf{F}_{(2,2)}^H \cdot \mathbf{F}_{(1,1)}^H$ can be calculated according to

$$\begin{aligned} \mathbf{F}_{(1,1)}^H &= -\mathbb{E} \left[\frac{\partial^2 \ln(\mathbb{1}(\tilde{\mathbf{b}}_k | \mathbf{w}))}{\partial h_k^R \partial h_k^I} \right] \\ &= \frac{T_s}{\sigma_\Psi^2} \mathbb{E} \left[\frac{\partial}{\partial h_k^R} (2\gamma^2 |a|^2 2h_k^R) \right] = \frac{4T_s \gamma^2 |a|^2}{\sigma_\Psi^2} \end{aligned} \quad (3.91)$$

such that the CRVB of the channel estimation is derived analog to (3.73) as

$$\text{CRVB}(\mathbf{w}_i) = \left(\mathbf{F}_{(i,i)}^H \right)^{-1} = \frac{\sigma_\Psi^2}{4T_s \gamma^2 |a|^2} \mathbf{I}. \quad (3.92)$$

Based on the i.i.d property of the real and imaginary part of h_k the relation

$$\text{CRVB}(h_k) = 2 \text{CRVB}(\mathbf{w}_1) = 2 \text{CRVB}(\mathbf{w}_2) \quad (3.93)$$

from [32] can be used to obtain the CRVB of the complex channel coefficient. With no offset present, i. e., $\tau = 0$ and $\nu = 0$, $|a|^2$ is equal to 1 and (3.93) yields the lower bound

$$\text{CRVB}(h) = \frac{\sigma_\Psi^2}{2T_s \gamma^2}. \quad (3.94)$$

It only depends on the subchannel-wise signal-to-noise ratio $\frac{\gamma^2}{\sigma_\Psi^2}$ and is independent of the channel coefficient itself. Hence, the RMSE of the channel estimate is obtained individually for each subchannel and is not subject to the spectrum allocation. However, it is subject to the power level per subchannel, which depends on K_u , as defined in (3.6).

3.4.3 Evaluation with residual synchronization errors

The results from Figure 3.10 show that even for high SNR values residual offsets remain after the synchronization process, which will affect the channel estimation. In this section the RMSE of the channel estimation is evaluated by simulation for different ranges of residual offsets and compared with the derived CRVB. For the simulation of residual offsets a one-tap channel impulse response, defined as $h[n] = \delta[n]e^{j2\pi\Phi}$ with $\Phi \sim \mathcal{U}([0, 1])$, is assumed. Furthermore, τ_{\max} and ν_{\max} limit the distributions of the offsets up to the specified values. The results in Figure 3.13 reveal that for small offsets the CRVB is achieved over the whole SNR range. A small residual offset range

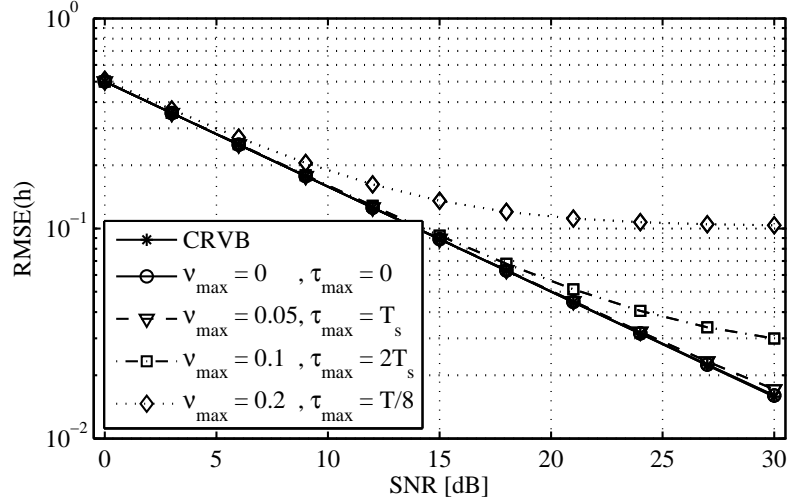


Figure 3.13: RMSE of the channel estimation with residual synchronization errors versus SNR.

with $\nu_{\max} = 0.05$ and $\tau_{\max} = T_s$ shows a slight degradation, which arise from the increased interference from the neighboring pilot symbols due to the mismatch of the SFB and AFB.

The influence of the interference on the estimation performance increases with the expansion of the residual offset range and eventually ends in an interference-induced error floor that is independent of the SNR. The calculation of the minimum achievable RMSE is described in Appendix C. Numerical evaluations of the approximations for the interference-limited RMSE are given in Table 3.2. The values at the main diagonal are related to the

τ_{\max} \ ν_{\max}	0	0.05	0.1	0.2
0	$2.5 \cdot 10^{-3}$	$7.4 \cdot 10^{-3}$	$27.2 \cdot 10^{-3}$	$100.6 \cdot 10^{-3}$
T_s	$2.5 \cdot 10^{-3}$	$7.5 \cdot 10^{-3}$	$27.3 \cdot 10^{-3}$	$100.7 \cdot 10^{-3}$
$2T_s$	$2.5 \cdot 10^{-3}$	$7.7 \cdot 10^{-3}$	$27.5 \cdot 10^{-3}$	$100.9 \cdot 10^{-3}$
$T/8$	$7.1 \cdot 10^{-3}$	$12.5 \cdot 10^{-3}$	$31.3 \cdot 10^{-3}$	$103.4 \cdot 10^{-3}$

Table 3.2: RMSE_{\min} for different residual offset ranges.

simulation-based evaluation presented in Figure 3.13. The error distribution reveals that the frequency offset has the most dominant effect on the channel estimation, where the error only depends slightly on the timing offset. This outcome corresponds to the results from the offset estimation and is due to the good spectral localization of the prototype filter.

3.4.4 Evaluation in multipath channel

Besides the influence of time and frequency offsets on the channel estimation, a second effect of performance degradation is the ISI and ICI introduced by multipath propagation of the signal. The Rayleigh fading channel is emulated in the following evaluation by an exponential-decaying PDP defined according to $E[|h[nT_s]|^2] \propto e^{-\frac{nT_s}{\tau_{rms}}}$ with $n \in \{0, \dots, 4K - 1\}$. The PDP is normalized such that $\sum_{n=0}^{4K-1} E[|h[nT_s]|^2] = 1$ and the channel is static for each run but is varied between runs. The evaluated PDPs are related to the PDPs defined at the beginning of this chapter for the evaluation of the STO and CFO estimation algorithms. In Figure 3.14 the RMSE is given in dependence of the

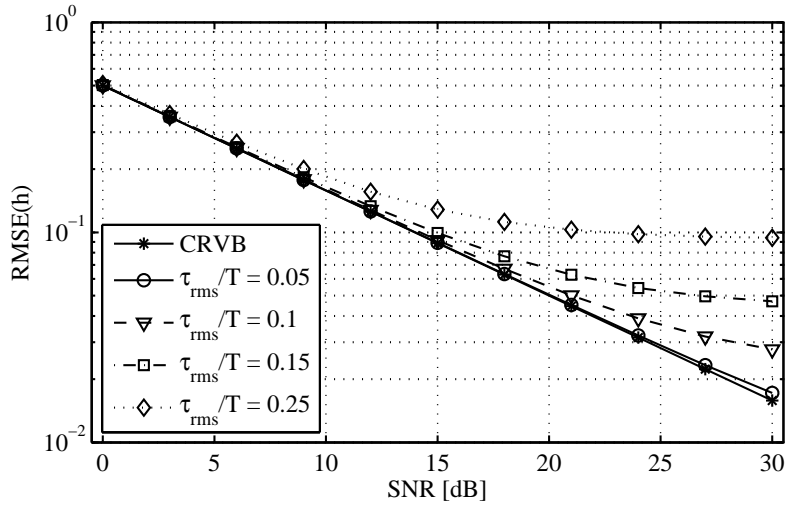


Figure 3.14: RMSE of the channel estimation versus SNR in dependence of the mean delay spread τ_{rms} .

mean delay spread τ_{rms} normalized to one symbol duration T . A small delay spread of 0.05 or below causes no significant interference on the pilot symbols for the given SNR range, which is mainly due to the sparse preamble design. However, for larger delay spreads the degradation of the estimates due to ISI increases and an error floor becomes apparent.

In literature, the normalized MSE (NMSE) is often used to evaluate the estimation accuracy of the channel estimation, as for example presented in [46]. The NMSE takes into account the scaling of the error in dependence of the amplitude of the true channel coefficient. Using Jensen’s inequality and

with the definitions of $\text{MSE} = \text{RMSE}^2$ and the NMSE, the different metrics can be compared according to

$$\text{NMSE} = \mathbb{E} \left[\frac{|\hat{h}_k - h_k|^2}{|h_k|^2} \right] \geq \frac{\mathbb{E} [|\hat{h}_k - h_k|^2]}{\mathbb{E} [|h_k|^2]} = \mathbb{E} [|\hat{h}_k - h_k|^2] = \text{MSE}. \quad (3.95)$$

The assumption that $\mathbb{E}[|h_k|^2] = 1$ is valid, given that the PDP is normalized with respect to the power. Hence, the MSE, and related to it the RMSE, provides an approximation of the achievable NMSE.

3.4.5 Concluding remarks

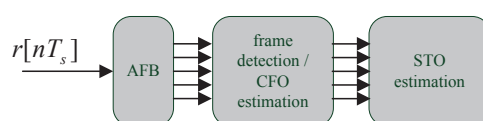
The discussed performance of the channel estimation is linked to the system level performance of synchronization algorithms. Even though the RMSE is a suitable metric for the determination of the residual offset error for synchronization algorithms, its relation to the overall system performance, i. e., the resulting BER and FER, is not obvious. The combination of channel estimation and equalization reduces or compensates some of the errors that are included in the offset error analysis and, hence, can improve the system performance. However, the channel estimation is influenced by the residual offset, as the analysis reveals. It shows that small frequency offsets up to a CFO of 10% have only a minor impact on the channel estimation error. The previous analysis of the CFO estimation leads to an RMSE that is well below this 10% limit. Hence, it is concluded that the BER and FER, which are presented in the following, are dominated by residual synchronization errors itself, rather than by a distortion of the channel estimate due to these errors. A similar 10% limit holds for the maximum amount of delay spread for which the channel estimation performs nearly undisturbed.

CONCEPT EVALUATION

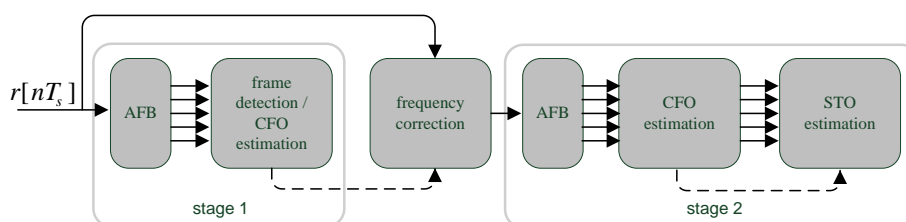
In this chapter synchronization concepts based on the previously described FD algorithms are developed and compared with a TD reference solution. The concepts are evaluated based on the RMSE criterion as well as on the uncoded BER and their computational complexity. Offline measurements are conducted to verify the practicability of FD processing for frame detection and synchronization.

4.1 SYNCHRONIZATION CONCEPTS

This work proposes two different concepts for initial frame detection and synchronization, named Concept 1 and Concept 2, in the following. The con-



(a) Concept 1



(b) Concept 2

Figure 4.1: Block diagrams of the FD concepts for synchronization.

cepts are illustrated in Figures 4.1a and 4.1b, where dashed lines indicate the exchange of information about the frame start and estimated CFO value and

solid lines indicate the flow of received samples in TD (single path) or blocks in FD (parallel paths). The concepts are described in the following.

- **Concept 1:** The demodulation of the received samples is only performed once and CFO estimation and STO estimation are performed on the same unsynchronized demodulated signal.
This concept reflects the straightforward utilization of the FD algorithms from Chapter 3 and results in the least complex implementation. However, it disregards that the estimation performance of the algorithms depends on the CFO.
- **Concept 2:** In contrast to Concept 1, in this concept the CFO is compensated after frame detection to reduce the residual CFO to the range $|\nu| \leq 0.1$ to avoid degradations in the second stage, as indicated in Figure 3.11. After correction of the CFO in the TD based on the first estimate the offsets can be estimated a second time. It yields better estimates which significantly lowers the effect of interference on the performance.

The two concepts are assessed in terms of achievable RMSE and by means of the uncoded BER for the two relevant STO estimators, CFE and CCE. The frame structure used in the evaluation is the one described in Figure 3.2 including auxiliary pilots and payload symbols.

4.1.1 Time domain reference concept

The performance of the FD synchronization needs to be compared with existing TD solutions to give an answer to the research question posed in this work. For that reason, we introduce a reference TD synchronization concept that makes use of the auto correlation metric for frame detection and CFO estimation based on the principles reported in [71]. For fine timing synchronization a cross correlation metric is used for TD processing, as suggested in [19]. A block diagram of the TD concepts is given in Figure 4.2. The TD metrics can make use of both preamble designs, as defined in (3.5) and (3.7). The shorter preamble, designed for FD processing, leads to a minor performance degradation in comparison to the ideal preamble design for TD processing. The difference for the CFO estimation is evaluated in Appendix D.

With the undistorted received signal $r[nT_s] = s[nT_s]$ the auto correlation metric, as described in [70], leads to

$$C[\tilde{n}T_s] = \sum_{n=\tilde{n}}^{\tilde{n}+K-1} r^*[nT_s]r[nT_s + T] \quad (4.1)$$

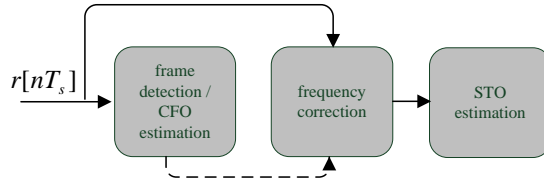


Figure 4.2: Block diagram of the TD concept for frame detection and estimation.

with the energy metric $Q[nT_s]$ equal to

$$Q[\hat{n}T_s] = \frac{1}{2} \sum_{n=\hat{n}}^{\hat{n}+K-1} |r[nT_s]|^2 + |r[nT_s + T]|^2 \quad (4.2)$$

$$\approx \sum_{n=\hat{n}}^{\hat{n}+K-1} |r[nT_s]|^2. \quad (4.3)$$

Based on $C[\hat{n}T_s]$ and $Q[\hat{n}T_s]$, the frame detection is performed as a maximum search over the metric

$$\hat{n}T_s = \underset{\hat{n}T_s}{\operatorname{argmax}} \left(\frac{|C[\hat{n}T_s]|}{Q[\hat{n}T_s]} \right) \quad (4.4)$$

followed by the decision

$$|C[\hat{n}T_s]| > \rho_{TD} Q[\hat{n}T_s] \quad (4.5)$$

based on the threshold value ρ_{TD} . If (4.5) is fulfilled, $\hat{n}T_s$ is the time instance at which the start of the frame is coarsely located.

$C[nT_s]$ is evaluated based on the TD estimator (TDE), as defined in [29], to obtain an estimate of the normalized CFO according to

$$\hat{\nu}_{TDE} = \frac{\angle C[\hat{n}T_s]}{2\pi}. \quad (4.6)$$

After coarse estimation of the preamble start, the fine timing estimation of the STO is achieved with the help of the cross correlation metric after the CFO has been compensated. The cross correlation window size is set to $T/2$. Hence, the STO estimation yields

$$\hat{\tau}_{TDE} = \underset{-T/4+T_s \leq \hat{\tau} \leq T/4}{\operatorname{argmax}} \left(\frac{\left| \sum_{n=0}^{2K-1} r_{\hat{\nu}}^*[\hat{n}T_s + nT_s + \hat{\tau}] s[nT_s] \right|}{Q_{cc}[\hat{\tau}]} \right) \quad (4.7)$$

with the frequency corrected received signal¹

$$r_{\hat{\nu}}[nT_s] = r[nT_s] e^{-j \frac{2\pi}{T} \hat{\nu}_{TDE} nT_s} \quad (4.8)$$

¹ For the cross correlation metric in (4.8) it does not matter whether $r[nT_s]$ or $s[nT_s]$ is frequency corrected. However, $r[nT_s]$ is chosen here to comply with the FD approach.

and the energy normalization factor

$$Q_{cc}[\tilde{\tau}] = \sum_{n=0}^{2K-1} |r[\hat{n}T_s + nT_s + \tilde{\tau}]|^2 + |s[nT_s]|^2. \quad (4.9)$$

The TD concept is used in the following for the simulation-based as well as for the measurement-based evaluation.

4.1.2 Concluding remarks

In this section we proposed two synchronization concepts that base on the FD algorithms derived in the previous chapter. Concept 1 is the straightforward implementation of the FD approach, whereas Concept 2 takes the CFO-dependent performance of the FD CFO estimator into consideration. Furthermore, to enable a fair comparison between the FD and TD approach to synchronization, a TD reference concept is discussed, which will be used in the following evaluation of the concepts to provide an answer to the fourth question of the problem statement.

4.2 SIMULATION-BASED EVALUATION

For the simulation results presented in this chapter the parameter defined in Chapter 3 are used. However, in contrast to the evaluation of the core algorithms in the previous chapter, outliers showing an absolute error greater than $T/4$ and 0.5 for the estimation of the STO and CFO, respectively, are considered as falsely detected and are not included in the performance results. The number of discarded estimations of this kind is well below 1% in case of AWGN and below 5% in case of Rayleigh fading channel conditions for the evaluation versus SNR. The selection of the results enables the meaningful representation of the BER which otherwise would be corrupted by estimation errors that yield a BER close to 0.5. Furthermore, it is assumed that the block index of the frame start is known, hence, the frame detection, described in (3.23) and (4.5), has no influence on the simulation results.

The results from Figure 3.7 indicate that the CFO has only a weak influence on the STO estimation. Hence, the difference between Concept 1 and 2 regarding the STO estimation is expected to be small, which is supported by the results in Figure 4.3. In case of Concept 2 with CCE one exception can be observed. Obviously, the additional consideration of the CFO to improve the estimation leads in some rare cases to timing errors due to an erroneous compensation of the CFO in (3.58), which could not be observed in the results for Concept 1. In all cases, the additional payload leads to a degradation

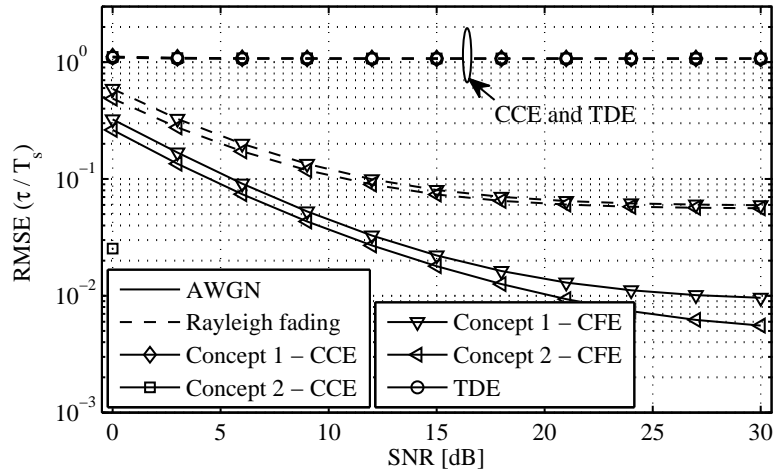


Figure 4.3: RMSE of the STO estimation versus SNR in dependence of the concept.

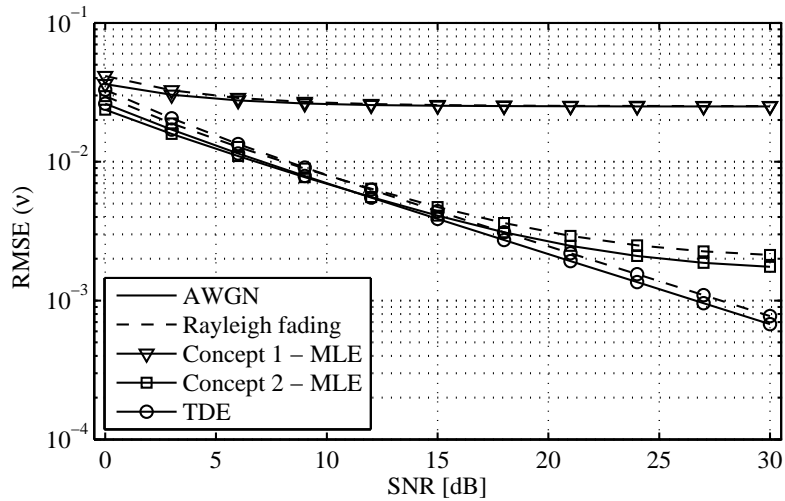


Figure 4.4: RMSE of the CFO estimation versus SNR in dependence of the concept.

of the estimations due to the increased interference. The TDE and the CCE have the same estimation performance because both algorithms are based on a maximum search with trial values that are multiples of T_s .

Even though the STO estimation does not benefit from the additional effort in Concept 2, the results in Figure 4.4 clearly show that it offers a significant lower interference-induced error floor for the CFO estimation compared to Concept 1 for the FD processing. The introduction of the second stage achieves a CFO estimation that is independent of the actual CFO value, which is shown in Figure 4.5 by the evaluation of the CFO estimators versus fixed CFO values. The Concept 2 achieves a constant performance over the whole CFO range which is comparable to the performance of the TDE. The slight

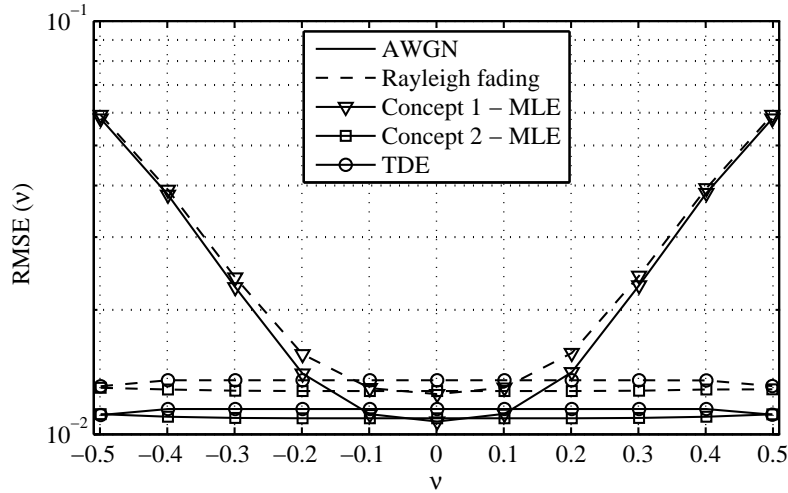


Figure 4.5: RMSE of the CFO estimation versus CFO in dependence of the concept at an SNR of 6 dB.

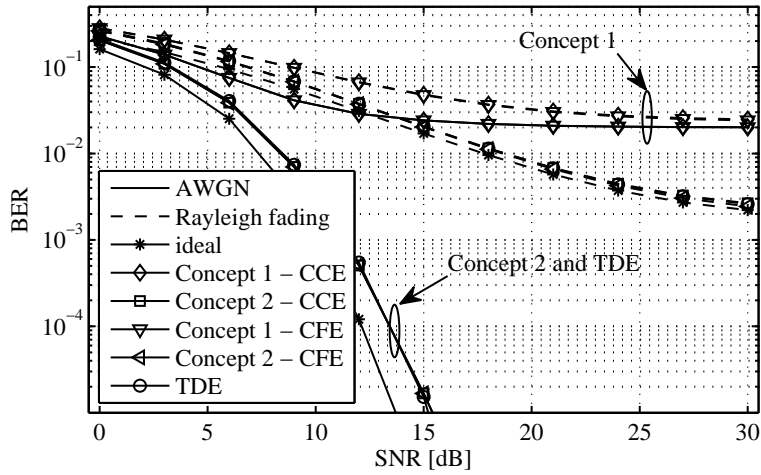


Figure 4.6: BER versus SNR in AWGN and Rayleigh fading. The payload QAM symbols are QPSK modulated.

decrease of the curve for the TDE at $|\nu| \approx 0.5$ results from the removal of false estimations.

The evaluation of the BER, plotted in Figure 4.6, provides a system view on the performance of the estimators. It can be observed that the difference between the CFE and the CCE is not significant when it comes to BER performance. The OQAM-OFDM system itself shows a robustness against offsets which depends on the pulse shape, as discussed in [27, 50, 51]. Hence, a certain range of residual offsets is tolerable with only minor impact on the BER performance. Combined with the ability of the channel equalizer to effectively reduce the rotation of the phase per subchannel, caused by small timing offsets, it leads to a BER performance which is close to the ideal case. For the

ideal case perfect knowledge of the offsets and the channel coefficients is assumed. On the contrary, residual frequency offsets result in a phase drift over time with a high impact on the constellation diagram at receiver side if they are not tracked. Hence, Concept 1 approaches the BER floor at $2 \cdot 10^{-2}$ in both AWGN and Rayleigh fading condition. The results for Concept 2 indicate that the gain in CFO estimation accuracy is sufficient to get close to the ideal BER performance for AWGN and to match it in Rayleigh fading environments.

4.2.1 Effect of auxiliary pilots

The influence of auxiliary pilots on the quality of the estimation is discussed in this section. Due to the pre-calculation of the interference at transmitter side, the introduction of a channel, i. e., $\tau \neq 0$ and $\nu \neq 0$, degrades the performance of the auxiliary pilots because the actual system impulse response differs from the calculated one. For the estimation algorithms discussed here the first and the third block of the preamble are used for estimation either to reduce the effect of noise as for the STO and channel estimation or to enable the estimation as in case of the closed-form CFO estimation. Hence, it needs to be considered for the discussion of the results that the estimation algorithms average over two blocks from which only one is potentially affected by the interference from the payload symbols. The benefit of using auxiliary pilot symbols even in the case of offsets is presented in Figures 4.7 to 4.10. For illustration of this benefit we opted for the simulation-based approach of the estimation algorithms rather than the analytical treatment of the interference $\iota_{k,m}$, because a one-to-one relation between interference level and estimation accuracy is not straightforward to derive. In the considered SNR range the TD estimations are unaffected by the auxiliary pilots as a result of the small amplitude of the auxiliary pilot symbols compared to the pilot symbols $b_{k,m}$. The maximum energy of the auxiliary pilots reaches only 5% of the energy of the pilot symbols for the given system configuration. In Figure 4.7 the payload interference leads to an increase of the error floor of the STO estimation for both Concept 1 and 2. The effect cannot be observed for SNR values below 10 dB as the noise dominates the estimation here. However, the TDE shows no degradation in estimation performance in both cases and no error can be observed, as discussed previously. A similar observation can be made in Figure 4.8, where the CFO estimation floor increases due to the lack of the interference-canceling influence of the auxiliary pilots. Hence, the CFO estimation can be improved by the introduction of the auxiliary pilots.

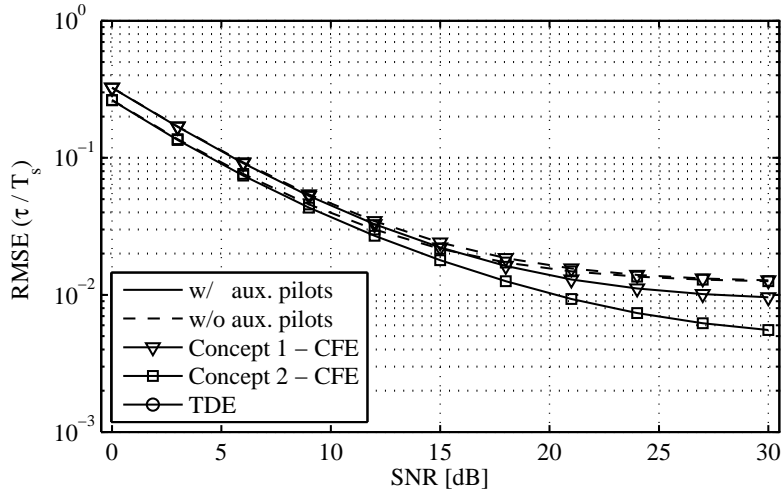


Figure 4.7: RMSE of the STO estimation versus SNR with and without auxiliary pilots.

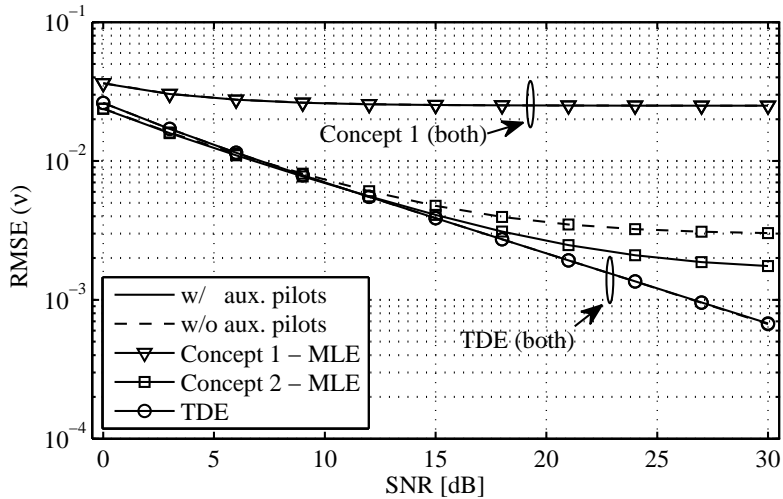


Figure 4.8: RMSE of the CFO estimation versus SNR with and without auxiliary pilots.

The channel estimation benefits from the auxiliary pilots in the same way as observed for the STO and CFO estimation, which is indicated by the results in Figure 4.9. The overall BER performance, as presented in Figure 4.10, is only slightly degraded for the case that no auxiliary pilots are deployed. Even though the BER performance is not affected significantly by the removal of the auxiliary pilot scheme in the lower SNR range using QPSK modulation, the estimation of STO, CFO, and channel coefficients benefit from the introduction of the auxiliary pilots for higher value of SNR. For that reason, the preamble proposed in Section 3.1 will be used for the verification by measurements, that is presented in Section 4.4.

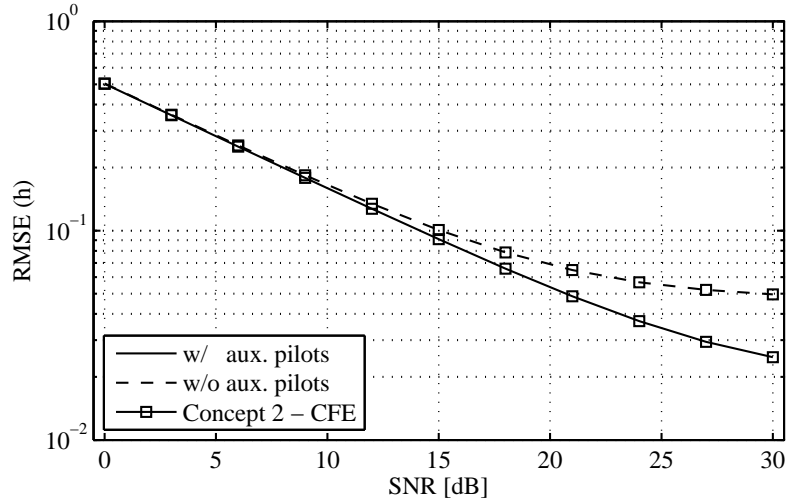


Figure 4.9: RMSE of the channel estimation versus SNR with and without auxiliary pilots.

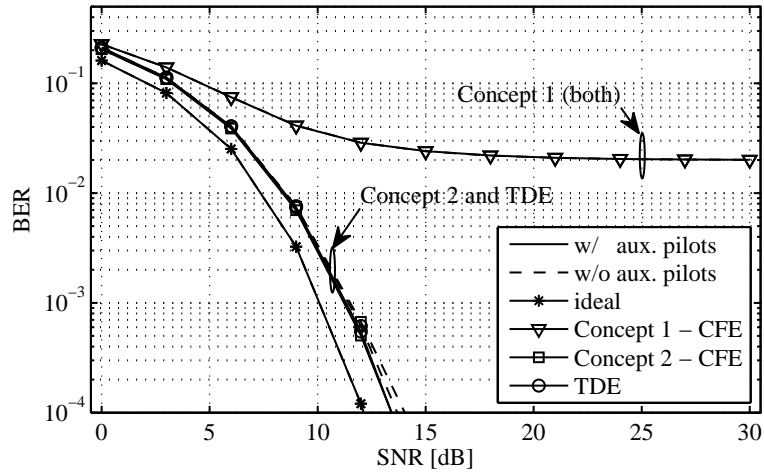


Figure 4.10: BER versus SNR with and without auxiliary pilots.

4.2.2 Concluding remarks

From the evaluation of the concepts it is concluded that the proposed FD approach with Concept 2 achieves the same BER performance as its TD counterpart for the evaluated scenarios. However, the utilization of Concept 1 results in a BER floor and severely degrades the system’s performance due to the dominant effect of the residual CFO estimation error. Hence, the first part of the fourth question, if the FD approach achieves the same performance as its TD counterpart, is answered in this section. However, the complexity has not been considered yet, but will be addressed in the following section.

4.3 COMPUTATIONAL COMPLEXITY

In this section the complexity of the concepts is derived and compared to obtain their cost of implementation.

The necessary demodulation step for FD processing adds more complexity to the synchronization stage in comparison to common TD methods. The costs of FD processing and the related algorithms are evaluated in terms of the number of complex multiplications needed to perform frame detection and synchronization. With the help of this complexity analysis the FD approach can be assessed in terms of performance and cost of implementation to answer the research question. Operations that involve additions are assumed to take significantly less resources than multiplications and are thus not considered in the complexity analysis. This holds similarly for taking the absolute value and the angle of a complex number. Furthermore, divisions and real multiplications are treated as complex multiplications and the generation of a vector of the form e^{jx} with $x \in \mathbb{R}$ is considered to take no additional resources. The number of complex multiplications Ω is calculated for $K/2$ processed samples in the TD, which corresponds to the $T/2$ time shift of each demodulated block for the OQAM-OFDM scheme, as described in Chapter 2. For the evaluation of the complexity $K_2 = K_u/2$ and $K_u = K$ are assumed, if not otherwise stated.

4.3.1 Frame detection

The complexity of the demodulation step in combination with the frame detection, denoted by $\Omega_{\text{detection (FD)}}$, is calculated according to

$$\begin{aligned} \Omega_{\text{detection (FD)}} &= \underbrace{\frac{K}{2} \log_2(K) + \beta K}_{\text{FFT + PPN [59]}} + \underbrace{3K_2 + n_u}_{\text{frame detection (3.19)-(3.23)}} \quad (4.10) \\ &= K \left(\frac{\log_2(K)}{2} + \beta \right) + 3K_2 + n_u. \end{aligned}$$

For the demodulation process, that is the shift of the signal from time to frequency domain, the complexity heavily depends on the number of subchannels K and, to a smaller amount, on the overlapping factor β . The influence of β on the demodulation becomes smaller for increasing K . In this analysis the efficient polyphase network implementation of the filterbank scheme, as described in [74], is taken into consideration. Furthermore, in the calculations the metrics in (3.20) and (4.2) are considered where the scaling factor of $1/2$ is neglected due to its simple implementation through bit-shifting.

For frame detection in the FD the complexity depends only marginally on the number of users or frequency bands, defined as n_u . In case of $n_u > 1$ the available number of subchannels for detection K_2 is split according to the spectrum allocation. However, the sum over all is assumed to be equal to K_2 and guard bands between subbands are neglected, leading in good approximation to an independence of the frame detection complexity from the parameter n_u .

TD frame detection, however, needs a single detection stage per subband using the complete window size of K , which leads to a linear scaling of the complexity with n_u . For a single subband the complexity is defined as

$$\Omega_{\text{detection (TD)}} = \underbrace{2K}_{\text{frame detection (4.1) - (4.5)}}. \quad (4.11)$$

The complexity calculation is based on the moving window approach, where only one new correlation value needs to be calculated per sample shift. The rest of the sums in (4.1) and (4.2) is stored in memory. $\Omega_{\text{detection (TD)}}$ is calculated for the same block size of $K/2$ as used for the FD frame detection in (4.10).

The straightforward extension of the TD frame detection to shared spectrum scenarios leads to the use of a prefiltering stage, as described in Chapter 2 and defined in (2.27). In [59] the complexity of an efficient implementation of the convolution is given by $\frac{KN}{2L} \log_2(2N)$ with the filter length $L = \beta K$ and the FFT-size $N_{\text{filter}} = 2^{\lceil \log_2(L + \beta K - 1) \rceil}$. Hence, the overall number of multiplications is calculated to be

$$\Omega_{\text{filter \& detection (TD)}} = n_u \left(\underbrace{\frac{KN_{\text{filter}}}{2L} \log_2(2N_{\text{filter}})}_{\text{prefiltering stage (2.27)}} + 2K \right) \quad (4.12)$$

for the TD method including the subband prefiltering stage. The complexity scales linearly with the parameter n_u . From Figure 4.11 it becomes apparent that the FD processing adds complexity just in demodulation and frame detection by a factor of five compared to the TD metric. However, the complexity of the TD approach needed for frame detection significantly exceeds the one for the FD approach if non-contiguous spectrum is considered.

4.3.2 Offset estimation

The offset estimation is triggered by the decision of the frame detection metric. For that reason, its complexity is evaluated on the basis of a single frame detection rather than on the basis of blocks. The CFO estimation metrics,

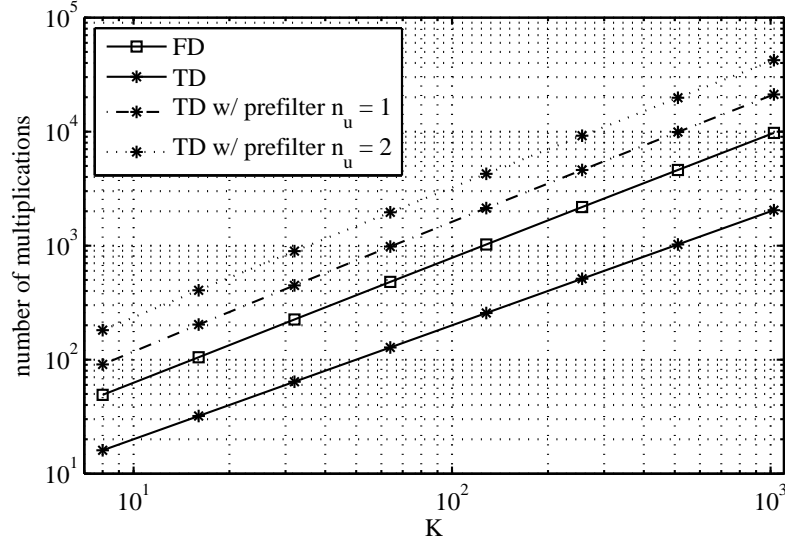


Figure 4.11: Computational complexity of frame detection and CFO estimation per processed OQAM-OFDM block.

described in (3.49) and (4.6), can be obtained directly from the frame detection metrics (3.19) and (4.1), respectively, while disregarding scaling factors. Hence, the cost of the CFO estimation is not taken into account because its contribution is not significant compared to the amount of the complexity added by the STO estimation. The complexity of the STO estimators $\Omega_{\text{CFE } i}$ and $\Omega_{\text{CCE } i}$ using either Concept 1 or 2 are indicated accordingly. The number of multiplications for Concept 1 with CFE leads to

$$\Omega_{\text{CFE } 1} = \underbrace{2K_p + 1}_{\text{STO estimation (3.56)}} \quad \text{with } K_p = K_2 - 1, \quad (4.13)$$

where the simple switch of the sign as a result of the denominator $b_{k,i} b_{k+\Delta_k,i}^*$ is not considered. The effort to compensate for the CFO in Concept 2 is taken into account by the multiplication of the TD preamble signal with the signal $e^{-j\frac{2\pi}{T} \hat{\nu} n T_s}$ and the following demodulation. Hence, the complexity is defined as

$$\begin{aligned} \Omega_{\text{CFE } 2} &= \underbrace{(2\beta + 2)(K/2 + K/2 \log_2(K) + \beta K)}_{\text{CFO correction and demodulation}} \\ &\quad + \underbrace{K_2 + 1 + 2K_p + 1}_{\text{CFO (3.49) and STO (3.56) estimation}} \\ &= K(\beta + 1)(\log_2(K) + 2\beta + 1) + K_2 + 2K_p + 2. \end{aligned} \quad (4.14)$$

The preamble, defined in (3.5), results in a TD signal of length $K(\beta + 1)$ samples which can be divided in groups of $2\beta + 2$ blocks, containing $K/2$ samples each. Due to the additional demodulation step the complexity increases sig-

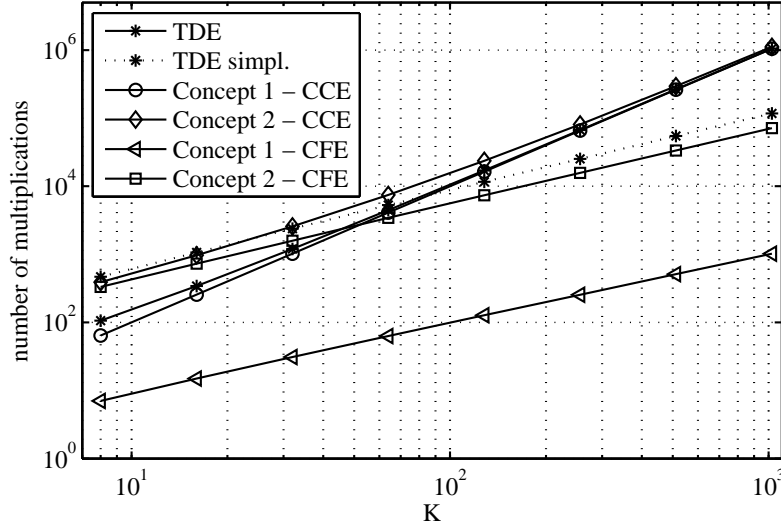


Figure 4.12: Computational complexity of STO estimation in number of complex multiplications per detected frame.

nificantly, as the evaluation of (4.13) and (4.14) versus K in Figure 4.12 reveals.

The cross correlation based STO estimation CCE results in a complexity according to

$$\Omega_{\text{CCE } 1} = \underbrace{2KK_2}_{\text{STO estimation (3.58)}} \quad (4.15)$$

The CCE performs a maximum search over $K/2$ trial values each having a cost of $2(2K_2)$ complex multiplications. The first factor of two results from the multiplication $\tilde{b}_{k,i} e^{-j\pi\hat{\nu}i}$ and the multiplication of its result with the trial value $b_{k,i} e^{-j\frac{2\pi}{T}k\hat{\tau}}$. However, the trial values can be calculated in advance and stored in memory. The second factor results from the sums over $2K_2$ values. Addition of $\Omega_{\text{CCE } 1}$ to the demodulation stage, as derived in (4.14), yields

$$\begin{aligned} \Omega_{\text{CCE } 2} &= \underbrace{(2\beta + 2)(K/2 + K/2 \log_2(K) + \beta K)}_{\text{CFO correction and demodulation}} \quad (4.16) \\ &\quad + \underbrace{K_2 + 1 + K/2(4K_2)}_{\text{CFO (3.49) and STO (3.58) estimation}} \\ &= K(\beta + 1)(\log_2(K) + 2\beta + 1) + K_2(2K + 1) + 1 \end{aligned}$$

for the complexity of the Concept 2 with CCE.

The TD STO estimation metric performs a maximum search in the range of $\{-T/4 + T_s, T/4\}$ which results in $K/2$ values to be tested. One multiplication per trial value is needed for power normalization in (4.9). By setting the window size of the cross correlation to $2K$ samples and considering the

two complex multiplications as a result of the cross correlation and frequency shifting the calculation of (4.7) yields

$$\begin{aligned}\Omega_{\text{TDE}} &= \underbrace{2(2K + K/2 - 1)}_{(4.8),(4.9)} + \underbrace{K/2(2K + 1)}_{\text{STO estimation (4.7)}} \\ &= K^2 + \frac{11K}{2} - 2.\end{aligned}\quad (4.17)$$

In (4.17) $2K + K/2 - 1$ multiplications are considered for the part described in (4.8) and $2K + K/2 - 1$ multiplications are taken into account for the energy factor calculation from (4.9). The window size of the correlation can be increased to achieve a more accurate estimate in the low SNR regime, however, the complexity increases as well. The window size of $2K$ is taken here for fairness reasons as it corresponds to the FD equivalent of two blocks. The complexity of the cross correlation can be further reduced by setting the energy normalization in (4.9) to a constant value. This is a valid simplification if the received signal $r[nT_s]$ has constant power over the period of the preamble. When the cross correlation is treated as a convolution the computation can be shifted to the FD with an FFT-size equal to $N_{\text{TDE}} = 2^{\lceil \log_2(4K + K/2 - 1) \rceil}$ for a window size of $2K$ and a shift range of $K/2$ samples. The calculation of the correlation of the sequence $r_{\hat{v}}[nT_s]$ and $s[nT_s]$ in the FD costs $N_{\text{TDE}} \log_2(2N_{\text{TDE}})$ multiplications [59] which leads to a complexity of

$$\begin{aligned}\Omega_{\text{TDE simpl.}} &= \underbrace{2K + K/2 - 1}_{\text{CFO correction (4.8)}} + \underbrace{N_{\text{TDE}} \log_2(2N_{\text{TDE}})}_{\text{simplified STO estimation}} \\ &= 5K/2 - 1 + N_{\text{TDE}} \log_2(2N_{\text{TDE}}).\end{aligned}\quad (4.18)$$

The transformation of the sequence $s[nT_s]$ can be calculated in advanced and stored in memory and is not taken into account in (4.18). However, the necessary assumption does not hold in general and the simplified metric may only perform sufficiently well in adequate scenarios. For that reason, it is presented here as an alternative reference design only, but is not further used in this work.

The complexity evaluation from Figure 4.12 shows the results for the case that $K_u = K/2$. In case that only a part of the available spectrum is used for synchronization the complexity is plotted against the subband allocation K_u/K in Figure 4.13. The results show that the complexity of both STO estimators for Concept 1 scales with the number of occupied subchannels, as indicated by the factor K_2 in (4.13) and (4.15). However, for the TD solution and approximately for Concept 2 the subchannel allocation does not influence the complexity.

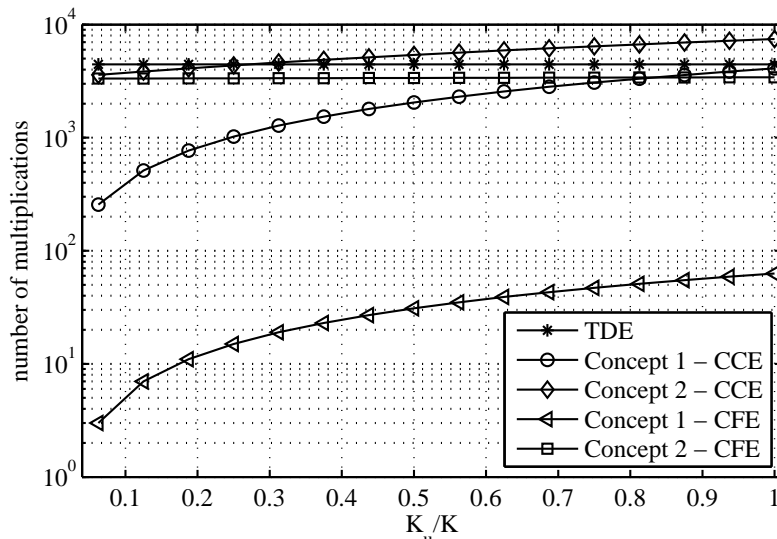


Figure 4.13: Computational complexity of STO estimation in dependence of the sub-band allocation for $K = 64$.

4.3.3 Concluding remarks

In this section we showed that frame detection in the FD adds a factor of five in complexity compared to a TD solution as a result of the AFB involved in the FD processing. However, if a prefiltering stage is needed to enable fragmented spectrum transmission, the complexity of the TD approach significantly exceeds the one necessary for FD processing. Furthermore, the complexity analysis reveals for Concept 2 a significant increase of additional complexity for both practical STO estimators by involving a frequency correction of the samples in the TD and their demodulation. A trade-off between performance and complexity can be achieved by a selective switching between Concept 1 and Concept 2 in dependence of the CFO, which is estimated with the help of (3.49). Hence, the outcome of this section answers the question how the FD approach compare with the TD approach in terms of complexity.

Nevertheless, it has to be considered that for an uncoordinated system like WiFi the frame detection will be active most of the time to capture the transmitted frames, as the receiver has no information about the time of transmission. Hence, the FD approach to multi-user synchronization significantly reduces the complexity of frame detection. In a coordinated system, frame detection is only needed once for the link initialization. Afterwards, only offset estimation is used to track changing STOs and CFOs.

It follows that the type of system, uncoordinated or coordinated, should be considered for a more specific evaluation of the costs of processing.

4.4 MEASUREMENT-BASED VERIFICATION

In this section the measurement-based verification of the concepts in a practical setup is presented. The previous evaluation of the concepts and algorithms leads to the conclusion that the performance of Concept 1 depends on the actual value of CFO, whereas Concept 2 can achieve a sufficient performance for the complete CFO range. Furthermore, for the STO estimation, the CFE yields similar performance as the CCE, but is of lower complexity. Hence, the focus is on the CFE for STO estimation in the following verification of the concepts.

4.4.1 Measurement setup

For the measurement setup the Universal Software Radio Platform (USRP) is chosen as the transceiver platform. The USRPs² are connected by cable with an attenuator in between for tuning the SNR. In Figure 4.14 a block diagram of the measurement setup is presented for illustration.

Dashed lines indicate the flow of baseband IQ samples from and to the computer, whereas solid lines represent the RF cable connections between the USRPs, the attenuator, and the 10 MHz reference clock. The measurements

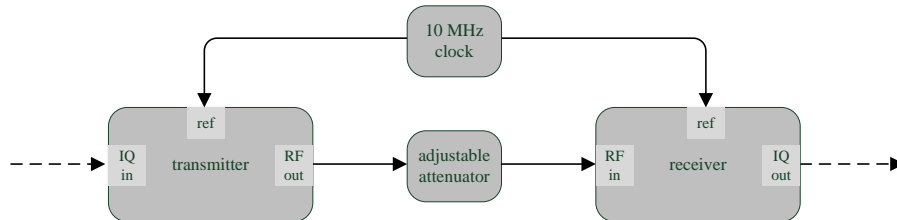


Figure 4.14: Block diagram of the offline measurement setup.

are carried out in an offline fashion, i. e., burst transmission with pre- and post-processing in Matlab. The measurement setup and parameter settings are described in detail in the following.

- The number of subchannels is set to $K = 64$ with $K_u = 50$ and $\mathbb{K}_u = \{-25, -24, \dots, -1, 1, 2, \dots, 25\}$.

² Model N210 rev. 2 [3], SBX daughterboard, rev. 3 [4], Gnuradio version 3.7.1 [2], UHD version 3.5.4, Ubuntu 12.04 64bit

- The sequence λ_k from (3.5) is chosen such that the PAPR of the TD preamble signal is minimized.
- The transmitted frames are combined to a burst that contains 10^3 frames. The timing distance between frames is composed of a fixed offset of $10T$ and a variable offset drawn from a uniform distribution in the range of $\{-T, T\}$ for each frame individually to ensure sufficient separation of the frames and to model random transmission.
- The number of real-valued payload symbols $d_{k,m}$ per frame is $4K_u$. With QPSK-modulation of the complex-valued payload symbols $q_{k,u}$, it results in the number of uncoded bits per frame to be $n_{\text{bits}} = 200$. Each frame contains different randomly generated payload bits.
- The uncoded bits are convolutional coded with a code rate of $2/3$ followed by a block interleaving of the coded bits. After QAM demapping, the received bits are decoded by a Viterbi decoder with hard decision.
- The sampling rate of the USRPs is set to 12.5 MHz, which results in a subchannel spacing of $f_{\Delta} = 195.313$ kHz and a symbol duration of $T = 5.12\mu\text{s}$.
- The hardware is tuned to a center frequency of 750 MHz, which is supported by a 10 MHz reference signal as a common clock source for the local oscillators of the USRPs. Deviations of the local oscillators leave a frequency offset of -0.367 kHz between the transmitting and receiving USRPs. The hardware offset is only taken into account during the discussion of the results where explicitly mentioned. Otherwise, the hardware imposed frequency offset is neglected due to its small value of approximately 0.2% of the subchannel spacing. Furthermore, the USRP supports the tuning of its local oscillator only for discrete frequency steps. Hence, the frequency offset is tuned to the frequency that is nearest to the desired one. However, the values of ν , that are considered in the measurements, are displayed as $\nu = \{0, 0.2, 0.4\}$, because the resulting deviations from the exact value of ν are not relevant for the discussion.
- The amplifier gain of the transmitting USRP is set to 0 dB to avoid non-linear behavior of the amplifier at the transmitter. At receiver side the amplifier gain is set to 10 dB to achieve an SNR in the range from 0 dB to 24 dB by adjusting the variable attenuator.
- The frame detection threshold is set to $\rho = 0.4$, which yields a $P_{\text{m,d}}$ of 10^{-2} at 0 dB SNR. The threshold is derived for 0 dB SNR from Figure 3.3, which represents the worst-case scenario of the SNR for the

measurements. The threshold decision is a trade-off between $P_{m,d}$ and $P_{f,a}$ to minimize both metrics simultaneously. The minimization of both probabilities is essential for the following evaluation to avoid distortions of the FLR. A value for ρ_{TD} to achieve the same $P_{m,d}$ is not explicitly derived in this work. However, due to the accordance of the analytical derivations of the FD and TD frame detection performance, the threshold is set to $\rho_{TD} = \rho$.

The measurements are made offline to compare the concepts based on the same set of received baseband IQ samples. Different to the previously shown simulation-based evaluation, the exact timing of the frame start is not known in the measurement setup. It corresponds to the case of a practical system, where the offsets are also not known prior to estimation. Hence, for the evaluation it is assumed that the STO is distributed equally. However, the CFO is set and fixed throughout one measurement.

4.4.2 Frame loss criterion

The FLR is defined as the ratio between the number of correctly received frames n_{rx} and the number of transmitted frames n_{tx} according to $FLR = \frac{n_{rx}}{n_{tx}}$. It is used here as a metric to quantify the frame detection performance of the synchronization schemes. The decision whether a frame is detected correctly or not is based on the resulting uncoded BER per frame due to the lack of the knowledge of the actual offset values in the measurement setup. A BER close to 0.5 indicates a false detection of a frame start, whereas a BER below the BER threshold ρ_{BER} , that is derived in the following, indicates a correct detection. Hence, a frame is considered to be detected but not synchronized correctly if the frame detection threshold ρ is exceeded and estimation errors lead to a significantly higher BER compared to the BER that is expected from theoretical derivations for the given SNR. The BER threshold ρ_{BER} should be set such that the probability for a false positive (P_{fp}), i. e., that a frame is considered as correctly received even though it is not synchronized correctly, and the probability of a false negative (P_{fn}), i. e., that a frame is discarded even though it is received correctly, are both minimized.

For the derivation of P_{fp} , it is assumed that the detected frame start deviates at least one symbol duration, i. e., $T/2$, from the true frame start. Hence, demodulation of the falsely detected frame yields a BER per frame with a mean value of $BER_{fd} = 0.5$, where the bit errors are assumed to be indepen-

dent from each other. This assumption leads to a binomial distribution of the bit errors, denoted by $\mathcal{B}(n_{\text{bits}}, \text{BER}_{f_p})$. It follows for the derivation of P_{f_p} that

$$P_{f_p} = \int_{x=0}^{\rho_{\text{BER}}} \mathcal{B}(n_{\text{bits}}, \text{BER}_{f_d}) dx. \quad (4.19)$$

In contrast to the P_{f_p} , the P_{f_n} depends on the SNR. Hence, the P_{f_n} is derived for the lowest SNR of 0 dB that is used in the measurements. The analytical derived probability of a bit error in AWGN channels, denoted by BER_{c_d} , is defined in [42] for correct frame detection and synchronization. Its evaluation for QPSK modulation yields

$$\text{BER}_{c_d} = \text{erfc}(\sqrt{1/2})/2 = 0.1587. \quad (4.20)$$

The analytical BER matches the observation made from Figure 4.6 that a BER of approximately 0.16 is achieved for ideal synchronization at an SNR of 0 dB. Under the assumption that the bit errors are independent from each other, the PDF is calculated from $\mathcal{B}(n_{\text{bits}}, \text{BER}_{c_d})$ according to

$$P_{f_n} = \int_{x=\rho_{\text{BER}}}^1 \mathcal{B}(n_{\text{bits}}, \text{BER}_{c_d}) dx. \quad (4.21)$$

To minimize both probabilities P_{f_p} and P_{f_n} the value for the threshold ρ_{BER} has to be determined which satisfies the condition

$$P_{f_p} = \int_{x=0}^{\rho_{\text{BER}}} \mathcal{B}(200, 0.5) dx \approx P_{f_n} = \int_{x=\rho_{\text{BER}}}^1 \mathcal{B}(200, 0.1587) dx. \quad (4.22)$$

The condition can only be fulfilled approximately as a result of the discrete distribution of the bit errors. Numerical evaluation yields a threshold value of $\rho_{\text{BER}} = 0.31$ as the solution to the condition in (4.22). It results in $P_{f_p} = 4.0135 \cdot 10^{-8}$ and $P_{f_n} = 2.9509 \cdot 10^{-8}$. Hence, the low values of the probabilities indicate that the measurement results are not likely to be affected by false decisions.

The synchronization performance of the FD and TD concepts is evaluated by the two metrics FLR and FER in the following. The FLR provides a metric for the performance of the frame detection, whereas the FER is related to the accuracy of the offset estimations. The direct calculation of the RMSE is not feasible due to the lack of the knowledge about the exact values of the STO and CFO. However, the FER is linked to the RMSE due to the fact that residual estimation errors, which are summarized in the RMSE metric, affect the demodulated payload symbols and, hence, the resulting FER.

4.4.3 Frame loss rate evaluation

The measured FLR is plotted versus SNR in Figure 4.15. For correct interpretation of the FLR it is to note that both concepts achieve in all considered

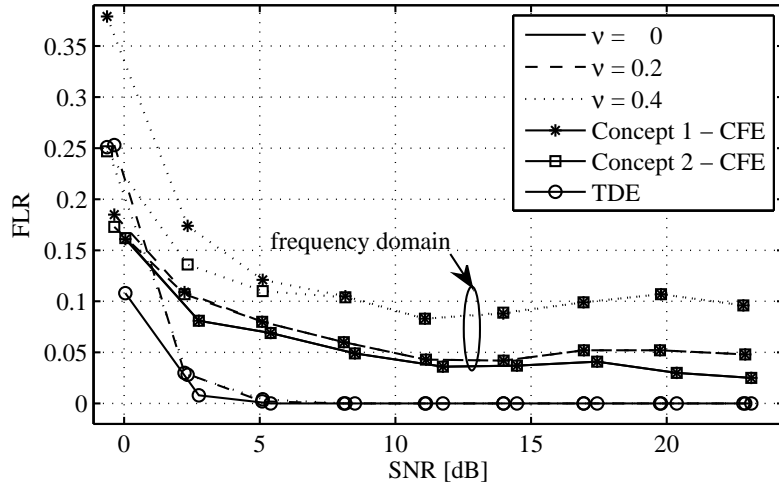


Figure 4.15: Measured FLR versus SNR for different values of the CFO.

scenarios a frame detection rate of 1 for SNR values above 2 dB. The TD synchronization approaches the FLR of 0 for an SNR above 5 dB. Furthermore, the independence of the TD approach from the CFO, as described in the previous section, can be verified from the results. In contrast to the TD solution, the FD approach suffers from a frequency offset, and the FLR floor increases for increasing values of the CFO in the measurement results.

The wiggling of the results around the FLR floor even for high SNR values results from the different starting positions of the bursts for each measurement trial. Even though the timing distance between frames is discrete uniformly distributed with the sample duration T_s in the digital domain, the delay between transmitter and receiver is continuous. The continuous distribution leads to differences of the STO values between trials in the range of fractions of the sample duration T_s . Hence, the range of the STO, that has to be estimated, is individually shifted by fractions of T_s for each trial and influences the STO estimation, which leads to the wiggling of the FLR.

The FLR floor results from the block-wise processing of the FD frame detection and the following STO estimation. Hence, it results in the same floor for Concept 1 and Concept 2 as discussed more in detail in the following. For Concept 1 the histograms of the false STO estimations are plotted in Figure 4.16 for the cases that $\nu = 0$ and $\nu = 0.4$. A false STO estimation is defined as the STO value that is estimated when the BER of a detected frame is greater than the BER threshold $\rho_{BER} = 0.31$. The concentration of the false STO estimations at negative values of the STO around $-T/4 = -16T_s$ indicates that the frame detection metric in (3.22) does not detect the frame start at the correct block index in case that the SFB and AFB are shifted around half an OQAM symbol spacing, i. e., the received energy of the pilot symbols

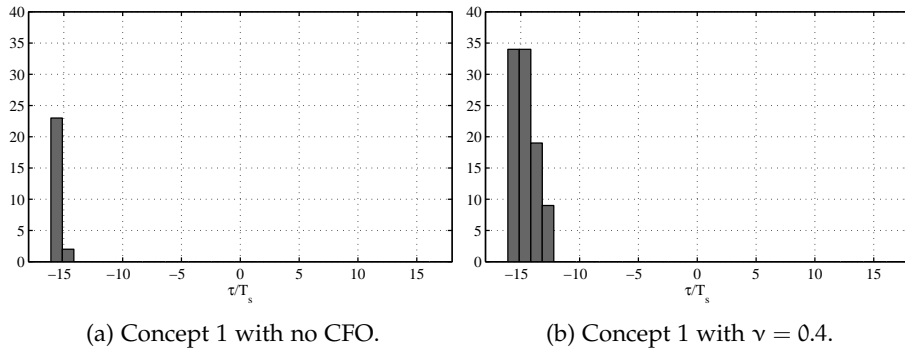


Figure 4.16: Histograms of measured false STO estimations with 10^3 detected frames at an SNR of 24 dB.

of the preamble is equally distributed between two blocks. Furthermore, the STO estimator has only an estimation range that is limited to $|\tau| < T/4$. Hence, it is not able to recover a STO with $|\tau| \geq T/4$ as a result of the wrong decision of the block index of the frame start. The reason for the bias of the block index towards the lower-valued index for these cases is located in the energy metric $Q_b[m]$ in (3.22) and will be explained in the following.

For the explanation it is assumed that the frame starts at block index $m = 0$ and the STO is set to $\tau = T/4 + T_s$. Hence, the correct decision in (3.22) for the block index would be $\hat{m} = 1$, because the delay shifts the modulated and demodulated blocks more than half an OQAM symbol spacing, as illustrated in Figure 4.17 with the frame structure from Figure 3.2. However, the contri-

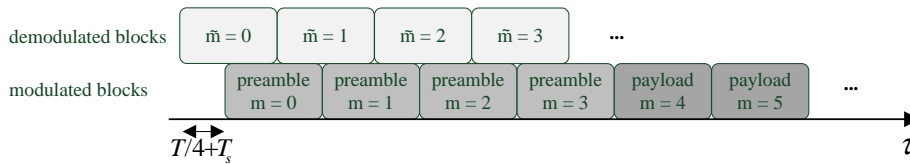


Figure 4.17: Illustration of the delay of $T/4 + T_s$ between modulated and demodulated blocks.

bution from the payload, which starts at the normalized block index $m = 4$, increases the metric $Q_b[1]$ which leads to a decrease of the ratio $\frac{C_b^A[m]}{Q_b[m]}$. Due to the equal distribution of the received pilot symbol energy between block index 0 and 1 the assumption that the correlation output $C_b^A[0]$ is approximately equal to $C_b^A[1]$ holds. It follows that the frame detection metric from (3.22) achieves a maximum at block index $\tilde{m} = 0$. The distorted frame start decision leads to the overall STO of $T/4 + T_s$ that need to be estimated. However,

this value is out of the detection range of the FD synchronization schemes. Hence, the histograms of the falsely synchronized frames show contributions close to $\hat{\tau} = -T/4$, which corresponds to $\tau \geq T/4$ due to the false frame start detection and the phase ambiguity of the STO estimation in (3.56). The frame detection error finally leads to a FLR floor in the measurement results that is independent of the SNR, as presented in Figure 4.15. The frame detection metric degrades further with increasing values of the CFO due to the increasing mismatch between SFB and AFB, as a comparison of Figure 4.16a and Figure 4.16b reveals.

The influence of the STO on the FLR is independent of the concept that is chosen as it influences the FLR at the frame detection stage, which is the same for both concepts. However, the effect of block-wise processing and the resulting FLR floor can be canceled and a FLR which is comparable to the TD solution can be achieved by minor modifications of the FD approach, as will be discussed in the next section.

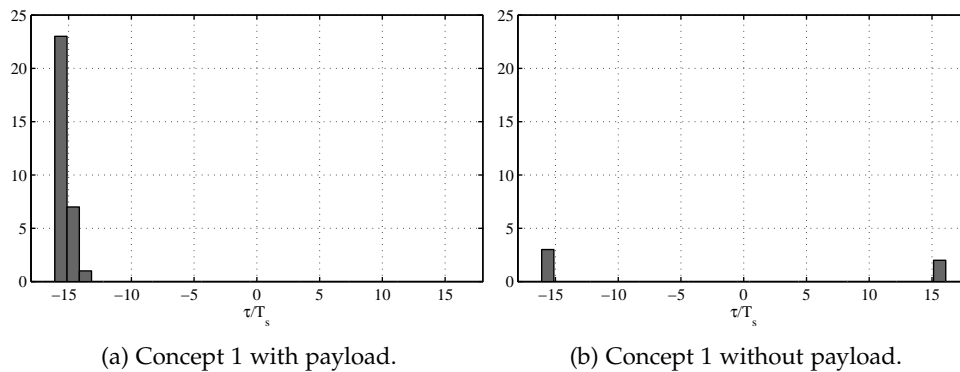


Figure 4.18: Histograms of simulated false STO estimations based on a frame structure with and without payload.

The given explanation is verified by simulation in scenarios where no CFO is present and the STO is uniformly distributed in steps of $T_s/4$ in the range of $\{-T, T\}$. The results of the simulation with 10^3 frames are given in Figure 4.18 by means of the histograms of the STO estimation for falsely synchronized frames at an SNR of 30 dB. The case of a frame with payload is given in Figure 4.18a and a frame without payload is considered in Figure 4.18b. The histogram in Figure 4.18a reveals a similar distribution of the false STO estimations as the histograms derived from the measurements and presented in Figure 4.16. However, the payload-free frame leads to the expected equally distributed STO of the falsely synchronized frames around $|T/4|$ due to the ambiguity in the phase in (3.56). It results in a significantly lower FLR floor of around $5 \cdot 10^{-3}$, derived from the histogram shown in Figure 4.18b.

After discussion of the influence of the STO estimation on the FLR, the influence of the CFO estimation is evaluated. In contrast to the histograms of the STO, the histograms shown in Figure 4.19 include the estimated CFO values for all detected frames independent of the decision of correct or false detection. The histograms of the CFO estimation show a Gaussian-like distri-

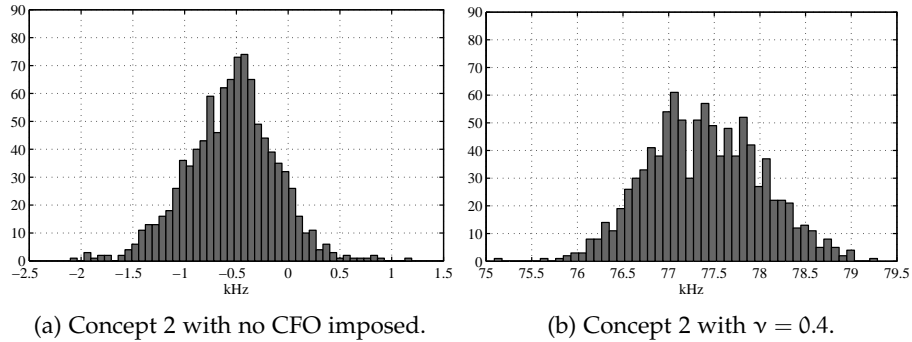


Figure 4.19: Histograms of measured CFO estimations at an SNR of 24 dB.

bution according to the expected distribution of the estimation error. Hence, no indication of a direct influence of the CFO estimation on the FLR is found.

4.4.4 Solutions to the frame loss rate problem

Even though the synchronization performance of the FD synchronization suffers from the block-wise processing, the previous analysis reveals that the FD approach can achieve nearly the same frame detection performance as the TD solution, if the distortion of the frame detection metric is removed. The straightforward approach to minimize the distortion is to add guard blocks between the preamble and payload parts to minimize the contribution from the payload, as suggested from the results of the simulations in Figure 4.18. However, this approach will reduce the resource-efficiency of the preamble design. Nevertheless, to achieve the same frame detection performance for the FD approach as for the TD approach, several modifications can be applied to the FD concepts at receiver side without affecting the frame structure.

The preferred solution is to perform the frame detection based on an AFB with a block shift of only $T/4$ to avoid ambiguity in the decision. This solution leads to a STO that is well within the range of the FD STO estimators but comes at the cost of an increase in complexity of the frame detection stage. The complexity is increased by a factor of two, because twice the amount of blocks need to be demodulated for frame detection. A comparison with the outcome of the complexity analysis, presented in Figure 4.11, reveals that the

complexity of this enhancement is still below the complexity of the time domain solution for multiple users. Hence, the FD approach could achieve the same performance as the TD solution while still being of lower complexity. Apart from the reduction of the size of the block shift, it is possible to extend the Concept 2 to incorporate STO estimation in the first stage. This estimate can be used to correct the block positioning to avoid situations in which the timing offset is close to $T/4$. However, a second block index detection according to (3.22) would then be needed at the second stage. Additionally, it is to note that the effect of the phase ambiguity depends on the number of sub-channels K . Assuming the discrete time model for illustration, where only the STO value of $T/4$ result in an ambiguous estimate of the STO, only one value out of K possible offset values is critical. Hence, with an increasing K , the relation between ambiguous and unambiguous estimates decrease and the FLR floor will be lowered. Depending on the application, the resulting FLR floor can be sufficiently low for high values of K so that no modification will be needed.

4.4.5 Frame error rate evaluation

Following the consideration of the FLR, which indicates how many frames are lost due to missed detection or false synchronization, the quality of the synchronization is given by means of the FER once the lost frames are discarded. The FER is based on the number of bit errors within a frame that are obtained after demodulation and decoding of the bit stream.

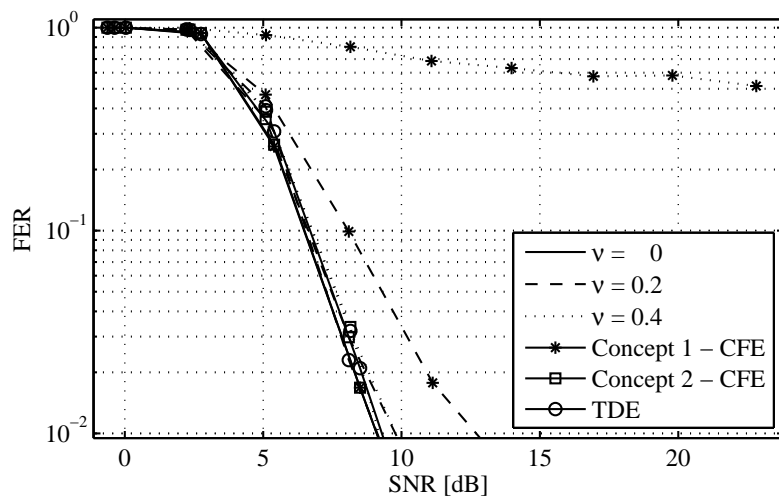


Figure 4.20: Measured FER versus SNR for different values of the CFO.

It follows for the calculation that $\text{FER} = \frac{n_0}{n_{rx}}$, with n_0 equal to the number of decoded frames without a bit error. The plot of the FER in Figure 4.20 reveals that the dominant degradation effect for the FER is the noise in the low SNR region, regardless of the synchronization scheme used. For the reason of readability, the confidence intervals for the results are provided in an additional plot in Appendix E for selected curves. With increasing SNR the CFO leads to a gap between the FER performance of the Concept 1 with FD synchronization and the other schemes. The insufficient estimation performance of the CFO of Concept 1 at high values of the CFO has already been discussed in Figure 4.6. However, for a CFO close to zero, Concept 1 achieves a FER that is the same as for Concept 2 with TD synchronization. The performance of the FD synchronization with Concept 2 reveals no significant deviation from the one of the TD scheme, as expected by the previous results.

4.4.6 Concluding remarks

The outcome of the measurements shows that the FD approach to synchronization achieves nearly the same performance as its TD counterpart with some degradations in its frame detection capabilities for the proposed concepts. However, this drawback can be counteracted by the solutions which we proposed as a consequence of the results from the measurement study.

From this chapter it is concluded that the FD synchronization approach performs equally well as common TD solutions while being of lower complexity for shared spectrum access, where multiple users are accessing the spectrum.

CONCLUSION AND FUTURE WORK

In this thesis we posed the question how frame detection and synchronization in the frequency domain compares to common time domain solutions in the context of fragmented and shared spectrum access. To provide an answer, we proposed and analyzed a resource-efficient and interference-mitigating preamble design for the use in filterbank multicarrier systems. Based on the design we derived a frame detection scheme and obtained the probabilities of missed detection and false alarm to study the effects of frequency domain processing on the frame detection. Furthermore, the Cramér-Rao vector bound of the frequency domain estimation is derived to benchmark the discussed estimation algorithms. We showed that the frequency domain lower bound is a function of the symbol timing and carrier frequency offset, due to the demodulation process involved. However, it is equal to the time domain lower bounds for small offsets.

In addition, we proposed and analyzed optimal as well as practical approaches to symbol timing and carrier frequency offset estimation and evaluated the estimators based on simulations in comparison to the derived lower performance bound. Even though the optimal symbol timing estimator approaches the lower bound, its estimation range is too limited to be practical. However, the practical closed-form estimator is robust to offset-induced interference and nearly achieves the lower bound. In contrast to this, the carrier frequency offset estimation, which is close to the optimum in scenarios with small offsets, strongly depends on the actual carrier frequency offset. For offset values below 10% of the subchannel spacing the estimation is undistorted. However, for larger values a degradation of the estimation can be observed.

Based on the evaluation of the estimation metrics we proposed two frequency domain synchronization concepts. The first one is of low complexity but disregards the influence of large frequency offsets on the estimation performance. Hence, the evaluation showed that an unacceptably high bit error rate floor is present that prevents its usage in a practical system. The second concept removes the influence from frequency offsets on the estimation performance by the introduction of a compensation stage. However, it comes at the cost of a higher complexity. From the comparison of both concepts with an equivalent time domain approach it followed that the second concept achieves a performance that is equal to the time domain solution but has a

lower complexity in shared spectrum transmission because it takes advantage of the inherent separation of users in the frequency domain. Additionally, as an essential part of a practical system, we investigated the possibilities to re-use the preamble for channel estimation and evaluated the influence of residual offsets on its performance.

Following the simulation-based evaluation, we conducted offline measurements to investigate on the practical aspects of the frequency domain solutions. The measured frame error rate verifies that the second frequency domain concept and the time domain approach performs equally well. Even though the block-wise processing leads to a non-zero frame loss rate floor, caused by the ambiguity at the edges of the estimation range, several solutions are discussed to solve the ambiguity problem and to achieve the same performance as equivalent time domain solutions.

In conclusion, the outcome of this thesis shows that the frequency domain approach is advantageous in shared spectrum access compared to common time domain schemes. The frequency domain processing outperforms time domain methods in terms of computational costs in shared spectrum access transmission while the same synchronization performance is maintained. The time domain solution only offers the same performance at lower computational costs in exclusive spectrum access. Furthermore, the frequency domain approach offers a flexibility for resource allocation due to the separate processing of subbands. This flexibility is not reached by time domain solutions, but will be needed in shared spectrum access at base station side to cope with asynchronous transmission of user terminals in the uplink.

In the future the presented concept of practical frequency domain estimation can be combined with advanced receiver designs that perform compensation of the estimated offsets in the frequency domain. Approaches to frequency domain compensation have already been discussed in [22] and [62]. Suitable resource allocation methods and medium access protocols, which make use of the per-user estimation and compensation in the uplink, may lead to a multi-user handling with reduced synchronization requirements. Hence, it lowers or removes signaling overhead in the network, which is especially relevant for short package transmission.

However, more research is needed to develop and analyze a complete system design and verify its advantages over classical time domain approaches for the next generation of cellular networks to enable efficient ubiquitous mobile connectivity for the increasing number of users.

Part II

APPENDIX

\mathbf{R} has only non-zero entries on the first off-diagonals, which are occupied by some value $|\alpha| < 1$. Under the assumption that $p[nT_s]$ is in good approximation a perfect reconstruction pulse shape that overlaps only with the subchannels directly adjacent to itself, $\mathbf{P}\mathbf{P}^H = \mathbf{I} + \mathbf{R}$ holds.

To distinguish between time and frequency domain noise energy σ_n^2 is renamed to σ_ψ^2 for $\mathbf{C}_\psi^{K \times K}$ in (A.4). Considering the structure of the preamble with only every second subchannel occupied, the noise that adds to the received pilot symbols after the analysis filterbank can still be considered white Gaussian noise. Furthermore, it is independent of the offsets that affects the received pilot symbols. This can also be understood intuitively by looking at the transfer function of the prototype filter, which expands only over adjacent subchannels. It follows that the relevant covariance matrix is \mathbf{C}_ψ , as defined in (3.51).

REGULARITY CONDITIONS

In this chapter the regularity conditions [44] of the CRVB for the offset and channel estimations are verified.

Offset estimation

The condition for the offset estimation is defined as

$$\mathbb{E} \left[\frac{\partial \ln(l(\tilde{\mathbf{b}}|\mathbf{v}))}{\partial v_i} \right] = 0 \quad \forall i \in \{1, 2, 3\}. \quad (\text{B.1})$$

Inserting (3.50) in (B.1) leads to

$$\mathbb{E} \left[\frac{\partial \ln(l(\tilde{\mathbf{b}}|\mathbf{v}))}{\partial v_i} \right] = \frac{-T_s}{\sigma_\Psi^2} \mathbb{E} \left[\frac{\partial}{\partial v_i} \left((\tilde{\mathbf{b}} - \gamma e^{j\phi} \mathbf{A} \mathbf{E} \mathbf{H} \mathbf{b})^H \underbrace{(\tilde{\mathbf{b}} - \gamma e^{j\phi} \mathbf{A} \mathbf{E} \mathbf{H} \mathbf{b})}_{=\Psi} \right) \right] \quad (\text{B.2})$$

with $\Psi = [\Psi_1, \Psi_2, \dots, \Psi_W]^T$, as defined in (3.13). It follows that

$$\begin{aligned} \mathbb{E} \left[\frac{\partial \ln(l(\tilde{\mathbf{b}}|\mathbf{v}))}{\partial v_i} \right] &= \frac{-T_s}{\sigma_\Psi^2} \mathbb{E} \left[\frac{\partial}{\partial v_i} \left(\sum_{w=1}^W \Psi_w^* \Psi_w \right) \right] \quad (\text{B.3}) \\ &= \frac{-T_s}{\sigma_\Psi^2} \sum_{w=1}^W \left(\mathbb{E} \left[\frac{\partial \Psi_w^*}{\partial v_i} \Psi_w \right] + \mathbb{E} \left[\Psi_w^* \frac{\partial \Psi_w}{\partial v_i} \right] \right) \\ &= \frac{-T_s}{\sigma_\Psi^2} \sum_{w=1}^W \left(\mathbb{E} \left[\frac{\partial \Psi_w^*}{\partial v_i} \right] \mathbb{E} [\Psi_w] + \mathbb{E} [\Psi_w^*] \mathbb{E} \left[\frac{\partial \Psi_w}{\partial v_i} \right] \right). \end{aligned}$$

In the last calculation step the expectation can be taken for each coefficient of the product $\partial \Psi_w / \partial v_i \Psi_w$ independently. It follows from the statistical independence of $\partial \Psi_w / \partial v_i$ and Ψ_w , as reported in [44]. With $\mathbb{E} [\Psi_w] = \mathbb{E} [\Psi_w^*] = 0$ the regularity condition is fulfilled and the CRVB can be calculated for the given problem.

Channel estimation

Inserting the log-likelihood function from (3.90) in

$$\mathbb{E} \left[\frac{\partial \ln(l(\tilde{\mathbf{b}}|\mathbf{w}))}{\partial w_i} \right] = 0 \quad \forall i \in \{1, 2\} \quad (\text{B.4})$$

yields for the derivation with respect to h_k^R the following expression

$$\begin{aligned} \mathbb{E} \left[\frac{\partial \ln(l(\tilde{\mathbf{b}}|\boldsymbol{w}))}{\partial h_k^R} \right] = & \mathbb{E} \left[\frac{-T_s}{\sigma_\Psi^2} \left(-\tilde{\mathbf{b}}_k^H \boldsymbol{\gamma} \mathbf{A}_k \mathbf{E}_k \mathbf{b}_k \right. \right. \\ & \left. \left. - \mathbf{b}_k^H \mathbf{E}_k^H \mathbf{A}_k^H \boldsymbol{\gamma} \tilde{\mathbf{b}}_k + 4|\mathbf{a}|^2 \gamma^2 h_k^R \right) \right] = 0. \end{aligned} \quad (\text{B.5})$$

When taking the expectation and with $\mathbb{E}[\tilde{\mathbf{b}}_k] = \gamma \mathbb{E}[h_k] \mathbf{A}_k \mathbf{E}_k \mathbf{b}_k$, (B.5) results in

$$\frac{-T_s}{\sigma_\Psi^2} \left(-2\gamma^2 \mathbb{E}[h_k^R] \mathbf{b}_k^H \mathbf{E}_k^H \mathbf{A}_k^H \mathbf{A}_k \mathbf{E}_k \mathbf{b}_k + 4|\mathbf{a}|^2 \gamma^2 \mathbb{E}[h_k^R] \right) = 0. \quad (\text{B.6})$$

Some further calculations lead to

$$4|\mathbf{a}|^2 \mathbb{E}[h_k^R] - 4|\mathbf{a}|^2 \mathbb{E}[h_k^R] = 0. \quad (\text{B.7})$$

Hence, the condition is fulfilled for h_k^R . The same holds for the derivation with respect to h_k^I .

ERROR FLOORS

In this chapter the interference-mitigating feature of the CFE is discussed and the error floors of the CFO and channel estimations are derived.

Interference-mitigating property of the CFE

In contrast to the estimation of ν and its corresponding error floor, which is derived in the next section, the performance limit as a result of the self-interference in case of the CFE cannot be calculated for each subchannel independently due to the relation between subchannels according to (3.56). Nevertheless, it can be shown that the CFE can partially cancel the interference. For the study of this capability the influence from noise, the common phase shift, and the channel coefficients are neglected and the received pilots are derived from (3.10) as

$$\tilde{b}_{k,i} = e^{-j\frac{i2\pi}{T}k\tau}(\mathbf{a}_i(\tau, \nu)\mathbf{b}_{k,i} + \mathbf{u}_{k,i}(\tau, \nu)) \quad (\text{C.1})$$

where $\gamma = 1$ is assumed without loss of generality. Here, the definition of interference, derived from (2.10), is used as

$$\begin{aligned} \mathbf{u}_{k,0}(\tau, \nu) = & \mathbf{b}_{k,2}\mathbf{a}_2(\tau - T, \nu) \\ & + \mathbf{b}_{k-2,0}\mathbf{a}_0(\tau, \nu + 2) + \mathbf{b}_{k-2,2}\mathbf{a}_2(\tau - T, \nu + 2) \\ & + \mathbf{b}_{k+2,0}\mathbf{a}_0(\tau, \nu - 2) + \mathbf{b}_{k+2,0}\mathbf{a}_2(\tau - T, \nu - 2) \end{aligned} \quad (\text{C.2})$$

and

$$\begin{aligned} \mathbf{u}_{k,2}(\tau, \nu) = & \mathbf{b}_{k,0}\mathbf{a}_0(\tau + T, \nu) \\ & + \mathbf{b}_{k-2,0}\mathbf{a}_0(\tau + T, \nu + 2) + \mathbf{b}_{k-2,2}\mathbf{a}_2(\tau, \nu + 2) \\ & + \mathbf{b}_{k+2,0}\mathbf{a}_0(\tau + T, \nu - 2) + \mathbf{b}_{k+2,2}\mathbf{a}_2(\tau, \nu - 2). \end{aligned} \quad (\text{C.3})$$

If appropriate the expressions $\mathbf{a}_i(\tau, \nu)$ and $\mathbf{u}_{k,i}(\tau, \nu)$ are simplified to \mathbf{a}_i and $\mathbf{u}_{k,i}$, respectively, for readability in the following. Defining \mathbb{K}_{np} as the subset of indices $k \in \mathbb{K}_p$, which fulfill the condition that $k, k + \Delta_k$, and $k + 2\Delta_k$ are part of the set \mathbb{K}_p , the CFE from (3.56) results in

$$\hat{\tau}_{\text{CFE}} = \frac{T}{2\pi\Delta_k} \angle \left(\sum_{i \in \{0,2\}} \sum_{k \in \mathbb{K}_{np}} \frac{\tilde{b}_{k,i}\tilde{b}_{k+\Delta_k,i}^*}{\mathbf{b}_{k,i}\mathbf{b}_{k+\Delta_k,i}} + \frac{\tilde{b}_{k+\Delta_k,i}\tilde{b}_{k+2\Delta_k,i}^*}{\mathbf{b}_{k+\Delta_k,i}\mathbf{b}_{k+2\Delta_k,i}} \right). \quad (\text{C.4})$$

Inserting (C.1) into (C.4) and after some calculations it follows that

$$\begin{aligned}
 \hat{\tau}_{\text{CFE}} &= \frac{T}{2\pi\Delta_k} \angle \left(e^{j\frac{2\pi}{T}\Delta_k\tau} \right. & (C.5) \\
 &\quad \times \left(\sum_{i \in \{0,2\}} \sum_{k \in \mathbb{K}_{np}} \frac{(a_i b_{k,i} + \iota_{k,i})(a_i b_{k+\Delta_k,i} + \iota_{k+\Delta_k,i})^*}{b_{k,i} b_{k+\Delta_k,i}} \right. \\
 &\quad \left. \left. + \frac{(a_i b_{k+\Delta_k,i} + \iota_{k+\Delta_k,i})(a_i b_{k+2\Delta_k,i} + \iota_{k+2\Delta_k,i})^*}{b_{k+\Delta_k,i} b_{k+2\Delta_k,i}} \right) \right) \\
 &= \frac{T}{2\pi\Delta_k} \angle \left(e^{j\frac{2\pi}{T}\Delta_k\tau} \left(\sum_{i \in \{0,2\}} \sum_{k \in \mathbb{K}_{np}} 2|a_i|^2 \right. \right. \\
 &\quad \left. \left. + \underbrace{\frac{(a_i^R \iota_{k+\Delta_k,i}^R + a_i^I \iota_{k+\Delta_k,i}^I)}{b_{k+\Delta_k,i}}}_{=\xi_{k+\Delta_k} \in \mathbb{R}} + \underbrace{\frac{a_i \iota_{k+2\Delta_k,i}^*}{b_{k+2\Delta_k,i}} + \frac{a_i^* \iota_{k,i}}{b_{k,i}}}_{=\xi_{k+2\Delta_k}} \right) \right. \\
 &\quad \left. \left. + \underbrace{\sum_{i' \in \{0,2\}} \sum_{k' \in \mathbb{K}_{np}} \frac{\iota_{k',i'} \iota_{k'+\Delta_k,i'}^*}{b_{k',i'} b_{k'+\Delta_k,i'}} + \frac{\iota_{k'+\Delta_k,i'} \iota_{k'+2\Delta_k,i'}^*}{b_{k'+\Delta_k,i'} b_{k'+2\Delta_k,i'}}}_{=\xi_{i'}} \right) \right) \\
 &\approx \frac{T}{2\pi\Delta_k} \angle \left(e^{j\frac{2\pi}{T}\Delta_k\tau} \sum_{i \in \{0,2\}} \sum_{k \in \mathbb{K}_{np}} \left(2|a_i|^2 \right. \right. \\
 &\quad \left. \left. + \frac{(a_i^R \iota_{k+\Delta_k,i}^R + a_i^I \iota_{k+\Delta_k,i}^I)}{b_{k+\Delta_k,i}} + \frac{a_i \iota_{k,i}}{b_{k,i}} + \frac{a_i \iota_{k+2\Delta_k,i}^*}{b_{k+2\Delta_k,i}} \right) \right).
 \end{aligned}$$

From the definition of ι_i in (C.2) and (C.3) it follows that the contribution from $\xi_{i'}$ is small compared to ξ_k and $\xi_{k+2\Delta_k}$. Hence, $\xi_{i'}$ has only a minor impact on the overall performance floor and it is neglected in the approximation. The interference $\xi_{k+\Delta_k}$, which effects the estimation metric for the subchannel index $k + \Delta_k$, is only real-valued and does not influence the estimation of the phase to obtain an estimate of τ . This cancellation feature of the CFE is based on the summation of related estimates. The summation over \mathbb{K}_{np} eventually cancels the interference at all indices in \mathbb{K}_{np} except the first and the last one for the case that a contiguous subchannel allocation is used.

In conclusion, the previous analysis of the CFE shows that it is very robust against self-interference due to the pairwise evaluation of the received pilot symbols. Hence, no impact on the estimation is observable in terms of an error floor in the simulation results.

Error floor of the CFO estimation

Given the preamble structure from (3.5), the minimum achievable estimation error only depends on the pulse shape $p[nT_s]$. Hence, the RMSE_{\min} of the CFO

estimation can be determined by evaluation of the ambiguity functions for a single subchannel averaged over the offset range and possible combinations of the preamble sequence $b_{k,m}$ from (3.5) according to

$$\text{RMSE}_{\min} = \left(\frac{1}{n_c} \sum_{c=1}^{n_c} \int_{\tau=-T/4+T_s}^{T/4-T_s} \int_{\nu=-0.5}^{0.5} \epsilon_{\nu}^2(\tau, \nu, c) d\nu d\tau \right)^{\frac{1}{2}} \quad (\text{C.6})$$

with the CFO estimation error $\epsilon_{\nu}(\tau, \nu, c)$ and the number of possible combinations n_c of the BPSK preamble sequence. For the calculation of the minimum achievable RMSE the influence from four surrounding subchannels are taken into account to capture the interference in case of frequency offsets. The error $\epsilon_{\nu}(\tau, \nu, c)$ depends on the combination index c and the offsets τ and ν and is defined as the difference in phase between the interference-free estimate from $a_2^*(\tau, \nu)a_0(\tau, \nu)$ and the interference-afflicted estimate

$$\epsilon_{\nu}(\tau, \nu, c) = \frac{1}{2\pi} \angle \left(\frac{a_2(\tau, \nu)a_0^*(\tau, \nu)}{(a_2(\tau, \nu) + \iota_2(\tau, \nu, c))(a_0(\tau, \nu) + \iota_0(\tau, \nu, c))^*} \right). \quad (\text{C.7})$$

The interference from the neighboring preamble symbols, summarized in the terms $\iota_i(\tau, \nu, c)$, is calculated as

$$\begin{aligned} \iota_0(\tau, \nu, c) = & a_2(\tau - T, \nu) \\ & + (-1)^c (a_0(\tau, \nu + 2) + a_2(\tau - T, \nu + 2)) \\ & + (-1)^{\lceil c/2 \rceil} (a_0(\tau, \nu - 2) + a_2(\tau - T, \nu - 2)) \end{aligned} \quad (\text{C.8})$$

and

$$\begin{aligned} \iota_2(\tau, \nu, c) = & a_0(\tau + T, \nu) \\ & + (-1)^c (a_0(\tau + T, \nu + 2) + a_2(\tau, \nu + 2)) \\ & + (-1)^{\lceil c/2 \rceil} (a_0(\tau + T, \nu - 2) + a_2(\tau, \nu - 2)). \end{aligned} \quad (\text{C.9})$$

In the considered case of $K = 64$ the evaluation yields a RMSE_{\min} of $2.55 \cdot 10^{-2}$, which is close to the RMSE value of the error floor in Figure 3.10.

Error floor of the channel estimation

The calculation of the minimum achievable RMSE follows the same procedure as described previously for the CFO estimation. Hence, the error floor can be calculated according to

$$\text{RMSE}_{\min} = \left(\frac{1}{n_c} \sum_{c=1}^{n_c} \int_{\tau=-\tau_{\max}}^{\tau_{\max}} \int_{\nu=-\nu_{\max}}^{\nu_{\max}} |\epsilon_h(\tau, \nu, c)|^2 d\nu d\tau \right)^{\frac{1}{2}} \quad (\text{C.10})$$

with the channel estimation error $\epsilon_h(\tau, \nu, c)$. $\epsilon_h(\tau, \nu, c)$ is a function of the offsets τ and ν and the chosen pilot sequence in (3.5) out of the n_c possible combinations and yields

$$\epsilon_h(\tau, \nu, c) = \frac{\alpha_2(\tau, \nu) + \iota_2(\tau, \nu, c) + \alpha_1(\tau, \nu) + \iota_1(\tau, \nu, c)}{2}. \quad (\text{C.11})$$

The interference from the surrounding preamble symbols to the pilot symbol under consideration is summarized in the terms $\iota_i(\tau, \nu, c)$, that are defined in (C.8) and (C.9). For the derivation the channel factor $e^{j2\pi\Phi}$ is set to 1 without loss of generality because of its irrelevance to the absolute value of the error. However, it is considered in the simulations to achieve the i.i.d. property of h_k . Numerical evaluations of the approximations for the interference-limited RMSE are given in Table 3.2.

TD CFO ESTIMATION WITH DIFFERENT PREAMBLES

The effect of the short preamble on the TD CFO estimation can be observed in Figure D.1 for the TD scheme. For the short preamble the condition $s[nT_s] =$

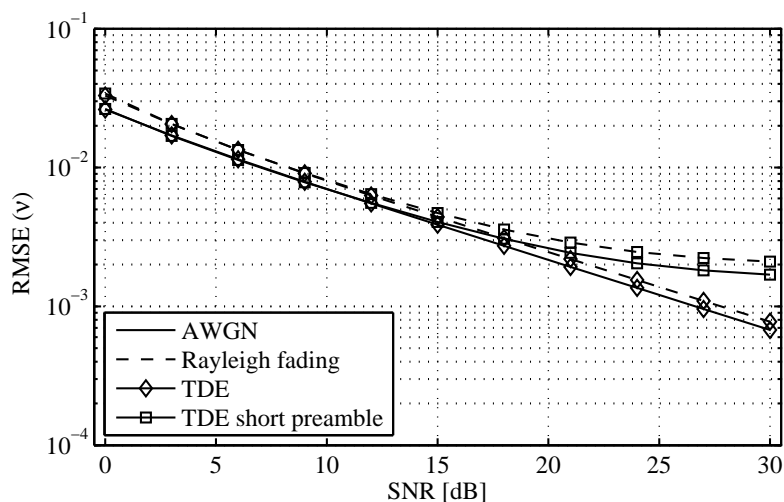


Figure D.1: RMSE of the CFO estimation versus SNR for the normal and short preamble design used by the TD approach.

$s[nT_s + T]$ for $nT_s \in \{(\beta - 1)T, \dots, \beta T - T_s\}$ from (3.8) only holds approximately. This approximation influences the correlation metric in (4.1) and leads to a distortion of the preceding phase estimation in (4.6) to obtain an estimate for the CFO. In Figure D.1 the effect of the distortion results in an error floor of the RMSE of the CFO. The difference between the results for the two preamble types is not significant in the SNR range considered for the measurements in Chapter 4. Hence, the results obtained by simulations can be used in good approximation for the discussion of the measurement results.

MEASURED FER WITH CONFIDENCE INTERVALS

The statistical significance of the FER measurements is not indicated in Figure 4.20 to improve readability. The 95% confidence interval has been added to a selection of the curves from Figure 4.20 in Figure E.1 to show that the number of received frames is sufficient to draw consistent conclusions from the results. The curves are selected from the FD concept 1 because it shows the

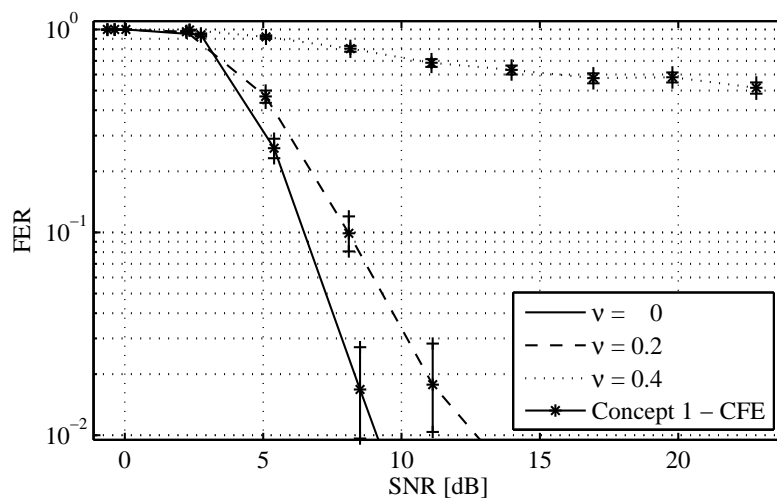


Figure E.1: Measured FER versus SNR including a confidence interval of 0.95.

worst-case scenario with the fewest frames taken into account. The confidence intervals reveal that the number of frames is sufficient to draw the conclusion that the FD concept 2 has the same performance as the TD scheme for the FER range above 10^{-1} , which is used as a performance indication in most practical system.

BIBLIOGRAPHY

- [1] Digital dividend: Insights for spectrum decisions. Technical report, ITU. URL http://www.itu.int/ITU-D/tech/digital_broadcasting/Reports/DigitalDividend.pdf. Online, accessed 22 July 2014.
- [2] Gnuradio project. URL <http://gnuradio.org/redmine/projects/gnuradio/wiki>. Online, accessed 20 June 2014.
- [3] USRP N210 data sheet. URL https://www.ettus.com/content/files/07495_Ettus_N200-210_DS_Flyer_HR_1.pdf. Online, accessed 20 June 2014.
- [4] SBX data sheet. URL http://www.ettus.com/content/files/kb/Selecting_an_RF_Daughterboard.pdf. Online, accessed 20 June 2014.
- [5] IEEE Standard for Information technology - Local and metropolitan area networks - Specific requirements Part 11 : Wireless LAN Medium Access Control (MAC) and Physical Layer (PHY) Specifications. 2012.
- [6] IEEE Standard for Information technology - Local and metropolitan area networks - Specific requirements Part 11: Wireless LAN Medium Access Control (MAC) and Physical Layer (PHY) Specifications Amendment 5: Television White Spaces (TVWS) Operation. 2013.
- [7] A. Akansu and P. Duhamel. Orthogonal transmultiplexers in communication: A review. *IEEE Transactions on Signal Processing*, 46(4), 1998.
- [8] P. Amini and B. Farhang-Boroujeny. Packet format design and decision directed tracking methods for filter bank multicarrier systems. *EURASIP Journal on Advances in Signal Processing*, 2010, 2010.
- [9] P. Bahl, R. Chandra, T. Moscibroda, R. Murty, and M. Welsh. White space networking with Wi-Fi like connectivity. *ACM SIGCOMM Computer Communication Review*, 39, 2009.
- [10] M. Bellanger. FBMC physical layer : a primer. Technical report, 2010. URL http://www.ict-phydyas.org/teamospace/internal-folder/FBMC-Primer_06-2010.pdf. Online, accessed 5 February 2012.
- [11] M. Bellanger and J. Daguët. TDM-FDM transmultiplexer: digital polyphase and FFT. *IEEE Transactions on Communications*, 22(9), 1974.

- [12] J. J. Benedetto, C. Heil, and D. F. Walnut. Differentiation and the Balian-Low theorem. *Journal of Fourier Analysis and Application*, 1(4), 1995.
- [13] J. J. Benedetto, C. Heil, and D. F. Walnut. Gabor systems and the Balian-Low theorem. In H. G. Feichtinger and T. Strohmer, editors, *Gabor analysis and algorithms*. Birkhäuser, 1998.
- [14] H. Bölcskei. Orthogonal frequency division multiplexing based on offset QAM. In H. G. Feichtinger and T. Strohmer, editors, *Advances in Gabor analysis*. Birkhäuser, 2003.
- [15] H. Bölcskei, P. Duhamel, and R. Hleiss. Design of pulse shaping OFDM/OQAM systems for high data-rate transmission over wireless channels. In *Proc. of the IEEE International Conference on Communications (ICC'99)*, Vancouver, Canada, June 1999.
- [16] H. Bölcskei, P. Duhamel, and R. Hleiss. Orthogonalization of OFDM/OQAM pulse shaping filters using the discrete Zak transform. *Signal Processing*, 83(7), 2003.
- [17] S. Caekenberghe, A. Bourdoux, L. der Perre, and J. Louveaux. Preamble-based frequency-domain joint CFO and STO estimation for OQAM-based filter bank multicarrier. *EURASIP Journal on Advances in Signal Processing*, 2014(1), 2014.
- [18] P. Chevillat and G. Ungerboeck. Optimum FIR transmitter and receiver filters for data transmission over band-limited channels. *IEEE Transactions on Communications*, 30(8), 1982.
- [19] T.-D. Chiueh and P.-Y. Tsai. *OFDM baseband receiver design for wireless communications*. John Wiley & Sons, 2008.
- [20] Y. S. Cho, J. Kim, W. Y. Yang, and C. G. Kang. *MIMO-OFDM wireless communications with MATLAB*. John Wiley & Sons, 2010.
- [21] Cisco. Cisco Visual Networking Index: Global Mobile Data Traffic Forecast Update, 2013 - 2018. *White Paper*, 2014. URL http://www.cisco.com/c/en/us/solutions/collateral/service-provider/visual-networking-index-vni/white_paper_c11-520862.pdf. Online, accessed 22 July 2014.
- [22] J.-B. Doré, V. Berg, N. Cassiau, and D. Ktésas. FBMC receiver for multi-user asynchronous transmission on fragmented spectrum. *EURASIP Journal on Advances in Signal Processing*, 2014(1), 2014.

- [23] J. Du and S. Signell. Comparison of CP-OFDM and OFDM/OQAM in doubly dispersive channels. In *Proc. of the Future Generation Communication and Networking (FGCN'07)*, Jeju, Korea, Dec. 2007.
- [24] J. Du and S. Signell. Pulse shape adaptivity in OFDM/OQAM systems. In *Proc. of the 2008 International Conference on Advanced Infocomm Technology (ICAIT'08)*, Shenzhen, China, July 2008.
- [25] B. Farhang-Boroujeny. OFDM versus filter bank multicarrier. *Signal Processing Magazine, IEEE*, 28(3), 2011.
- [26] B. Farhang-Boroujeny and C. H. Yuen. Cosine modulated and offset QAM filter bank multicarrier techniques: a continuous-time prospect. *EURASIP Journal on Advances in Signal Processing*, 2010, 2010.
- [27] M. Fuhrwerk, J. Peissig, and M. Schellmann. Channel adaptive pulse shaping for OQAM-OFDM systems. In *Proc. of the 22nd European Signal Processing Conference (EUSIPCO'14)*, Lisbon, Portugal, Sept. 2014.
- [28] T. Fusco, A. Petrella, and M. Tanda. Data-aided symbol timing estimation for multiple-access OFDM/OQAM systems. In *Proc. of the IEEE International Conference on Communications (ICC'09)*, Dresden, Germany, June 2009.
- [29] T. Fusco, A. Petrella, and M. Tanda. Data-aided symbol timing and CFO synchronization for filter bank multicarrier systems. *IEEE Transactions on Wireless Communications*, 8(5), 2009.
- [30] T. Fusco, A. Petrella, and M. Tanda. Joint symbol timing and CFO estimation in multiuser OFDM/OQAM systems. In *Proceeding of the 10th Workshop on Signal Processing Advances in Wireless Communications (SPAWC'09)*, Perugia, Italy, June 2009.
- [31] T. Fusco, A. Petrella, and M. Tanda. Joint symbol timing and CFO estimation for OFDM/OQAM systems in multipath channels. *EURASIP Journal on Advances in Signal Processing*, 2010:3, 2010.
- [32] L. Häring. *Synchronisation in Mehrnutzer-OFDM-Systemen*. PhD thesis, Universität Duisburg-Essen, 2007.
- [33] F. J. Harris. *Multirate signal processing for communication systems*. Prentice Hall PTR, 2004.
- [34] T. Hidalgo Stitz, T. Ihalainen, and M. Renfors. Practical issues in frequency domain synchronization for filter bank based multicarrier transmission. In *Proc. of the 3rd International Symposium on Communications*,

- Control and Signal Processing (ISCCSP'08)*, St. Julians, Malta, Mar. 2008. IEEE.
- [35] B. Hirosaki. An orthogonally multiplexed QAM system using the discrete Fourier transform. *IEEE Transactions on Communications*, 29(7), 1981.
- [36] T. Ihalainen, A. Viholainen, T. Stitz, and M. Renfors. Filter bank based multi-mode multiple access scheme for wireless uplink. In *Proc. of the 17th European Signal Processing Conference (EUSIPCO'09)*, Glasgow, UK, Aug. 2009.
- [37] L. Izzo, D. Mattera, and M. Tanda. Multipath-aware joint symbol timing and CFO estimation in multiuser OFDM/OQAM systems. In *Proc. of the 18th European Signal Processing Conference (EUSIPCO'10)*, Aalborg, Denmark, Aug. 2010.
- [38] J.-P. Javaudin, D. Lacroix, and A. Rouxel. Pilot-aided channel estimation for OFDM/OQAM. In *Proc. of the 57th IEEE Semiannual Vehicular Technology Conference (VTC'03-Spring)*, Jeju, Korea, Apr. 2003.
- [39] W. Jiang and M. Schellmann. Suppressing the out-of-band power radiation in multi-carrier systems: A comparative study. In *Proc. of the IEEE Global Communications Conference (GLOBECOM'12)*, Anaheim, California, USA, Dec. 2012.
- [40] P. Jung. *Weyl-Heisenberg Representations in Communication Theory*. PhD thesis, Technische Universität Berlin, 2007.
- [41] P. Jung and G. Wunder. The WSSUS pulse design problem in multicarrier transmission. *IEEE Transactions on Communications*, 55(10), 2007.
- [42] K. D. Kammeyer. *Nachrichtenübertragung*. Vieweg+Teubner, 4th edition, 2008.
- [43] D. Katselis, E. Kofidis, A. Rontogiannis, and S. Theodoridis. Preamble-based channel estimation for CP-OFDM and OFDM/OQAM systems: a comparative study. *IEEE Transactions on Signal Processing*, 58(5), 2010.
- [44] S. M. Kay. *Fundamentals of Statistical Signal Processing: Estimation Theory*. Prentice-Hall, 1993.
- [45] S. M. Kay. *Fundamentals of Statistical Signal Processing: Detection Theory*. Prentice-Hall, 1998.

- [46] E. Kofidis, D. Katselis, A. Rontogiannis, and S. Theodoridis. Preamble-based channel estimation in OFDM/OQAM systems: a review. *Signal Processing*, 93(7), 2013.
- [47] M. Marey and H. Steendam. Analysis of the narrowband interference effect on OFDM timing synchronization. *IEEE Transactions on Signal Processing*, 55(9), 2007.
- [48] D. Mattera and M. Tanda. Preamble-based synchronization for OFDM/OQAM systems. In *Proc. of the 19th European Signal Processing Conference (EUSIPCO'11)*, Barcelona, Spain, Aug. 2011.
- [49] D. Mattera and M. Tanda. Data-aided synchronization for OFDM/OQAM systems. *Signal Processing*, 92(9), 2012.
- [50] Y. Medjahdi, M. Terre, D. Le Ruyet, D. Roviras, and A. Dziri. Performance analysis in the downlink of asynchronous OFDM/FBMC based multi-cellular networks. *IEEE Transactions on Wireless Communications*, 10(8), 2011.
- [51] Y. Medjahdi, D. Le Ruyet, D. Roviras, H. Shaiek, and R. Zakaria. On the impact of the prototype filter on FBMC sensitivity to time asynchronism. In *Proc. of the 9th International Symposium on Wireless Communication Systems (ISWCS'12)*, Paris, France, Aug 2012.
- [52] A. F. Molisch. *Wireless Communications*. John Wiley & Sons, 2011.
- [53] P. H. Moose. A technique for orthogonal frequency division multiplexing frequency offset correction. *IEEE Transactions on Communications*, 42(10), 1994.
- [54] M. Morelli, C.-C. Kuo, and M.-O. Pun. Synchronization techniques for orthogonal frequency division multiple access (OFDMA): a tutorial review. *Proc. of the IEEE*, 95(7), 2007.
- [55] N. Moret and A. M. Tonello. Design of orthogonal filtered multi-tone modulation systems and comparison among efficient realizations. *EURASIP Journal on Advances in Signal Processing*, 2010, 2010.
- [56] M. Moretti and I. Cosovic. OFDM synchronization in an uncoordinated spectrum sharing scenario. In *Proc. of the IEEE Global Telecommunications Conference (GLOBECOM'07)*, Washington, DC, USA, Nov. 2007.
- [57] M. Nekovee. Cognitive radio access to TV white spaces: spectrum opportunities, commercial applications and remaining technology challenges.

In *Proc. of the IEEE Symposium on New Frontiers in Dynamic Spectrum (DySPAN'10)*, Singapore, Apr. 2010.

- [58] A. Osseiran, F. Boccardi, V. Braun, K. Kusume, P. Marsch, M. Maternia, O. Queseth, M. Schellmann, H. Schotten, H. Taoka, H. Tullberg, M. Uusitalo, B. Timus, and M. Fallgren. Scenarios for 5G mobile and wireless communications: the vision of the METIS project. *IEEE Communications Magazine*, 52(5), May 2014.
- [59] J. G. Proakis and D. G. Manolakis. *Digital signal processing*. Pearson, 4th edition, 2007.
- [60] J. G. Proakis and M. Salehi. *Digital communications*. McGraw-Hill, 5th edition, 2007.
- [61] R. W. Chang. High-speed multichannel data transmission with bandlimited orthogonal signals. *Bell System Technology Journal*, 45(6), 1966.
- [62] M. Renfors and J. Yli-Kaakinen. Timing offset compensation in fast-convolution filter bank based waveform processing. In *Proc. of the 10th International Symposium on Wireless Communication Systems (ISWCS'13)*, Ilmenau, Germany, Aug. 2013.
- [63] M. Renfors, F. Bader, L. Baltar, D. Le Ruyet, D. Roviras, P. Mege, M. Haardt, and T. Hidalgo Stitz. On the use of filter bank based multicarrier modulation for professional mobile radio. In *Proc. of the 77th IEEE Vehicular Technology Conference (VTC'13-Spring)*, Dresden, Germany, June 2013.
- [64] B. Sadler and R. Kozick. A survey of time delay estimation performance bounds. In *Proc. of the 4th IEEE Workshop on Sensor Array and Multichannel Processing (SAM'06)*, Waltham, MA, USA, July 2006.
- [65] H. Saeedi-Sourck and S. Sadri. Frequency-domain carrier frequency and symbol timing offsets estimation for Offset QAM filter bank multicarrier systems in uplink of multiple access networks. *Wireless personal communications*, 70(2), 2013.
- [66] H. Saeedi-Sourck, Y. Wu, J. W. Bergmans, S. Sadri, and B. Farhang-Boroujeny. Low-complexity carrier frequency offset estimation for multiuser offset QAM filter bank multicarrier systems uplink. In *Proc. of the 75th IEEE Vehicular Technology Conference (VTC'12-Spring)*, Yokohama, Japan, May 2012.

- [67] H. Saeedi-Sourck, S. Sadri, Y. Wu, and B. Farhang-Boroujeny. Near maximum likelihood synchronization for filter bank multicarrier systems. *IEEE Wireless Communications Letters*, 2(2), Apr. 2013.
- [68] B. Saltzberg. Performance of an efficient parallel data transmission system. *IEEE Transactions on Communication Technology*, 15(6), 1967.
- [69] D. Schafhuber, G. Matz, and F. Hlawatsch. Pulse-shaping OFDM/BFDM systems for time-varying channels: ISI/ICI analysis, optimal pulse design, and efficient implementation. In *Proc. of the 13th IEEE International Symposium on Personal, Indoor and Mobile Radio Communications (PIMRC'02)*, Lisbon, Portugal, Sept. 2002.
- [70] J. M. Schellmann. *Multi-user MIMO-OFDM in practice : enabling spectrally efficient transmission over time-varying channels*. PhD thesis, Technische Universität Berlin, 2009.
- [71] T. Schmidl and D. Cox. Robust frequency and timing synchronization for OFDM. *IEEE Transactions on Communications*, 45(12), 1997.
- [72] C. Siclet, P. Siohan, and D. Pinchon. Perfect reconstruction conditions and design of oversampled DFT-modulated transmultiplexers. *EURASIP Journal on Applied Signal Processing*, 2006.
- [73] C. Siclet, P. Siohan, and D. Pinchon. Oversampled orthogonal and biorthogonal multicarrier modulations with perfect reconstruction. In *Proc. of the 14th International Conference on Digital Signal Processing (DSP'02)*, volume 2, Santorini, Greece, July 2002.
- [74] P. Siohan, C. Siclet, and N. Lacaille. Analysis and design of OFDM/O-QAM systems based on filterbank theory. *IEEE Transactions on Signal Processing*, 50(5), 2002.
- [75] A. Skrzypczak, P. Siohan, N. Chotkan, and M. Djoko-Kouam. OFDM/O-QAM: An appropriate modulation scheme for an optimal use of the spectrum. In *Proc. of the 3rd International Symposium on Communications, Control and Signal Processing (ISCCSP'08)*, St. Julians, Malta, Mar. 2008.
- [76] T. H. Stitz, A. Viholainen, T. Ihalainen, and M. Renfors. CFO estimation and correction in a WiMAX-like FBMC system. In *Proc. of the 10th IEEE Workshop on Signal Processing Advances in Wireless Communications (SPAWC'09)*, Perugia, Italy, June 2009.

- [77] T. H. Stitz, T. Ihalainen, A. Viholainen, and M. Renfors. Pilot-Based Synchronization and Equalization in Filter Bank Multicarrier Communications. *EURASIP Journal on Advances in Signal Processing*, 2010, 2010.
- [78] K. W. Sung, L. Shi, and J. Zander. Coexistence of LTE femtocells with GSM cellular network. In *Proc. of the 21st IEEE International Symposium on Personal Indoor and Mobile Radio Communications (PIMRC'10)*, Istanbul, Turkey, Sept. 2010.
- [79] C. Thein, M. Fuhrwerk, and J. Peissig. CFO Estimation Algorithm for OQAM-OFDM Systems Based on the Conjugate Symmetry Property. In *Proc. of the 20th European Signal Processing Conference (EUSIPCO'12)*, Bukarest, Romania, Sept. 2012.
- [80] C. Thein, M. Fuhrwerk, J. Peissig, and M. Schellmann. Opportunistic spectrum access in TVWS: a comparative coexistence study for LTE. In *Proc. of the IEEE International Symposium on Dynamic Spectrum Access Networks (DySPAN'12)*, Bellevue, USA, Oct. 2012.
- [81] C. Thein, M. Fuhrwerk, and J. Peissig. Frequency-domain processing for synchronization and channel estimation in OQAM-OFDM systems. In *Proc. of the 14th IEEE Workshop on Signal Processing Advances in Wireless Communications (SPAWC'13)*, Darmstadt, Germany, June 2013.
- [82] C. Thein, M. Fuhrwerk, and J. Peissig. Practical evaluation of NC-OFDM system designs in dynamic spectrum access with narrow-band interference. In *Proc. of the 10th International Symposium on Wireless Communication Systems (ISWCS'13)*, Ilmenau, Germany, Aug. 2013.
- [83] C. Thein, M. Schellmann, and J. Peissig. Analysis of frequency domain frame detection and synchronization in OQAM-OFDM systems. *EURASIP Journal on Advances in Signal Processing*, 2014(1), 2014.
- [84] A. M. Tonello. Performance limits for filtered multitone modulation in fading channels. *IEEE Transactions on Wireless Communications*, 4(5), Sept. 2005.
- [85] A. M. Tonello and F. Pecile. Efficient architectures for multiuser FMT systems and application to power line communications. *IEEE Transactions on Communications*, 57(5), 2009.
- [86] P. P. Vaidyanathan. Multirate digital filters, filter banks, polyphase networks, and applications: a tutorial. *Proc. of the IEEE*, 78(1), 1990.
- [87] P. P. Vaidyanathan. *Multirate systems and filter banks*. Prentice Hall, 1993.

- [88] M. Vetterli and D. Le Gall. Perfect reconstruction FIR filter banks: some properties and factorizations. *IEEE Transactions on Acoustics, Speech and Signal Processing*, 37(7), 1989.
- [89] A. Viholainen, T. Ihalainen, T. H. Stitz, M. Renfors, and M. Bellanger. Prototype filter design for filter bank based multicarrier transmission. In *Proc. of the 17th European Signal Processing Conference (Eusipco'09)*, Glasgow Scotland, Aug. 2009.
- [90] T. Weiss and F. K. Jondral. Spectrum pooling: an innovative strategy for the enhancement of spectrum efficiency. *IEEE Communications Magazine*, 42(3), 2004.
- [91] T. Weiss, J. Hillenbrand, A. Krohn, and F. K. Jondral. Mutual interference in OFDM-based spectrum pooling systems. In *Proc. of the 59th IEEE Vehicular Technology Conference (VTC'04-Spring)*, Seoul, Korea, May 2004.
- [92] G. Wunder, P. Jung, M. Kasparick, T. Wild, F. Schaich, Y. Chen, S. Brink, I. Gaspar, N. Michailow, A. Festag, L. Mendes, N. Cassiau, D. Ktenas, M. Dryjanski, S. Pietrzyk, B. Eged, P. Vago, and F. Wiedmann. 5GNOW: non-orthogonal, asynchronous waveforms for future mobile applications. *IEEE Communications Magazine*, 52(2), Feb. 2014.
- [93] H. Zhang, D. Le Ruyet, and M. Terre. Spectral efficiency analysis in OFDM and OFDM/OQAM based cognitive radio networks. In *Proceeding of the 69th IEEE Vehicular Technology Conference (VTC'09-Spring)*, Barcelona, Spain, Apr. 2009.

GLOSSARY OF SYMBOLS

β	Overlapping factor.
δ	Kronecker delta.
ϵ	Estimation error.
$\eta[nT_s]$	Circular symmetric Gaussian distributed noise.
γ	Scaling factor of the transmitted signal.
ι	Intersystem interference.
λ	BPSK sequence.
μ	Mean value.
ν	Normalized carrier frequency offset.
Ω	Computational complexity.
φ	Bandwidth efficiency.
$\Psi_{k,m}$	Frequency domain noise.
ϕ	Common phase of the received signal.
Π	Rectangular window.
Φ	Uniformly distributed phase.
ρ	Threshold value.
σ^2	Variance.
$\bar{\tau}_h$	Mean delay of the channel.
τ	Symbol timing offset.
$\theta_{k,m}$	Switch between 1 and j depending on k and m .
Θ	Power per sample or bin.
$\alpha(\tau, \nu)$	Auto ambiguity function.
$\mathbf{A}, \mathbf{E}, \mathbf{H}, \mathbf{b}, \Psi$	Matrix representation of signals and influence of the channel in frequency domain.
B_c	Coherence bandwidth.
$b_{k,m}$	Real-valued pilot symbol within the preamble.
$\mathcal{C}(x)$	Cardinality of x .
$C[m]$	Outcome of correlation.

$C_{\{\Psi\}}, C_{\{\eta\}}$	Covariance matrix of the frequency domain Ψ and time domain η noise.
$c(\tau, \nu)$	Cross ambiguity function.
$d_{k,m}$	Real-valued data symbol within the frame.
e	Euler's constant.
F	Fisher information matrix.
f_{Δ}	Subchannel spacing.
h_k	Channel coefficient of the subchannel k .
$h[nT_s]$	Channel impulse response at time instance nT_s .
$h_c[nT_s]$	Filter impulse response of the prefiltering stage.
I	Identity matrix.
j	Imaginary unit.
k	Subchannel index.
\mathbb{K}	Set of all subchannel indices.
K	Cardinality of \mathbb{K} .
l	Likelihood function.
m	Block index of $T/2$ spaced blocks.
\mathbb{M}, \mathbb{U}	Set of utilized block indices.
n_c	Number of possible combinations.
n_u	Number of users or subbands.
n	Sample index.
P_{fa}	Probability of false alarm.
P_{fn}	Probability of false negative.
P_{fp}	Probability of false positive.
P_{md}	Probability of missed detection.
$P(x)$	Probability of x .
$p[nT_s]$	Prototype filter function.
p^f	Frequency domain prototype filter coefficient.
p	Vector containing prototype filter coefficients.
P	Matrix containing prototype filter coefficients.
$q_{k,u}$	Complex-valued symbol within the frame.
$Q[m]$	Energy normalization factor.
$r[nT_s]$	Received signal.
R	Off-diagonal matrix.

$s[nT_s]$	Transmitted signal.
T_s	Sample duration.
T	Time between two successive symbols $q_{k,u}$ excluding a possible cyclic prefix.
T_{CP}	Duration of the cyclic prefix.
T_{Δ}	Time between two successive symbols $q_{k,u}$ including a possible cyclic prefix.
u	Block index of T spaced blocks.
\mathbf{v}	Vector of the parameters τ, ν and ϕ .
$w[nT_s]$	Interfering signal.
\mathbf{w}	Vector of the parameters h_k^R and h_k^I .
\mathbf{W}	DFT matrix.
$*$	Convolution operator.
\propto	Indicator for proportionality.
$\hat{\cdot}$	Superscription referring to the estimated value.
$\tilde{\cdot}$	Superscription referring to the received value.
\cdot^A	Reference to absolute value.
\cdot^I	Reference to real value.
\cdot^R	Reference to imaginary value.
$E[x]$	Expected value of x .
$\mathcal{F}\{x\}$	Fourier transform of x .
$\lceil x \rceil$	Mapping of x to the smallest following integer.
$\Im\{x\}$	Imaginary part of x .
$\Re\{x\}$	Real part of x .
$\ln(x), \log_2(x)$	Logarithm of x with base e and 2 .
$\text{mod}(a, b)$	Modulo operation on a based on b .
\sim	Distributed according to following distribution.
$\mathcal{B}(n, p)$	Binomial distribution with n number of trials and p equal to the success probability per trial.
χ_n^2	Chi-square distribution with n degree of freedoms.
$\Gamma(a, b)$	Gamma distribution with shape a and scale b .

$\mathcal{N}(\mu, \sigma^2)$	Normal distribution with mean μ and variance σ^2 .
$\mathcal{U}([a, b])$	Uniform distribution in the range of $[a, b]$.

GLOSSARY OF ACRONYMS

AWGN	Additive white Gaussian noise.
BER	Bit error rate.
BPSK	Binary phase shift keying.
CCE	Cross correlation estimator (STO).
CFE	Closed-form estimator (STO).
CFO	Carrier frequency offset.
CMT	Cosine-modulated multitone.
CP	Cyclic prefix.
CRVB	Cramér-Rao vector bound.
DFT (IDFT)	(Inverse) Discrete Fourier transform.
FBMC	Filterbank multicarrier.
FD	Frequency domain.
FER	Frame error rate.
FFT	Fast Fourier transform.
FLR	Frame loss rate.
FMT	Filtered multitone.
FST	Frequency sampling technique.
ICI	Intercarrier interference.
IOTA	Isotropic orthogonal transformation algorithm.
ISI	Intersymbol interference.
LTE	Long-term evolution.
ML	Maximum-likelihood.

MLE	Maximum-likelihood estimator.
MSE	Mean square error.
NC	Non-contiguous.
NMSE	Normalized mean square error.
OFDM	Orthogonal frequency division multiplexing.
OQAM	Offset quadrature amplitude modulation.
PAM	Pulse amplitude modulation.
PAPR	Peak to average power ratio.
PDF	Probability density function.
PDP	Power delay profile.
PPN	Polyphase network.
PSD	Power spectral density.
QAM	Quadrature amplitude modulation.
QPSK	Quadrature phase shift keying.
RF	Radio frequency.
RMSE	Root mean square error.
SIR	Signal power to interference power ratio.
SNR	Signal power to noise power ratio.
STO	Symbol timing offset.
TD	Time domain.
TDE	Time domain estimator.
UHF	Ultra high frequency.
UMTS	Universal mobile telecommunications system.
USRP	Universal software radio platform.
WiFi	Wireless local area network.

INDEX

- A**
Ambiguity function.....7
Auxiliary pilot symbols.....29
- B**
Balian-Low theorem 10
Bit error rate.....18
- C**
Carrier frequency offset.....6
Cramér-Rao vector bound
 channel estimation 58
 offset estimation
 frequency domain.....45
 time domain 49
- E**
Estimator
 CFO.....41
 CFO time domain 65
 channel coefficients.....57
 STO closed-form 43
 STO cross correlation.....44
 STO ML.....42
 STO time domain 65
- F**
FBMC
 PAM 8
 QAM.....8
- Fisher information matrix
 channel estimation 59
 offset estimation.....45
- Frame detection
 frequency domain34
 time domain 64
Frame error rate18
Frame loss rate 18
- I**
Intercarrier interference.....26
Intersymbol interference.....26
Intersystem interference 11
- O**
OFDM.....3
 cyclic prefix 8
 non-contiguous.....15
 OQAM.....10
- P**
Preamble design
 frequency domain30
 time domain.....31
- R**
Root mean square error.....48
- S**
Symbol timing offset.....6

SCIENTIFIC CAREER

Name	Christoph Oliver Thein
Date of birth	04.05.1984
Working Experience	
since 07/2009	Research assistant and PhD student: Institute of Communications Technology at Leibniz Universität Hannover. Research in the field of synchronization algorithms and coexistence for filterbank multicarrier systems.
Teaching Experience	
since 10/2011	Exercises on "Signal and systems"
since 10/2009	Lab exercises on "Physical layer transmission techniques"
Education	
10/2008 – 04/2009	Studies: Electrical engineering at Universität Paderborn. Diploma thesis at the Institute of Optical Communications at Universität Paderborn

02/2008 – 07/2008	Studies: Electrical engineering at Queensland University of Technology, Brisbane, Australia.
10/2006 – 02/2008	Studies: Electrical engineering at Universität Paderborn.
04/2005 – 09/2006	Studies: Electrical engineering at Leibniz Universität Hannover.
10/2004 – 03/2005	Studies: Mechatronics at Leibniz Universität Hannover.

**Publications
& Patents**

1 journal and 10 conference publications.

1 patent granted and 4 further patent applications pending.

LIST OF PUBLICATIONS

- M. Fuhrwerk, C. Thein, and L. Häring. Performance Comparison of CP-OFDM and OQAM-OFDM Based WiFi Systems. In *Proc. of the 16th International OFDM-Workshop (InOWo'11)*, pages 11–15, Hamburg, Germany, August 2011.
- M. Fuhrwerk, C. Thein, and J. Peissig. Audio Quality Measurements for Wireless Microphones in Spectrum Pooling Scenarios. In *Proc. of the IEEE International Conference on Communications - Cognitive Radio and Networks Symposium (ICC'13 CRN)*, pages 1416–1421, Budapest, Hungary, June 2013.
- C. Thein, A. Anggraini, T. Kaiser, and K. L. Chee. Throughput Coverage Simulations Based on Signal Level Measurements at 825 MHz and 3535 MHz. In *Proc. of the 4th International Conference on Signal Processing and Communication Systems (ICSPCS'10)*, Gold Coast, Australia, December 2010a.
- C. Thein, H. Cao, and A. Wilzeck. Setup and Characterization of a Flexible Low-Cost 2×2 MIMO Testbed Based on USRP2. In *Proc. of the 6th Karlsruhe Workshop on Software Radios (WSR'10)*, pages 77–82, Karlsruhe, Germany, March 2010b.
- C. Thein, M. Fuhrwerk, and J. Peissig. CFO Estimation Algorithm for OQAM-OFDM Systems Based on the Conjugate Symmetry Property. In *Proc. of the 20th European Signal Processing Conference (EUSIPCO'12)*, pages 470–473, Bukarest, Romania, August 2012a.
- C. Thein, M. Fuhrwerk, J. Peissig, and M. Schellmann. Opportunistic spectrum access in TVWS: A comparative coexistence study for LTE. In *Proc. of the IEEE International Symposium on Dynamic Spectrum Access Networks (DySPAN'12)*, pages 289–298, Bellevue, USA, October 2012b.
- C. Thein, M. Fuhrwerk, and J. Peissig. Frequency-Domain Processing for Synchronization and Channel Estimation in OQAM-OFDM Systems. In *Proc. of the IEEE 14th Workshop on Signal Processing Advances in Wireless Communications (SPAWC'13)*, pages 634 – 638, Darmstadt, Germany, June 2013a.
- C. Thein, M. Fuhrwerk, and J. Peissig. Practical Evaluation of NC-OFDM System Designs in Dynamic Spectrum Access with Narrow-Band Interference. In *Proc. of the 10th International Symposium on Wireless Communication Systems (ISWCS'13)*, Ilmenau, Germany, August 2013b.

- C. Thein, M. Fuhrwerk, and J. Peissig. About the Use of Different Processing Domains for Synchronization in Non-Contiguous FBMC Systems. In *Proc. of the IEEE 24th International Symposium on Personal Indoor and Mobile Radio Communications (PIMRC'13)*, London, UK, September 2013c.
- C. Thein, M. Schellmann, and J. Peissig. Analysis of frequency domain frame detection and synchronization in OQAM-OFDM systems. *EURASIP Journal on Advances in Signal Processing*, 2014:83, 2014.
- Z. Zhao, C. Thein, F. Zheng, and T. Kaiser. Analysis of the Influence of OFDM Sidelobe Interference on Femto Rich Systems. In *Proc. of the IEEE 9th International Symposium on Modeling and Optimization in Mobile, Ad Hoc, and Wireless Networks (WiOpt'11)*, Princeton, USA, May 2011.